

**DEVELOPMENT OF NOVEL COMPUTATIONAL
METHODS FOR OPTIMAL DESIGN OF ELECTRICALLY SMALL
ELECTROMAGNETIC SCATTERING PARTICLES**

by

Sarah Jensen

A dissertation submitted to the Faculty of the University of Delaware in partial fulfillment of the requirements for the degree of Doctor of Philosophy in Electrical and Computer Engineering

Fall 2022

© 2022 Sarah Jensen
All Rights Reserved

**DEVELOPMENT OF NOVEL COMPUTATIONAL
METHODS FOR OPTIMAL DESIGN OF ELECTRICALLY SMALL
ELECTROMAGNETIC SCATTERING PARTICLES**

by

Sarah Jensen

Approved: _____

Jamie Phillips, Ph.D.
Chair of the Department of Electrical and Computer Engineering

Approved: _____

Levi T. Thompson, Ph.D.
Dean of the College of Engineering

Approved: _____

Louis F. Rossi, Ph.D.
Vice Provost for Graduate and Professional Education and
Dean of the Graduate College

I certify that I have read this dissertation and that in my opinion it meets the academic and professional standard required by the University as a dissertation for the degree of Doctor of Philosophy.

Signed:

Mark Mirotznik, Ph.D.
Professor in charge of dissertation

I certify that I have read this dissertation and that in my opinion it meets the academic and professional standard required by the University as a dissertation for the degree of Doctor of Philosophy.

Signed:

Keith Goosen, Ph.D.
Member of dissertation committee

I certify that I have read this dissertation and that in my opinion it meets the academic and professional standard required by the University as a dissertation for the degree of Doctor of Philosophy.

Signed:

Shridhar Yarlagadda, Ph.D.
Member of dissertation committee

I certify that I have read this dissertation and that in my opinion it meets the academic and professional standard required by the University as a dissertation for the degree of Doctor of Philosophy.

Signed:

Yuping Zeng, Ph.D.
Member of dissertation committee

ACKNOWLEDGMENTS

“It takes a village to raise child,” or at least get a grad student through her PhD program. Many people have helped me on my academic journey, and I would like to take a moment thank them.

To my lab mates, thank you for providing a supportive environment. Special thanks to Mr. Tom Lum and Mr. Michael Richards for allowing me to use their experimental work in my dissertation.

To UD ECE’s administrative staff, thank you for providing support to us students. Ms. Debby Nelson was invaluable in ensuring a smooth undergraduate career and I hope she is enjoying a good retirement! Ms. Gwen Looby has been equally helpful during my graduate program. Thank you for helping me get the right paperwork in for both UD and to maintain my SMART scholarship.

To Dr. Mark Mirotznik, who is the reason I entered UD’s electrical engineering program as an undergraduate. I’m deeply grateful for his support throughout my entire academic journey, from offering me a summer job when I was first starting at Harford Community College to overseeing my graduate program. Thanks for being here for the long haul.

To Chris, Estella, and Lachelle, you guys are great. Thanks for all your love and support (and cat pictures) while I’m beating my head against MATLAB. Love you guys.

And finally, to my parents, Janet and Jim Jensen. My parents have always fostered a love of science and learning to enjoy “not knowing what the heck is going

on.” Thank you for your unwavering love and support throughout my entire life. Love you!

TABLE OF CONTENTS

LIST OF TABLES	ix
LIST OF FIGURES	x
ABSTRACT	xvi
 Chapter	
1 INTRODUCTION	1
1.1 Motivation	1
1.2 Brief Background on Metamaterials and Metasurfaces	2
1.3 Original Contributions	8
1.4 Dissertation Outline	9
2 BACKGROUND IN COMPUTATIONAL ELECTROMAGNETICS	12
2.1 Computational Electromagnetics Solvers	12
2.2 Electric Field Integral Equation Using Method of Moments	14
2.2.1 Derivation of the EFIE and Related Parameters	15
2.2.1.1 EM Background	15
2.2.1.2 The Wave Equation	18
2.2.1.3 Boundary Conditions	21
2.2.1.4 Electric Field Integral Equations	23
2.2.1.5 Impedance Sheet Approximation	25
2.2.1.6 Radar Cross Section	25
2.2.1.7 Extinction	28
2.2.2 Method of Moments	29
2.3 Particle Cloud Model	31
2.4 Conclusion	33
3 MODELING A METAL PATTERNED FLAKE	34
3.1 Overview of the Shape Synthesis Concept for Particle Scattering	34
3.2 Method of Moments Applied to a Patterned Flake	37

3.2.1	Method of Moments Applied to a PEC Plate	38
3.2.2	Polarized Incident Field.....	44
3.2.3	Scattering Parameters	46
3.3	Efficient Impedance Matrix Formulation	46
3.4	Model Validation.....	52
3.4.1	Fully Metallized Square Plate	52
3.4.2	Patterned Square Plate	54
3.5	Overview of Optimization Procedure.....	56
3.5.1	Optimizers	57
3.5.1.1	Pattern Search.....	58
3.5.1.2	Genetic Algorithm	58
3.5.1.3	Particle Swarm.....	59
3.6	System	59
3.7	Summary.....	60
4	COMPUTATIONAL RESULTS	61
4.1	Optimization of Co-polarized Backscattering from Patterned Plates.....	62
4.1.1	Backscattered Optimization of Patterned Flakes at a Single Frequency – Assumes Perfect Registration	64
4.1.2	Backscattered Optimization of Patterned Flakes at a Single Frequency – Assumes No Registration	75
4.1.3	Backscattered Optimization of Patterned Flakes at a Single Frequency – Partial Registration	77
4.1.4	Backscattered Optimization of Patterned Flakes at Multiple Frequencies.....	79
4.1.5	Effects of Finite Conductivity on Backscattered Optimized Patterns	85
4.1.6	Summary of Computational Results for Backscatter	87
4.2	Optimization of Co-polarized Forward Scattering from Patterned Plates	88
4.2.1	Forward Scattered Optimization of Patterned Flakes at a Single Frequency	88
4.2.2	Forward Scattered Optimization of Patterned Flakes at Multiple Frequency	98

4.2.3	Effects of Finite Conductivity on Forward Optimized Patterns	102
4.2.4	Summary of Results for Optimizing Forward Scattering Patterns	103
4.3	Optimization of Co and Cross-Polarized Back Scattering	104
4.3.1	Optimization Schemes for Co- and Cross-Polarized Backscattering	104
4.3.2	Symmetric Designs with No Ratio Control for Co- and Cross-polarized Backscattering	105
4.3.3	Symmetric Designs with Ratio Control for Co- and Cross-polarized Backscattering	106
4.3.4	Non-symmetric Designs with Ratio Control for Co- and Cross-polarized Backscattering	106
4.3.5	Results of the Optimized Co- and Cross-polarized Backscattering Patterns	107
4.3.6	Effects on Finite Conductivity on Co and Cross-polarized Backscattering Optimized Patterns.....	117
4.3.7	Summary of Results for Optimizing Patterns for Co and Cross-Polarized Backscattering	118
4.4	Concluding Remarks	118
5	EXPERIMENTAL VALIDATION.....	120
5.1	Fabrication of Patterned Particles.....	120
5.2	Metrology Results	122
5.3	Particle Cloud Chamber	127
5.4	Experimental Results.....	130
5.5	Comparison of Experimental Results to Computational Predictions	134
5.6	Conclusion.....	136
6	CONCLUSION AND FUTURE WORKS.....	137
	REFERENCES	142

LIST OF TABLES

Table 3.1: Timing for solving matrix equations	52
Table 3.2: Percent difference between custom code and FEKO	53
Table 4.1: 1.49898cm Plate Lengths in term of wavelength	80
Table 4.2: 1.1530cm Plate Lengths in term of wavelength	82
Table 4.3: 1.1530cm Plate Lengths in terms of wavelength	85
Table 5.1: Measured abs(S21) for both fully flooded and patterned particles	133
Table 5.2: EF of measured and computational prediction of patterned particles	135

LIST OF FIGURES

Figure 1.1: Split ring resonator fed by copper wire.....	3
Figure 1.2: Ziolkowski’s Z-antenna shown on right [4]. Size comparison to an equivalent horn antenna shown on the left.....	4
Figure 1.3: Illustrative example of novel antenna designed using antenna shape synthesis methods [17]	5
Figure 1.4: Illustration of shape syntesis concepts applied to scattering from small particles	6
Figure 1.5: Illustration of random cloud of printed metasurface flakes. The metallic pattern is designed to maximize the scattering over a band of frequencies over all incident angles and polarization states.....	7
Figure 2.1: Tangential boundary components [7]	22
Figure 2.2: Scattering off a PEC a) an incident field approaching a PEC scatterer b) the incident field inducing J_s c) J_s generating a scattered field.....	24
Figure 3.1: Illustration of square flakes with patterned metal. The metallic pattern is designed to maximize scattering over a band of frequencies over all incident angles and polarization states.	36
Figure 3.2: Illustration of optimization algorithm which iteratively tests printed patterns until an optimal design is reached.	37
Figure 3.3: Meshing of the square plate	38
Figure 3.4: Roof-top basis function.....	40
Figure 3.5: Defining (x_m, y_n) for B_{xn} (right) and B_{yn} (left)	40
Figure 3.6: Razor-blade function.....	41
Figure 3.7 Incident and scattered wave polarization [33]	45
Figure 3.8 Illustration of the coupling, Z_{ij} , within the impedance matrix.	48

Figure 3.9: Removing cells from the impedance matrix	49
Figure 3.10: Corner fix	50
Figure 3.11 Enforcing symmetric patterns reduced the computational time for the design algorithms.	51
Figure 3.12: Plate average monostatic RCS (MATLAB vs FEKO)	53
Figure 3.13: Average monostatic RCS at $\varphi = 0$ of full 0.3λ plate.....	54
Figure 3.14: Patterned plate with side length of 0.3λ	54
Figure 3.15: Average monostatic RCS plotted in a. FEKO and b. MATLAB of pattern 0.3λ plate.....	55
Figure 3.16: Average monostatic RCS at $\varphi = 0$ of pattern 0.3λ plate	55
Figure 3.17: Flow diagram describing the optimization algorithm used.....	57
Figure 4.1: Illustration of the coordinate system used to calculate a single particle's backscatter or mono-static RCS.	63
Figure 4.2: Optimization grid. Pixels in the red triangle are reflected throughout the pattern. Yellow is PEC, and blue is free space.....	65
Figure 4.3: Optimized backscattering patterns using co-polarized monostatic RCS where yellow represents PEC and blue represents free space.....	68
Figure 4.4: Average Monostatic RCS over a range of plate lengths	68
Figure 4.5: $EF = \sigma_{pattern}\sigma_{plate}$	69
Figure 4.6: Plots of the monostatic RCS of plate length of $L = 0.2\lambda$ for $\sigma_{\theta\theta}$ for a. a plate, b. an optimized pattern, $\sigma_{\phi\phi}$ for c. a plate, and d. an optimized pattern.....	70
Figure 4.7: Plots of the monostatic RCS of plate length of $L = 0.5\lambda$ for $\sigma_{\theta\theta}$ for a. a plate, b. an optimized pattern, $\sigma_{\phi\phi}$ for c. a plate, and d. an optimized pattern.	71
Figure 4.8: $\sigma_{\theta\theta}$ plotted at $\phi = 0, \theta \in [0, 90]$ for $L \in [0.1\lambda, 1.5\lambda]$	72
Figure 4.9: Comparing the average RCS with the optimized angles vs increasing the angles.....	73

Figure 4.10: EF of optimized incident angles vs more incident angles.....	74
Figure 4.11: a. Runtimes and b. number of generations for the algorithm to find an optimized pattern.....	74
Figure 4.12: Illustration of optimization algorithm, which iteratively tests printed chaff patterns until an optimal design is reached. This algorithm was modified from the original one to account for random lateral shifts of the pattern (or random registration) during fabrication.....	75
Figure 4.13: a. Optimized pattern showing lateral movement occurring during optimization b. average monostatic RCS at each lateral movement point.....	76
Figure 4.14: Optimized Pattern with some registration. Yellow is PEC and blue is free space.....	78
Figure 4.15: Average monostatic RCS normalized by full metal plate as a function of lateral movement.....	79
Figure 4.16: Cost function evaluations for 7-13GHz, plate length of 1.4989cm.....	81
Figure 4.17: Optimized pattern for a plate length 1.4989cm at 7-13GHz where yellow is PEC and blue is free space.....	81
Figure 4.18: Plate length $L = 1.4989\text{cm}$ optimized over [7,9,10,11,13] GHz a. Average monostatic RCS and b. EF over extended frequency range	82
Figure 4.19: Cost function evaluations for 7-13GHz, plate length of 1.1530cm.....	83
Figure 4.20: Optimized pattern for a plate length 1.1530cm at 7-13GHz where yellow is PEC and blue is free space.....	84
Figure 4.21: Plate length $L = 1.1530\text{cm}$ optimized over [7,9,10,11,13] GHz a. Average monostatic RCS and b. EF over extended frequency range 5 GHz to 15 GHz.....	84
Figure 4.22: Average monostatic RCS of optimized patterns with impedance effects	86
Figure 4.23: Impedance effect on EF of optimized patterns	86
Figure 4.24: Optimized forward scatter patterns for plate length $L \in [0.1\lambda, 1.5\lambda]$. Yellow is PEC, blue is a free space.....	91

Figure 4.25 a. C_{extavg} over a range of plate lengths b. Zoomed in view over 0.1λ to 0.5λ	91
Figure 4.26: $EF = C_{extpattern}C_{extplate}$	92
Figure 4.27: C_{ext} is plotted for the optimized pattern at $L = 0.2\lambda$ a. Plate's $C\theta\theta$ b. Patterns's $C\theta\theta$ c. plate's $C\phi\phi$ d. Patterns's $C\phi\phi$	93
Figure 4.28: C_{ext} is plotted for the optimized pattern at $L = 0.5\lambda$ a. Plate's $C\theta\theta$ b. Patterns's $C\theta\theta$ c. plate's $C\phi\phi$ d. Patterns's $C\phi\phi$	94
Figure 4.29: The RCS of the optimized forward scatterer vs. the optimized backscatter patterns	95
Figure 4.30 The RCS of the optimized forward scatterer vs. the optimized backscatter patterns	96
Figure 4.31: Comparing average C_{ext} of optimized angles vs increasing angles	97
Figure 4.32: EF of optimized incident angles vs more incident angles.....	97
Figure 4.33: Optimized forward scatter a. runtime and b. number of generations.....	98
Figure 4.34 Cost function evaluations for 7-13GHz, plate length of 1.4989cm	99
Figure 4.35 Optimized pattern for a plate length 1.4989cm at 7-13GHz where yellow is PEC and blue is free space.....	99
Figure 4.36 The $L=1.4989$ pattern's a. average C_{ext} b. EF plotted from 5GHz to 15GHz	100
Figure 4.37: Cost function evaluations for 7-13GHz, plate length of 1.1530cm	101
Figure 4.38: Optimized pattern for a plate length 1.1530cm at 7-13GHz where yellow is PEC and blue is free space.....	101
Figure 4.39: The $L=1.1530$ cm pattern's a. average C_{ext} b. EF plotted from 5GHz to 15GHz	102
Figure 4.40: Impedance effects on the single frequency optimized patterns a. The average C_{ext} at each length b. a zoomed-in view for $L \in [0.1, 0.5]$ and c. The EF	103
Figure 4.41: Symmetric patterns and no attempt at ratio control varying between 0.1λ to 0.5λ lengths. Yellow is PEC and blue is free-space.....	108

Figure 4.42: Symmetric patterns and ratio control ($9 < \sigma_{co}\sigma_{cross} < 11$) varying between 0.1λ to 0.5λ lengths. Yellow is PEC and blue is free-space. ..	109
Figure 4.43: Non-symmetric patterns and ratio control ($9 < \sigma_{co}\sigma_{cross} < 11$) varying between 0.1λ to 0.5λ lengths. Yellow is PEC and blue is free-space	110
Figure 4.44: a. Average co-polarized RCS and b. EF for no ratio control with symmetry, ratio control with symmetry, ratio control with no symmetry, optimized co-polarized designs	111
Figure 4.45: a. Average cross-polarized RCS and b. EF for no ratio control with symmetry, ratio control with symmetry, ratio control with no symmetry, optimized cross-polarized designs.....	112
Figure 4.46: Cost function for co- and cross-polarized RCS schemes.....	113
Figure 4.47: Co- and cross-polarized a. run times and b. number of generations.....	113
Figure 4.48: RCS for an optimized non-symmetric plate with length $L = 0.2\lambda$ a. $\sigma_{\theta\theta}$ a. $\sigma_{\theta\phi}$ a. $\sigma_{\phi\phi}$	115
Figure 4.49: RCS for an optimized non-symmetric plate with length $L = 0.5\lambda$ a. $\sigma_{\theta\theta}$ b. $\sigma_{\theta\phi}$ c. $\sigma_{\phi\phi}$	116
Figure 4.50 Impedance effects on a. the average σ_{co} b. co-polarized EF c. the average σ_{cross} and d. cross-polarized EF for non-symmetric plates ..	117
Figure 5.1: Pattern and fully flooded flakes	121
Figure 5.2: Printed chaff particle optimized for maximum scattering return assuming no registration.....	122
Figure 5.3: Registration error visible using Keyence VK-3000 laser confocal system.....	123
Figure 5.4: Patterned chaff test particle 1 at 50 times zoom for Thickness measurement.....	123
Figure 5.5: Skin depth at 35 GHz as a function of metal conductivity. Solid red line indicates the measured average thickness of the printed metal chaff....	125

Figure 5.6: Fully flooded chaff particles at 5 times zoom showing the surface roughness of the printed metal materials a. and b. show two different chaff particles	126
Figure 5.7: Roughness profile of chaff test particle	126
Figure 5.8: Experimental setup for measuring RCS of chaff particles.....	127
Figure 5.9: Diagram of particle chamber	128
Figure 5.10: Experimental setup for measuring RCS of chaff particles. Three independently controlled blower fans are used for suspending particles in space during RF testing	129
Figure 5.11: Images of chaff cloud chamber suspending particles during a test and the transmission results on the VNA.....	130
Figure 5.12: Images of chaff cloud chamber suspending particles during a test. The total weight of chaff particles placed in the system varied from 0.25 grams to 1.75 grams to demonstrate how various concentration of particles can be suspended.	131
Figure 5.13: Results for fully flooded chaff particles (3 mm x 3mm in dimensions). Measurements were conducted from 26 GHz to 40 GHz over a 45 second time frame. Here the transmission magnitude in dB is displayed in a color plot as a function of frequency (x-axis) and time (y-axis). The yellow portion indicates a high level of transmission (i.e., small degree of scattering) while the blue regions indicate increased scattering. The different plots are experiments on the same particles but increasing concentrations.....	132
Figure 5.14. Transmission results for fully flooded chaff particles (3 mm x 3mm in dimensions) verses patterned particles of the same size. For these experiments the same concentration of both particles was used. Also shown are plots of the mean transmission averaged over the time frame of 15 to 45 seconds.....	133

ABSTRACT

Metamaterials and metasurfaces are well-studied in the scientific community. They allow for unusual material properties over a wide range of engineering applications that would not otherwise be achievable. One interesting application is electromagnetic scattering from small particles. Past manufacturing capabilities limited interest in this study. However, current manufacturing technologies allow the creation of small particles with complex metallic patterns. Finding patterns that can minimize or maximize scattering is of general interest. Unfortunately, existing general-purpose commercial software packages are not well suited to finding optimized pattern designs that have any complexity due to the long computation times. A custom computational electromagnetic algorithm developed for this purpose is thus needed.

In this dissertation, I present a computationally efficient custom electromagnetic solver used to find optimized patterns that either enhance or reduce scattering at a desirable frequency range. My approach, which is based on the standard method of moments (MoM) algorithm, allows for a computationally efficient rigorous solution from planar flakes with complex printed metallic patterns. This computationally efficient method was integrated within well-known iterative optimization algorithms (genetic algorithm, particle swarm, pattern search, etc.) to arrive at patterns with improved scattering properties. This technique was applied to three cases 1) maximizing the backscattering through the co-polarized radar cross

section (RCS), 2) minimizing the forward scattering through the co-polarized C_{ext} , and 3) maximizing the backscattering through co- and cross-polarized RCS. For each case electrically small particles as small as 0.2 wavelengths on a side were found that significantly enhanced scattering compared to metal flakes of the same size. The algorithms were generalized to include material effects such as finite conductivity metals to evaluate potential performance degradation and glide symmetry to arrive at patterns that are less sensitive to registration errors that occur during fabrication. A particle cloud model was also developed to predict scattering from a cloud of randomly oriented particles. Lastly, one of the most promising particle designs was fabricated and tested in a custom make particle cloud chamber providing experimental validation.

Chapter 1

INTRODUCTION

1.1 Motivation

Metamaterials have gained increased interest among the scientific community over the last decade with their unique electromagnetic properties. Beyond their ability to achieve unusual properties, such as a negative refractive index, the flexible design nature of metamaterials has fostered their exploration of a wide range of engineering applications. Many of these applications are not easily accomplished using conventional materials. *One intriguing application is the use of metamaterials, or metasurfaces, to either reduce or enhance electromagnetic scattering.* A popular specific application along these lines is the design of metamaterial coatings for electromagnetic cloaking of structures [1-3]. *In this research, I have studied the use of metasurfaces to optimize electromagnetic scattering from electrically small particles ($0.1\lambda < L < 1\lambda$ where L is the length of the a particle).* Specifically, with improvements in modern printing technologies, it is now feasible to manufacture small flake-like particles with complex metallic patterns. This technology has numerous commercial and military applications, including the ability to retro-reflect or attenuate electromagnetic energy over a broad range of incident angles and frequencies. Designing particles that achieve desirable scattering properties is a challenging computational task. It is even more difficult for electrically small particles that are only a fraction of the wavelength in size. Since general-purpose commercial codes are not well suited, it is necessary to explore new rigorous electromagnetic scattering

models and optimization schemes. The specific research goals of this research were, (1) develop new computationally efficient electromagnetic models that can be used to predict the scattering and retro-reflecting properties of patterned planar metallic particles, (2) to develop iterative optimization algorithms that can be used to design/optimize particles and (3) validate my designs both numerically and experimentally.

To this end, I have combined several novel theoretical, computational, and experimental methods to accomplish the research goals. Specifically, these are; (1) I have developed an iterative design algorithm that leverages shape synthesis methods to create unique metasurface patterns, (2) I have developed custom rigorous electromagnetic solvers based on the method of moments (MOM) that allows for orders of magnitude improvements in the total computational time needed to achieve metasurface designs and (3) I have experimentally validated my design approach using novel fabrication and experimental characterization systems.

1.2 Brief Background on Metamaterials and Metasurfaces

Metamaterials are artificial structures that bend electromagnetic waves in non-intuitive ways using subwavelength structures. The field of metamaterials as we know it today began with Veselago proposing negative refraction in 1968. His theoretical approach was more interested in discussing what would happen if such materials existed. It was not until many years later that groups would physically realize these structures [1,2]. These earlier pioneers found that Veselago's theoretical negative refractive index material could be achieved by periodically repeating sub-wavelength unit cell structures. An example is shown in figure 1.1 where a split ring resonator powered by a copper wire is repeated [1].



Figure 1.1: Split ring resonator fed by copper wire

At first, there was much public interest in these new materials because negative refractive index implied the possibility of “invisibility devices.” No cloaking over the entire visible region has been achieved to date, however, metamaterials found uses in other applications. One of Pendry’s original applications of negative refractive index materials was for superlenses. His group found that a negative refractive index slab had better resolution than classical optical materials [1]. Other applications include dual-band antennas, frequency-selective surfaces, artificial magnetic conductors, and flat lenses.

The size of structures in the above work tends to be large compared to the wavelength, even though the individual unit cell is small. Recently there has been research exploring new “metamaterial-inspired” structures. For example, some investigators have found that a single metamaterial unit cell can achieve desirable impedance-matching properties at a narrow band of frequencies and, thus, significantly reduce the size of an equivalent traditional antenna. Figure 1.2 shows a traditional horn antenna next to Ziolkowski’s Z-antenna [4]. This concept is based on metamaterial transmission line structure.

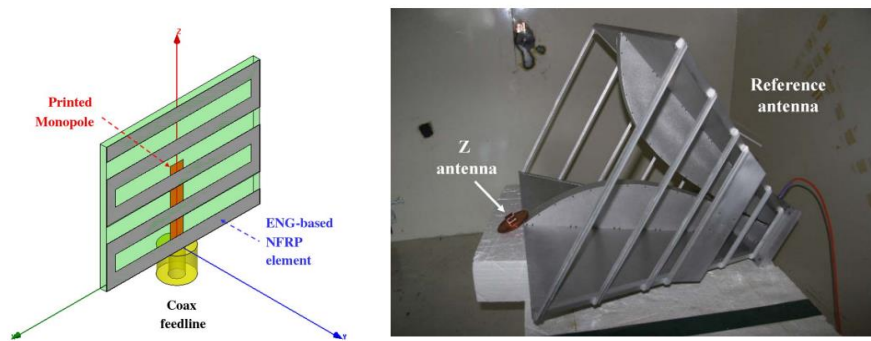


Figure 1.2: Ziolkowski's Z-antenna shown on right [4]. Size comparison to an equivalent horn antenna shown on the left

Wang et al. [5] created a low-Q wide beamwidth circularly polarized antenna using two-hybrid small magnetic dipoles fed by a metal screw. These small structures have other applications as well. Bilotti et al. [6] moved away from antennas and explored scattering from coated cylinders in hopes of creating cloaking devices. All of this research focuses on simple shapes that are either analytically solvable or well-suited for commercial software packages (e.g., HFSS, FEKO, COMSOL, etc).

Antenna synthesis is defined as any technique used to design an antenna system to yield desired radiation characteristics [7]. Classic examples of this include Schelkunoff's method for null placement in beam forming [8-10], Woodward-Lawson's method for beam shaping [11-13], and Dolph-Tschebyscheff's method for narrow beams and low sidelobes [14,15]. Advancements in computational electromagnetics have led to a new area of this field coined "Antenna shape synthesis." As the name suggests, the shape of the antenna is changed to tune the radiation properties. This is generally a metallic object [17-22] where iterative solvers create geometries that optimize some property of the radiation characteristics (e.g., gain, bandwidth, etc.). An example is shown in Figure 1.3. Here the investigators used

shape synthesis methods to design an unusual antenna surface in which the gain and bandwidth were co-optimized over some desirable ranges [17].

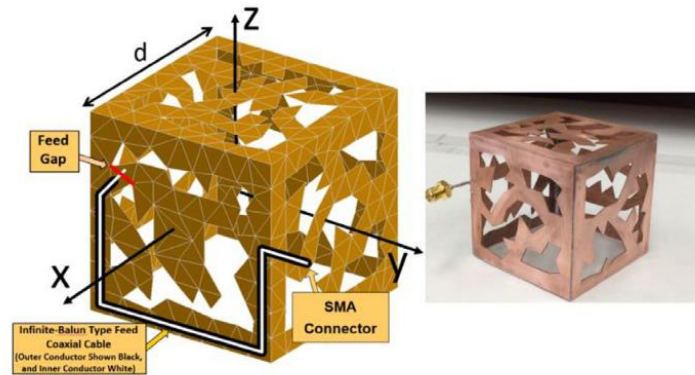


Figure 1.3: Illustrative example of novel antenna designed using antenna shape synthesis methods [17]

In this research, I extend the concepts used in antenna shape synthesis to design patterned surfaces that optimize electromagnetic scattering from electrically small thin flakes. Here I define a surface as an array of “pixels” in which metal can be applied or removed at each pixel to alter the scattering properties. An illustration of this concept is shown in figure 1.4. The goal is to optimize the pattern of metallic pixels to optimize scattering over a desirable range of incident angles, polarization states, and frequencies. This could be applied to maximizing the total scattering cross-section, backscatter, cross-polarized, or forward scattering.

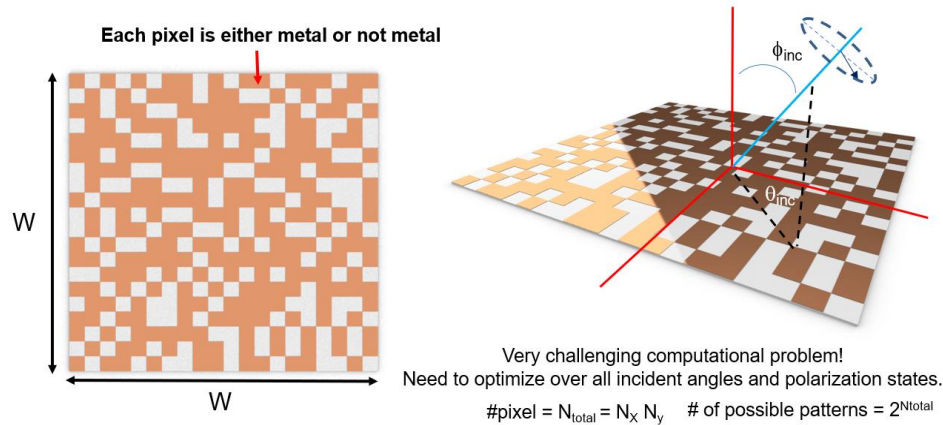


Figure 1.4: Illustration of shape synthesis concepts applied to scattering from small particles

The brute force method to design an optimal pattern would consider all possible variations. A simple example will show why this is not feasible. Consider a scattering problem where 3600 incident angles are considered (60 in ϕ and 60 in θ), both polarizations (TM and TE), and five discrete frequencies. Commercial software such as HFSS or FEKO can be used to generate a solution for each pattern. However, it must generate the pattern each time, create a mesh and solve for the radiated fields. Consider that for each change in a parameter, the model takes 0.01 seconds to solve. A single pattern would therefore take 360 seconds for all incident angles, polarization states, and frequencies. For a 121-pixel square (11 by 11), there would be 14641 possible patterns. Solving for all possible solutions would take 61 days! This is clearly not practical.

Two major computational challenges must be addressed for this approach to be practical. First, modern iterative optimization algorithms are needed to arrive at an optimal pattern without searching through all possible patterns. A wide range of optimization algorithms has been developed for this purpose. These include gradient

descent methods, genetic algorithms, pattern search, and particle swarm optimization. All of these techniques have various advantages and disadvantages depending on the specific application. This is discussed in more detail in Chapter 3. The second major challenge is developing a custom electromagnetic solver that is tuned for the particular application. The goal is to generate accurate predictions in a short amount of time compared to current solvers. Commercial codes are prohibited for this application due to the relatively long computation times required due to their overhead. My particular solution to this challenge, discussed in detail in Chapter 3, reduced the optimization time from weeks to hours. Once a single particle design is optimized, the final goal is to predict scattering from a cloud of these particles randomly distributed within some volume (see Figure 1.5). To that end, I developed a simple cloud model that could predict scattering from the optimized particles for various particle densities.

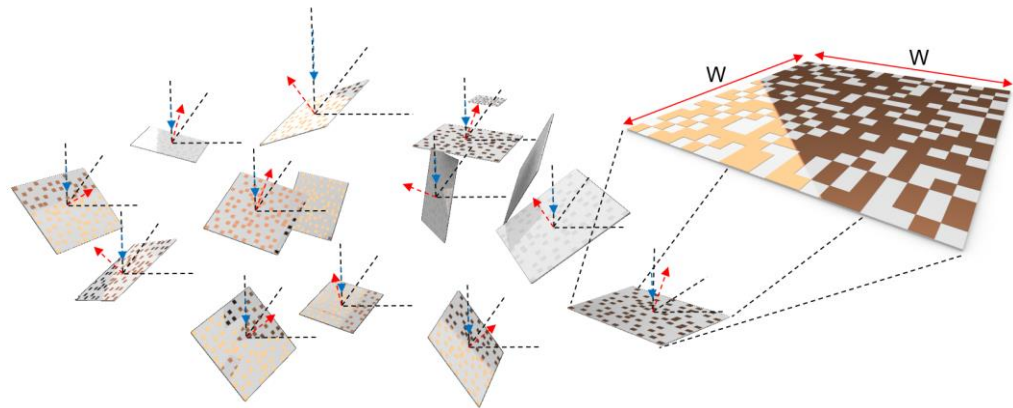


Figure 1.5: Illustration of random cloud of printed metasurface flakes. The metallic pattern is designed to maximize the scattering over a band of frequencies over all incident angles and polarization states.

1.3 Original Contributions

This thesis offered several original contributions related to the development of computational methods for the optimal design of geometrically complex particles with desirable scattering properties. These include;

- A custom-developed method-of-moments (MoM) based algorithm for efficiently calculating electromagnetic scattering from complex planar metallic patterns.
- An iterative optimization algorithm that uses antenna shape synthesis techniques to enhance or minimize the scattering from electrically small square particles.
- A cloud model to predict scattering from a random distribution of patterned particles.
- A novel method for experimental validation of the computational results.

In addition to the methods described above, several novel results were obtained. These included;

- Optimal patterns were designed that demonstrated enhanced backscatter and extinction cross-sections of electrically small particles. Specifically, patterned surfaces were designed that showed over a 40 times enhancement in scattering from particles as small as 0.2 wavelengths on a side compared to metal plates of the same dimensions.
- Optimal patterns were designed that enhanced the cross-polarized scattering from electrically small particles (<0.25 wavelengths) by a factor of over 25,000 compared to a metal plate of the same dimensions.
- Optimal patterns that included glide-symmetry were designed to account for fabrication errors in pattern registration during printing.

- The effect of finite conductivity metal on scattering performance was modeled for patterned and fully metalized flakes. The results demonstrated the need for high conductivity and reasonably thick print layers to ensure conductive layers with an adequate skin depth.

This research will result in the following publications:

1. Jensen S., Lum T., Richards M., Mills K., Kaplan D. and Mirotznik M.S., “Shape Synthesis Algorithms Applied for the Design of Electrically Small Particles with Enhanced Electromagnetic Scattering”, to be submitted at the **Defense Technical Information Center Journal (DTIC)**, 2022
2. Jensen S., Lum T., Richards M., Mills K., Kaplan D. and Mirotznik M.S., “Experimental Validation of Enhanced Scattering from Electrically Small Metasurface Particles”, to be submitted at the **Defense Technical Information Center Journal (DTIC)**, 2022.
3. Jensen S., Lum T., Richards M., Mills K., Kaplan D. and Mirotznik M.S., “Electrically Small Metasurface Particles with Enhanced Cross-polarization Scattering”, to be submitted at the **Defense Technical Information Center Journal (DTIC)**, 2022.

1.4 Dissertation Outline

This section provides an outline of this dissertation. In Chapter 2, I provide the necessary background in computational electromagnetics and scattering theory relevant for the research described in the subsequent chapters. It begins from first principles, starting with Maxwell’s equations and working towards the well-known Electric field Integral Equation (EFIE). The three full wave solvers: finite difference time domain (FDTD), finite element method (FEM), and Method of Moments (MoM)

are then discussed. MoM is shown to be the best choice for scattering problems and is used to discretize the EFIE. Finally, the radar cross section (RCS) and extinction (C_{ext}) for a generalized MoM are derived. I also provide background on the cloud model used to predict scattering from a random distribution of particles.

Chapter 3 presents the specific computational models developed during this research. The chapter begins with deriving the MoM for a flat PEC plate. A square-cell model is used rather than a normal triangular mesh to allow pixelation of the plate. The surface current coefficients are derived, and the scattering parameters, RCS and C_{ext} , are given in terms of the surface current coefficients. It is then shown how the shape of the plate can be modified by removing values from the impedance matrix \mathbf{Z} . Next, the model is generalized to non-PEC material properties using the impedance sheet approximation. Finally, the model is numerically validated using a commercially available MoM software program (FEKO). This chapter also provides a background on the various optimization algorithms used for the iterative design (i.e., genetic algorithms, pattern search optimization, and particle swarm optimization).

In Chapter 4, I present the computational results. These include metasurface designs that optimized co-polarized backscatter at a single frequency, co-polarized extinction at a single frequency, cross-polarized backscatter at a single frequency, and co-polarized backscatter and extinction over a band of frequencies. This chapter also provides computational results on the particles designed with glide-symmetry and the effect of finite conductivity (i.e., surface impedance).

In Chapter 5, I present experimental validation using a novel custom-built particle cloud chamber. The final chapter summarizes the thesis's important findings

and discusses similarities found in optimized patterns. A brief discussion is given on potential future research areas to continue this work.

Chapter 2

BACKGROUND IN COMPUTATIONAL ELECTROMAGNETICS

This chapter reviews relevant topics in computational electromagnetics (CEM) used for this research. An overview of the three full-wave solvers is given in section 2.1. Method of Moments (MoM) is shown to be the optimal choice when dealing with scattering problems. Section 2.2 seeks to derive the Electric Field Integral Equation (EFIE) from the first principles, leading to a derivation of the MoM applied to the generalized scattering problem. The chapter concludes with a description of a particle cloud model that is useful for scattering from the distribution of random scatterers.

2.1 Computational Electromagnetics Solvers

Three options for full wave solvers exist in computational electromagnetics: Method of Moments (MoM), Finite Difference Time Domain, (FDTD), and Finite Elements Methods [23]. An brief overview of these is presented here.

MoM begins with the integral form of Maxwell's equations that includes the appropriate Green's function. The continuous integrals are discretized by approximating continuously varying variables, such as electric currents, by a sum of basis functions. Surface currents are used to replace the radiating surface/scattering structure. By applying boundary conditions, a linear system of equations can be found and solved using the method of weighted residuals. The benefit of this approach is that only the scatterer needs to be meshed and not the surrounding space, thus reducing

computational time and memory requirements. MoM is an efficient method for modeling surface effects. While MoM can be applied to volumetric models, this can be computationally expensive, and other solvers should be considered.

FDTD and FEM both use the differential form of Maxwell's equations and generally solve directly for the electric \vec{E} and magnetic \vec{H} fields. This requires the entire region of interest to be meshed. This is an effective approach for inhomogeneous materials where surface currents cannot fully represent the model. FDTD directly approximates Maxwell's curl equations in the time domain using a staggered grid in time and space. Within the solvers discussed here, it is the only way to consider time and allow modeling of wave propagation through space and obstructions.

The third general CEM approach is FEM which begins with Maxwell's equations in the partial differential equation form. The models follow a similar scheme to MoM using weighted residuals. FEM handles two different classes of problems; eigenanalysis (source-free) and deterministic (driven). Eigenanalysis is when there is no source, the model is just looking for resonant frequencies such as a cavity resonator. Deterministic is any model with a source and is used for antennas, periodic structure analyses, and microwave circuits. Like FDTD, FEM is a volumetric approach and thus can be memory and time expensive for many scattering problems.

MoM was chosen as an optimal approach to developing the predictive models presented in this dissertation. The geometric model, thin metalized flakes, would require a fine volume mesh that makes a FEM and FDTD approach computationally burdensome. Adding in surrounding space would exacerbate this problem. MoM will be explored more fully in the following sections.

2.2 Electric Field Integral Equation Using Method of Moments

This section provides a foundation in the use of Method of Moments for Electromagnetic (EM) scatterers beginning with the necessary background in electromagnetic theory. It then moves on to define the wave equations and gives the framework needed for a computational solution. The solution to the wave equation can be found directly. However, it is more common to define auxiliary vector functions $\bar{\mathbf{A}}$ and $\bar{\mathbf{F}}$. These mathematical tools with no physical meaning are used here to ease the mathematical burden. The auxiliary functions will be solved using a Green's Function approach. The electric and magnetic fields can be found later. The solution to these functions necessitates boundary conditions. The model builds a predictive description for wave interactions with the scatterer. Boundary conditions are derived once again from Maxwell's equations. Next, the EFIE will be derived. This forms the defining equation that can predict the behavior of electromagnetic scatterers in MoM models. Finally, the section discusses the radar cross-section and extinction coefficient. The predictive model developed in this thesis optimizes these values.

Generally, the EFIE cannot be solved analytically except for the simplest of canonical problems. Instead, computational methods are needed. I will show how the EFIE can be discretized in section 2.2.2. For that solution, the scatterer is meshed to create discrete points. The current is expanded at these points as a series of functions and then weighted to create N-equations for N-unknowns. An understanding of these functions and what they physically model will be explained. The plate geometry fully described in the impedance matrix is of particular importance to this work. The optimization algorithm exploits this fundamental fact to reduce computational time for iterative design. Solving for current coefficients fully solves the problem. Any other parameters, such as RCS or far field radiation patterns, can be calculated easily once

the surface currents are known. The standard EFIE assumes perfect electrical conducting (PEC) materials. However, an impedance sheet approximation can be used to introduce finite conductivity found in real materials.

The section concludes by introducing a particle cloud model. This allows for single-particle radiation to be extended into multiple randomly oriented particles acting together as a group.

2.2.1 Derivation of the EFIE and Related Parameters

The EFIE and related parameters will be derived in this section. Starting from Maxwell's Equations, the time-harmonic wave equation is derived. The small metal flakes used in this dissertation will first assume PEC boundaries where the electrical conductivity is infinite. The necessary boundary condition will then be derived. Combining the wave equation with the boundary condition, the EFIE is found. However, this equation assumed infinite conductivity (PEC), which is not found in the real world. The impedance sheet approximation adds a linear loss term to the EFIE, allowing finite conductivity to be modeled. The RCS and C_{ext} can then be found in terms of the scattered current. With this information, any generalized scatter can be modeled. The following section will present the computational method necessary to solve the derived linear equation, the EFIE.

2.2.1.1 EM Background

Advanced Engineering Electromagnetics by Constatine Balanis is a well-known reference and a staple of this field [7]; this work follows his notation.

Maxwell's equations form the foundation of electromagnetics. It is comprised of four equations: Gauss's Law, Gauss's Law for magnetism, Faraday's Law, and Ampere's Law shown in this order below:

$$\nabla \cdot \bar{\mathbf{D}} = q_{ev} \quad (2.1)$$

$$\nabla \cdot \bar{\mathbf{B}} = q_m \quad (2.2)$$

$$\nabla \times \bar{\mathbf{E}} = -\frac{\partial \bar{\mathbf{B}}}{\partial t} - \bar{\mathbf{M}}_i \quad (2.3)$$

$$\nabla \times \bar{\mathbf{H}} = \bar{\mathbf{J}}_i + \bar{\mathbf{J}}_c + \frac{\partial \bar{\mathbf{D}}}{\partial t} = \bar{\mathbf{J}}_{ic} + \frac{\partial \bar{\mathbf{D}}}{\partial t} \quad (2.4)$$

These equations relate the electric field intensity $\bar{\mathbf{E}}$ [V/m], magnetic field intensity $\bar{\mathbf{H}}$ [A/m], electric flux density $\bar{\mathbf{D}}$ [V/m²], magnetic flux density $\bar{\mathbf{B}}$ [A/m²], impressed (source) electric current density $\bar{\mathbf{J}}_i$ [A/m²], the electric conduction current $\bar{\mathbf{J}}_c$ [A/m²], impressed magnetic (source) current density $\bar{\mathbf{M}}_i$ [V/m²], electric charge density q_{ev} [C/m³], and magnetic charge density q_m [W/m³]. Magnetic current and charge do not exist in the physical world. However, the presented formulation can be used to create a solvable equivalent problem for an otherwise unsolvable problem. This form of Maxwell's equations is more useful in computational electromagnetics.

The electric field intensity $\bar{\mathbf{E}}$ and magnetic field intensity $\bar{\mathbf{H}}$ can be related to their respective flux densities ($\bar{\mathbf{D}}$ and $\bar{\mathbf{B}}$) with equations (2.5) and (2.6). Material properties are represented using the permittivity ϵ and permeability μ . The permittivity can further be expressed as a product of the permittivity of free space ϵ_0 and the relative permittivity of a particular material ϵ_r . The same is true for permeability.

$$\bar{\mathbf{E}} = \epsilon_0 \epsilon_r \bar{\mathbf{D}} = \epsilon \bar{\mathbf{D}} \quad (2.5)$$

$$\bar{\mathbf{H}} = \mu_0 \mu_r \bar{\mathbf{B}} = \mu \bar{\mathbf{B}} \quad (2.6)$$

One final equation needed is the continuity equation (2.7). This can be derived from equations (2.1) to (2.4), so is not considered a fundamental equation. It is useful for derivations to be able to relate current and charge.

$$\nabla \cdot \bar{\mathbf{J}}_{ic} = \frac{\partial q_{ev}}{\partial t} \quad (2.7)$$

Implied in equations (2.1) – (2.7) is a time and space dependency i.e. $\bar{\mathbf{E}}(x, y, z, t)$. In many real-world scenarios, the time variation is assumed to be sinusoidal. A useful mathematical approach is to transform the equation into the complex domain using Euler's formula stated in equation (2.8).

$$e^{jx} = \cos(x) + j \sin(x) \quad (2.8)$$

A sine wave is just a phase-shifted cosine, so it is inconsequential if the real or imaginary part of e^{jx} is taken. The result is just phased shifted. The convention takes the real form and the time-harmonic electromagnetic fields ($\bar{\mathbf{E}}$, $\bar{\mathbf{H}}$, $\bar{\mathbf{D}}$, $\bar{\mathbf{B}}$) can be defined as

$$\bar{\mathbf{E}}(x, y, z, t) = \text{Re}\{\bar{\mathbf{E}}(x, y, z)e^{j\omega t}\} \quad (2.9)$$

$$\bar{\mathbf{H}}(x, y, z, t) = \text{Re}\{\bar{\mathbf{H}}(x, y, z)e^{j\omega t}\} \quad (2.10)$$

$$\bar{\mathbf{D}}(x, y, z, t) = \text{Re}\{\bar{\mathbf{D}}(x, y, z)e^{j\omega t}\} \quad (2.11)$$

$$\bar{\mathbf{B}}(x, y, z, t) = \text{Re}\{\bar{\mathbf{B}}(x, y, z)e^{j\omega t}\} \quad (2.12)$$

Plugging equations 2.9–2.12 leads to the time-harmonic form of Maxwell's equations given by 2.13–2.16:

$$\nabla \cdot \bar{\mathbf{D}} = q_{ev} \quad (2.13)$$

$$\nabla \cdot \bar{\mathbf{B}} = q_{mv} \quad (2.14)$$

$$\nabla \times \bar{\mathbf{E}} = -j\omega \bar{\mathbf{B}} - \bar{\mathbf{M}}_i \quad (2.15)$$

$$\nabla \times \bar{\mathbf{H}} = \bar{\mathbf{J}}_i + \bar{\mathbf{J}}_c + j\omega \bar{\mathbf{D}} = \bar{\mathbf{J}}_{ic} + j\omega \bar{\mathbf{D}} \quad (2.16)$$

From this point forward, I will assume the time-harmonic form.

2.2.1.2 The Wave Equation

The wave equation for electric fields can be found by taking the curl of equation 2.15, recalling equation 2.6, and substituting both into equation 2.16. Likewise, the magnetic field is found by doing the reverse. These can be seen in equations 2.17-2.18.

$$\nabla^2 \bar{\mathbf{E}} + \beta^2 \bar{\mathbf{E}} = \nabla_{\mathbf{x}} \bar{\mathbf{M}} + j\omega\mu\bar{\mathbf{J}} + \frac{1}{\epsilon} \nabla q_{ev} \quad (2.17)$$

$$\nabla^2 \bar{\mathbf{H}} + \beta^2 \bar{\mathbf{H}} = -\nabla_{\mathbf{x}} \bar{\mathbf{J}} + j\omega\mu\bar{\mathbf{M}} + \frac{1}{\epsilon} \nabla q_{mv} \quad (2.18)$$

$$\beta^2 = \omega^2 \mu \epsilon \quad (2.19)$$

The wave equation can be solved directly for a given source, but this approach tends to be mathematically intensive. Instead, auxiliary vector potentials $\bar{\mathbf{A}}$ and $\bar{\mathbf{F}}$ are introduced as mathematical aids. Looking at the right-hand side for equations 2.17-2.19, you can see that each source term is separate. This means each solution can be looked at separately and then summed at the end. For the vector potential $\bar{\mathbf{A}}$, the magnetic current $\bar{\mathbf{M}}$ will be set to zero. For the vector potential $\bar{\mathbf{F}}$, the electric current $\bar{\mathbf{J}}$ is zero.

Now the auxiliary equation $\bar{\mathbf{A}}$ will be derived. By setting $q_{mv} = 0$, equation 2.14 becomes equation 2.20. By the application of well-known vector identities, some distribution $\bar{\mathbf{A}}$ must exist that satisfies equation 2.21.

$$\nabla \cdot \bar{\mathbf{B}} = 0 \quad (2.20)$$

$$\nabla \cdot (\nabla_{\mathbf{x}} \bar{\mathbf{A}}) = 0 \quad (2.21)$$

By combining equation 2.6 with equations 2.20-2.21, a relationship can be written for the magnetic field intensity $\bar{\mathbf{H}}$ shown in equation 2.22. Plugging this into Faraday's Law (equation 2.15), and simplifying results in equation 2.23.

$$\bar{\mathbf{H}}_A = \frac{1}{\mu} \nabla \times \bar{\mathbf{A}} \quad (2.22)$$

$$\nabla \times (\bar{\mathbf{E}}_A + j\omega \bar{\mathbf{A}}) = 0 \quad (2.23)$$

Because the curl expression in equation 2.23 is equal to zero a scalar function ϕ_e must exist that satisfies equation 2.24. This will be referred to as an arbitrary electric scalar potential and is a function of position. Comparing terms with equation 2.23 and rearranging values results in equation 2.25.

$$\nabla \times (-\nabla \phi_e) = 0 \quad (2.24)$$

$$\bar{\mathbf{E}}_A = -\nabla \phi_e - j\omega \bar{\mathbf{A}} \quad (2.25)$$

Equation 2.25 relates the vector potential $\bar{\mathbf{A}}$ to the electric field $\bar{\mathbf{E}}_A$. In order to achieve an equation that contains only $\bar{\mathbf{A}}$, Ampere's Law in equation 2.16 and the definition of the vector potential $\bar{\mathbf{A}}$, equation 2.22, are used. Ampere's law takes the curl of $\bar{\mathbf{H}}$, so plugging in $\bar{\mathbf{A}}$ leads to a curl of the curl of $\bar{\mathbf{A}}$. The vector identity shown in 2.26 allows the curl of the curl to be rewritten in Ampere's law as equation 2.27.

$$\nabla \times \nabla \times \bar{\mathbf{A}} = \nabla(\nabla \cdot \bar{\mathbf{A}}) - \nabla^2 \bar{\mathbf{A}} \quad (2.26)$$

$$\mu \bar{\mathbf{J}} + j\omega \mu \epsilon \bar{\mathbf{E}}_A = \nabla(\nabla \cdot \bar{\mathbf{A}}) - \nabla^2 \bar{\mathbf{A}} \quad (2.27)$$

Equation 2.25 relates the vector potential $\bar{\mathbf{A}}$ to the electric field $\bar{\mathbf{E}}_A$. To achieve an equation that is only in terms of the variable $\bar{\mathbf{A}}$, I employ Ampere's Law. Ampere's Law takes the curl of $\bar{\mathbf{H}}$, so plugging in $\bar{\mathbf{A}}$ leads to a curl of the curl of $\bar{\mathbf{A}}$. The vector identity shown in 2.26 allows the curl of the curl to be rewritten in Ampere's Law as equation 2.27.

$$\begin{aligned}\nabla^2 \bar{\mathbf{A}} + \beta^2 &= -\mu \bar{\mathbf{J}} + \nabla(\nabla \cdot \bar{\mathbf{A}}) + \nabla(j\omega\mu\epsilon\phi_e) \\ &= -\mu \bar{\mathbf{J}} + \nabla(\nabla \cdot \bar{\mathbf{A}} + j\omega\mu\epsilon\phi_e)\end{aligned}\quad (2.28)$$

Note that the curl of $\bar{\mathbf{A}}$ has been defined in equation 2.22. Without loss of generality, the divergence of $\bar{\mathbf{A}}$ can be defined arbitrarily to reduce the complexity of the problem. This is referred to as a gauge condition. The Lorenz gauge condition shown in equation 2.29 defines the divergence of $\bar{\mathbf{A}}$ such that equation 2.28 is simplified by canceling out the scalar potential ϕ_e . This leads to equation 2.30, which is an equation composed of only the auxiliary vector potential $\bar{\mathbf{A}}$ and the electric current $\bar{\mathbf{J}}$.

$$\nabla \cdot \bar{\mathbf{A}} = -j\omega\epsilon\mu\phi_e \quad (2.29)$$

$$\nabla^2 \bar{\mathbf{A}} + \beta^2 \bar{\mathbf{A}} = -\mu \bar{\mathbf{J}} \quad (2.30)$$

An equivalent set of equations can be found for $\bar{\mathbf{F}}$ by setting the electric source $q_{ev} = 0$. Specifically, by switching the appropriate variables, a solution of the same form of equation 2.30 can be found for $\bar{\mathbf{F}}$ and is summarized in equations 2.31-2.34.

$$\bar{\mathbf{E}}_F = \frac{1}{\epsilon} \nabla \times \bar{\mathbf{F}} \quad (2.31)$$

$$\bar{\mathbf{H}}_F = -j\omega \bar{\mathbf{F}} - \frac{j}{\omega\mu\epsilon} \nabla(\nabla \cdot \bar{\mathbf{F}}) \quad (2.32)$$

$$\nabla \cdot \bar{\mathbf{F}} = -j\omega\epsilon\mu\phi_m \quad (2.33)$$

$$\nabla^2 \bar{\mathbf{F}} + \beta^2 \bar{\mathbf{F}} = -\epsilon \bar{\mathbf{M}} \quad (2.34)$$

The differential equations 2.30 and 2.34 have homogenous and particular solutions. The homogenous solution occurs when the source is zero. The solution is used to represent standing waves such as those found in a waveguide. The particular solution must be obtained using the Green's function technique for scattering problems.

The Green's function is obtained by replacing the source with a phase-shifted delta function. The solution to this problem is the Green's function $G(\mathbf{r}, \mathbf{r}')$ and is shown in equation 2.35. The solution to this equation is found by integrating out the Laplacian and is given in 2.36 [24].

$$\nabla^2 G(\mathbf{r}, \mathbf{r}') + \beta^2 G(\mathbf{r}, \mathbf{r}') = -\mu \delta(\mathbf{r} - \mathbf{r}') \quad (2.35)$$

$$G(\mathbf{r}, \mathbf{r}') = \frac{\mu_0}{4\pi|\mathbf{r} - \mathbf{r}'|} e^{-jk|\mathbf{r} - \mathbf{r}'|} \quad (2.36)$$

The final solution can be found by summing up individual solutions from different sources by linear superposition. For a continuous source, the sum becomes an integral. The Green's function is the solution at particular points and can be integrated over the space of interest to form the final solution. The solution to the auxiliary equations $\bar{\mathbf{A}}$ and $\bar{\mathbf{F}}$ are given in equations 2.37-2.38 [7, 23].

$$\bar{\mathbf{A}} = \frac{\mu}{4\pi} \iiint_V \bar{\mathbf{J}}(\mathbf{r}') G(\mathbf{r}, \mathbf{r}') dv' \quad (2.37)$$

$$\bar{\mathbf{F}} = \frac{\mu}{4\pi} \iiint_V \bar{\mathbf{M}}(\mathbf{r}') G(\mathbf{r}, \mathbf{r}') dv' \quad (2.38)$$

For any currents $\bar{\mathbf{J}}$ and $\bar{\mathbf{M}}$, the auxiliary equations $\bar{\mathbf{A}}$ and $\bar{\mathbf{F}}$ can be found. The fields can be found with equations 2.22, 2.25, 2.31, and 2.32. In practice, these cannot be solved analytically for complex problems. Computational methods are needed.

2.2.1.3 Boundary Conditions

Electromagnetic waves propagate through space and, at some point, are impeded by a material surface. At that point, boundary conditions are needed to relate field values on either side of the material interface. Only the tangential boundary conditions are required for this discussion and are the only ones derived.

Faraday's Law, equation 2.15, can be rewritten in integral form using Stoke's Law and becomes equation 2.39.

$$\oint \bar{\mathbf{E}} \cdot d\bar{\mathbf{l}} = - \iint \bar{\mathbf{M}}_i - j\omega\bar{\mathbf{B}} ds \quad (2.39)$$

Place a square cylinder at the boundary of two different media. Integrate on the face of the cylinder. The line integral follows C_0 for the electric field $\bar{\mathbf{E}}$. The magnetic current $\bar{\mathbf{M}}_i$ and magnetic flux $\bar{\mathbf{B}}$ will be over the surface S_0 as shown in figure 2.1.

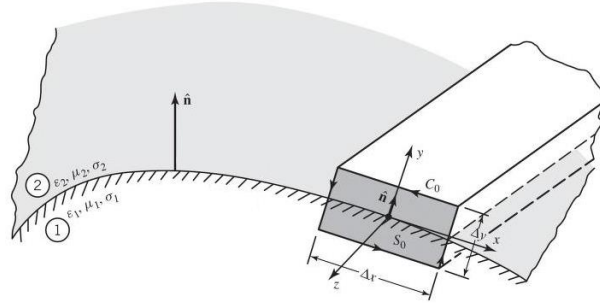


Figure 2.1: Tangential boundary components [7]

Δy , shown in figure 2.1, is taken to 0 (i.e. $\Delta y \rightarrow 0$) to collapse the problem to the surface of the media. The line integral normal to the surface, therefore, becomes zero. The dot product in the line integral can be rewritten in terms of the boundary's normal as given in equation 2.40.

$$\int \hat{\mathbf{n}} \times (\bar{\mathbf{E}}_2 - \bar{\mathbf{E}}_1) dl \quad (2.40)$$

The magnetic flux $\bar{\mathbf{B}}$ is bounded. When the surface collapses, it approaches zero, as shown in equation 2.41. The current, however, can collapse onto the interface

of the surface. This new surface current will be defined as $\bar{\mathbf{M}}_s$. The surface integral becomes a line integral, and the surface current is defined in equation 2.42.

$$\lim_{\Delta y \rightarrow 0} \iint j\omega \bar{\mathbf{B}} ds = 0 \quad (2.41)$$

$$\lim_{\Delta y \rightarrow 0} \iint \bar{\mathbf{M}}_i ds = \int \bar{\mathbf{M}}_s dl \quad (2.42)$$

Combining equation 2.39-2.42, gives us the tangential $\bar{\mathbf{E}}$ boundary condition

$$\hat{\mathbf{n}} \times (\bar{\mathbf{E}}_2 - \bar{\mathbf{E}}_1) = \bar{\mathbf{M}}_s \quad (2.43)$$

Again, the magnetic current $\bar{\mathbf{M}}_s$ is fictitious and is used in creating equivalence problems. For PEC, $\bar{\mathbf{M}}_s = 0$. The same process can be carried out to find the tangential magnetic field boundary condition and is

$$\hat{\mathbf{n}} \times (\bar{\mathbf{H}}_2 - \bar{\mathbf{H}}_1) = \bar{\mathbf{J}}_s \quad (2.44)$$

The electric current defined in equation 2.43 is a real measurable quantity when collapsing the surface. This only occurs on perfect electrical conductors (PEC) where the conductivity is taken to be infinite.

2.2.1.4 Electric Field Integral Equations

This section derives the Electric Field Integral Equation for a generalized PEC scatterer to provide a more intuitive feel of the problem before moving into a more rigorous mathematical discussion of the plate scatterer.

As an incident wave approaches, an arbitrary PEC scatterer is placed in space in figure 2.2. When the incident wave hits the surface, a surface current $\bar{\mathbf{J}}_s$ is induced, as explained in the boundary condition section. This current is itself a source that radiates a scattered field E_s . An equivalent problem containing magnetic current $\bar{\mathbf{M}}_s$ is

not needed for a PEC, so the tangential electric field boundary in equation 2.43 can be rewritten as

$$\bar{\mathbf{E}}_{total} = (\bar{\mathbf{E}}_{inc} + \bar{\mathbf{E}}_s) = 0 \quad (2.45)$$

$$\bar{\mathbf{E}}_{inc} = -\bar{\mathbf{E}}_s \quad (2.46)$$

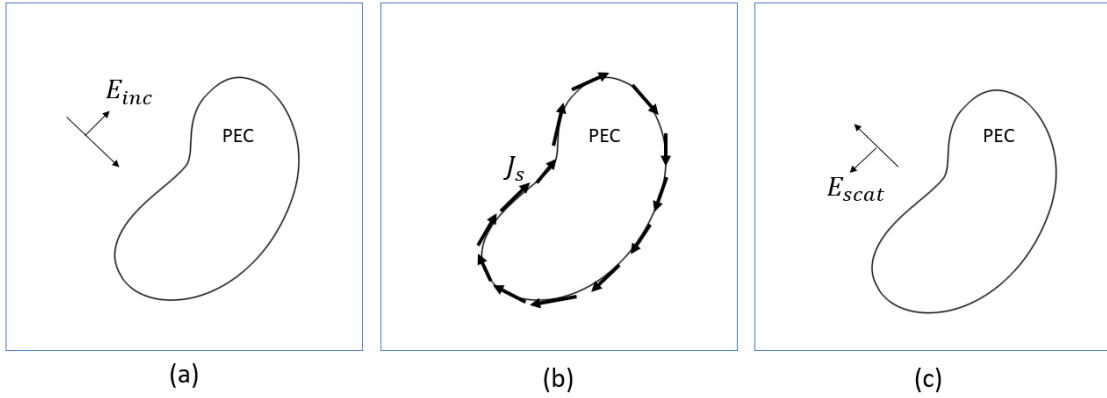


Figure 2.2: Scattering off a PEC a) an incident field approaching a PEC scatterer b) the incident field inducing J_s c) J_s generating a scattered field

In the previous discussion of the wave equation, equations 2.25, 2.29, 2.31, 2.37, and 2.38 are used to determine the induced scattered fields in terms of the surface current. Combining these equations leads to

$$\bar{\mathbf{E}}_s = \frac{\nabla\nabla \cdot \bar{\mathbf{A}} + k^2\bar{\mathbf{A}}}{j\omega\epsilon_0} - \nabla\times\bar{\mathbf{F}} \quad (2.47)$$

This is the generalized EFIE. For a PEC, there is no magnetic current, so $\bar{\mathbf{F}}$ is set to zero. Equations 2.46 and 2.47 are combined to form the equation for the scattering of a PEC surface [25].

$$\bar{\mathbf{E}}_{inc} = -\frac{\nabla\nabla \cdot \bar{\mathbf{A}} + k^2\bar{\mathbf{A}}}{j\omega\epsilon_0} \quad (2.48)$$

2.2.1.5 Impedance Sheet Approximation

For thin non-PEC materials, the linear operator in equation 2.48 for a PEC scatterer can be modified with a linear term

$$\bar{\mathbf{E}}_{inc} = -\frac{\nabla\nabla \cdot \bar{\mathbf{A}} + k^2\bar{\mathbf{A}}}{j\omega\epsilon_0} + Z_L\bar{\mathbf{J}}_s \quad (2.49)$$

$$\bar{\mathbf{E}}_{inc} = L(\bar{\mathbf{J}}_s) + Z_L\bar{\mathbf{J}}_s \quad (2.50)$$

For a sheet with high conductivity Z_L becomes

$$Z_L = \frac{1}{\sigma t} \quad (2.51)$$

$$Z_L = \frac{\eta_0}{jk(\epsilon_r - 1)t} \quad (2.52)$$

Where σ is the plate conductivity and t is the thickness of the scatterer [27].

For a dielectric with a large dielectric constant ϵ , Z_L can be written as Harrington's approximation

$$Z_L = \frac{1}{j\omega(\epsilon - \epsilon_0)t} \quad (2.53)$$

Where ϵ is the permittivity of the material, ϵ_0 is the permittivity of free space, and $\omega = 2\pi f$ for frequency f [28].

2.2.1.6 Radar Cross Section

An important secondary variable of interest for this work is the radar cross section (RCS). The RCS measures the backscattering properties of a target in the far field. An incident field approaches the target from θ_{inc}, ϕ_{inc} and is then measured at θ, ϕ . When the measured angle is not the same as the incident field, this is referred to as the bistatic RCS. When the incident and measured direction is the same, this is known as the monostatic RCS. The units of RCS are in the area (m^2 or dBm^2). They

can be interpreted as the cross-sectional area of an isotropic scatterer that would result in the same scattered power density as the actual object. Thus, a large object with a small RCS would appear to a radar system as a much smaller object. As previously noted, the RCS is not only a function of the object's size but also its geometry, material properties, angle of incidence, angle of measurement, and polarization of the incident field. This concept will be used to optimize the backscatter from our particles in future chapters [7,25].

To calculate the RCS, I start with the basic definition of the bistatic RCS

$$\sigma = \lim_{r \rightarrow \infty} 4\pi r^2 \frac{|\bar{\mathbf{E}}_S|^2}{|\bar{\mathbf{E}}_{inc}|^2} \quad (2.54)$$

In the far field, the scattered field can be approximated as

$$\bar{\mathbf{E}}_S \cong \hat{\theta} E_\theta^S + \hat{\phi} E_\phi^S \quad (2.55)$$

Only PEC scattering is considered ($\bar{\mathbf{F}} = \mathbf{0}$) and the far fields can be estimated as

$$E_\theta^S \cong -jk\eta A_\theta \quad (2.56)$$

$$E_\phi^S \cong -jk\eta A_\phi \quad (2.57)$$

In future sections, this will need to be in Cartesian coordinates. Equations 2.56-2.57 are transformed into

$$A_\theta = \cos\theta \cos\phi A_x + \cos\theta \sin\phi A_y - \sin\theta A_z \quad (2.58)$$

$$A_\phi = -\sin\phi A_x + \cos\phi A_y \quad (2.59)$$

For three-dimensional models, the value $R = |\mathbf{r} - \mathbf{r}'|$ is needed. In the far field, this can be approximated as

$$R = r - x' \sin\theta \cos\varphi - y' \sin\theta \sin\varphi - z' \cos\theta \quad (2.60)$$

The vector potential $\bar{\mathbf{A}}$ can then be approximated in the far field as

$$\bar{\mathbf{A}} = \frac{r e^{-jkr}}{4\pi r} \iiint \bar{\mathbf{J}}(x', y', z') e^{jkr(x' \sin\theta \cos\varphi + y' \sin\theta \sin\varphi + z' \cos\theta)} dx' dy' dz' \quad (2.61)$$

Combining 2.54-2.61, the RCS can be written as the scattering cross sections

$$\sigma_\theta(\theta, \varphi) = \frac{\eta^2 k^2}{4\pi} \left| \iiint (J_x \cos\theta \cos\varphi + J_y \cos\theta \sin\varphi - J_z \sin\theta) e^{jkr(x' \sin\theta \cos\varphi + y' \sin\theta \sin\varphi + z' \cos\theta)} dx' dy' dz' \right| \quad (2.62)$$

$$\sigma_\varphi(\theta, \varphi) = \frac{\eta^2 k^2}{4\pi} \left| \iiint (-J_x \sin\varphi + J_y \cos\varphi) e^{jkr(x' \sin\theta \cos\varphi + y' \sin\theta \sin\varphi + z' \cos\theta)} dx' dy' dz' \right| \quad (2.63)$$

where σ_θ is the RCS from E_θ^s and σ_φ is from E_φ^s . The oncoming incident field has polarization as well. The total scattering cross section σ can be represented by a scattering matrix defined by the polarization of the incident field and the polarization of the scattering field defined as

$$\sigma(\theta, \varphi) = \begin{bmatrix} \sigma_{\theta\theta}(\theta, \varphi) & \sigma_{\theta\phi}(\theta, \varphi) \\ \sigma_{\varphi\theta}(\theta, \varphi) & \sigma_{\varphi\phi}(\theta, \varphi) \end{bmatrix} \quad (2.64)$$

where $\sigma_{\theta\theta}$ is the a $\hat{\theta}$ polarized incident field scattered in the $\hat{\theta}$ and $\sigma_{\theta\phi}$ is the a $\hat{\theta}$ polarized incident field scattered in the $\hat{\phi}$. Likewise, $\sigma_{\phi\phi}$ is the a $\hat{\phi}$ polarized incident field scattered in the $\hat{\phi}$ and $\sigma_{\phi\theta}$ is the a $\hat{\phi}$ polarized incident field scattered in the $\hat{\theta}$ direction. This fully characterizes the back scattering cross sections for co-polarized and cross-polarized waves [25].

2.2.1.7 Extinction

When a traveling wave is incident upon some particle, its energy is either scattered or absorbed. The total scattering of the system can be equivalently represented as the incident field scattering an area C_{scat} . Likewise, the total internal absorption of the particle can be written as the incident field being absorbed by an area C_{abs} . The total energy removed from the original wave is defined as the area C_{ext} , the total extinction cross-section. By the Law of conservation of energy, this can be written as the sum

$$C_{ext} = C_{abs} + C_{scat} \quad (2.65)$$

The actual meaning of C_{ext} is perhaps better explained with an example. Consider light approaching a telescope. The telescope has some area where it can capture the incoming light. Now particles are introduced in front of that telescope that either scatter the light or absorb it. The ability of the telescope to capture light is therefore reduced. The extinction describes this reduction as a decreased area of the telescope. This means the larger the extinction cross-section, the larger the reduction. This gives the unintuitive interpretation that to minimize the wavefront at the point of measurement (maximizing reduction), C_{ext} must be maximized. This section finds an expression of the extinction cross-section in terms of the RCS σ . Hulst's formulation is used [26]. The scattered field can be expressed as

$$u = S(\theta, \varphi) \frac{e^{-jkr+j\omega t}}{jkr} \quad (2.66)$$

$S(\theta, \phi)$ can be seen as a complex amplitude function that gives both amplitude and phase of a scattered scalar wave denoted by u . Since S is a complex amplitude function it can be written in the form

$$S(\theta, \varphi) = s(\theta, \varphi) \cdot e^{j\sigma} \quad (2.67)$$

where s is positive and σ is real. The extinction cross-section is then defined as

$$C_{ext} = \frac{4\pi}{k^2} \text{Re}\{s(0)\} \quad (2.68)$$

Equation (2.68) is the well-known optical theorem.

The extinction cross-section can also be related to the RCS derived in the previous section. Here the intensity of a scattered wave I_{scat} is written in terms of incident wave with intensity I_0 and the complex amplitude $s(\theta, \varphi)$ as

$$\bar{\mathbf{I}}_{scat} = \frac{s^2(\theta, \varphi)}{k^2 r^2} \bar{\mathbf{I}}_0 \quad (2.69)$$

The radar cross section can also be written as

$$\sigma = \lim_{r \rightarrow \infty} 4\pi r^2 \frac{|\bar{\mathbf{I}}_{scat}|}{|\bar{\mathbf{I}}_0|} \quad (2.70)$$

Combining equation 2.68-2.70, the extinction coefficient C_{ext} can be determined using the radar cross section σ in the forward scattering direction. This is written mathematically in equation 2.71.

$$C_{ext} = \sqrt{\frac{4\pi}{k^2} \text{Re}\{\sigma(0)\}} \quad (2.71)$$

2.2.2 Method of Moments

This section describes a generalized Method of Moments (MoM) problem solving an unknown linear equation [7,23-25]. This will be applied to the scatterer of interest in later chapters.

Consider a 1-D linear function in the form

$$g(x) = L(f(x)) \quad (2.72)$$

where $f(x)$ is the unknown function, $g(x)$ is the driving function (source), and L is the linear operator being applied to $f(x)$. The purpose of this method is to reconstruct $f(x)$. This is done by expanding the unknown function $f(x)$ in terms of a series of N basis functions B_n that span $f(x)$. Here the basis functions $B_n(x)$ are weighted by a set of unknown coefficients a_n .

$$f(x) = \sum_{n=1}^N a_n B_n(x) \quad (2.73)$$

This results in one equation with N unknown constants instead of an unknown continuous function. The goal is then to generate N linearly independent equations with the same set of unknown constants which can then be solved. To generate the N equations needed, the linear equation is weighted using an inner product defined as

$$\langle g(x), w(x) \rangle = \int g(x)w(x)dx \quad (2.74)$$

Notice that this is also a linear operator. Linear operators can be applied in any order. By taking the inner product of the linear equation, substituting in the series expansion for $f(x)$, and changing the order of the inner product and linear operator L , we get

$$\sum_{m=1}^M \langle g(x), w_m(x) \rangle = \sum_{m=1}^M \sum_{n=1}^N a_n L\langle B_n(x), w_m(x) \rangle \quad (2.75)$$

This be written as the matrix equation

$$\bar{E} = \bar{Z} \bar{J} \quad (2.76)$$

where

$$\bar{\mathbf{E}} = \begin{bmatrix} \langle g(x), w_1(x) \rangle \\ \langle g(x), w_2(x) \rangle \\ \vdots \\ \langle g(x), w_m(x) \rangle \end{bmatrix} = \begin{bmatrix} g_1 \\ g_2 \\ \vdots \\ g_m \end{bmatrix} \quad (2.77)$$

$$\bar{\mathbf{Z}} = \begin{bmatrix} L\langle B_1(x), w_1(x) \rangle & \cdots & L\langle B_1(x), w_m(x) \rangle \\ \vdots & \ddots & \vdots \\ L\langle B_n(x), w_1(x) \rangle & \cdots & L\langle B_n(x), w_m(x) \rangle \end{bmatrix} \quad (2.78)$$

$$\bar{\mathbf{J}} = \begin{bmatrix} a_1 \\ a_2 \\ \vdots \\ a_n \end{bmatrix} \quad (2.79)$$

Here $\bar{\mathbf{J}}$ represents the vector of unknown coefficients. The system of equations given by equation 2.71 can be solved by any number of matrix equation solvers (e.g., Gaussian elimination, inverse multiplication, Conjugate Gradient FFT, etc). Lastly, the original function $f(x)$ is determined by substituting the coefficients $\bar{\mathbf{J}}$ back into equation 2.73. This can easily be expanded to a larger coordinate set (i.e., $f(x, y, z)$) by introducing basis and test functions with the new coordinate system.

2.3 Particle Cloud Model

In this section, I describe a simple model that can extend the single particle scattering properties to a distribution, or cloud, of randomly oriented particles. When looking at particles in a cloud, the average RCS of a single particle can be used, assuming that the particles are spaced far enough apart such that mutual scattering effects are not significant [29-30]. This can be extended into larger particle densities. When an incident field approaches a cloud of particles, the total scattering can be divided into coherent and incoherent scattering components. This means that the average RCS can be written as a sum of coherent RCS and incoherent RCS [31,32].

$$\bar{\sigma} = \sigma_{coh} + \sigma_{incoh} \quad (2.80)$$

The coherent term dominates in forward scattering, whereas the incoherent term dominates in the backscattered direction [32]. At all other angles, the RCS combines coherent and incoherent components. For a single particle, this is written mathematically as

$$\bar{\sigma} = \frac{1}{4\pi} \int_0^{2\pi} d\Phi \int_0^\pi \sigma(\Theta, \Phi) \sin\Theta d\Theta \quad (2.81)$$

Where $\sigma(\Theta, \Phi)$ is the complex RCS of a single particle at an orientation angle (Θ, Φ) , and $\bar{\sigma}$ is the mean RCS averaged over all orientations. The average RCS of a single particle can be written as a sum of coherent and incoherent components given by

$$\bar{\sigma} = \bar{\sigma}_{coh} + \bar{\sigma}_{incoh} \quad (2.82)$$

In this expression, the coherent and incoherent terms can be calculated from the far-field electric field distribution as given below

$$\bar{\sigma}_{coh} = 4\pi r^2 \left(|\bar{E}_\theta|^2 + |\bar{E}_\phi|^2 \right) \quad (2.83)$$

$$\bar{\sigma}_{incoh} = 4\pi r^2 \left(\overline{|E_\theta - \bar{E}_\theta|^2} + \overline{|E_\phi - \bar{E}_\phi|^2} \right) \quad (2.84)$$

Marcus [32] showed that for a cloud of particles in which mutual scattering effects can be ignored that the aggregate RCW can be given as

$$\bar{\sigma}_{cloud} = N^2 \bar{\sigma}_{coh} + N \bar{\sigma}_{incoh} \quad (2.82)$$

where N is the total number of non-interacting within a volume. In general, the coherent component dominates for scattering in the forward direction while the incoherent term dominates in the backscattered direction. In chapter 4, I will apply this theory to compare measured results to computational predictions within a cloud of particles.

2.4 Conclusion

The necessary background for the dissertation has been given. MoM is the best full-wave solver for thin scatters like the small flakes that will be modeled in this dissertation. I derived the EFIE from first principals. This required extensive background to be given in EM. The EFIE is a continuous linear equation that is analytically unsolvable except for a few special cases. Computational methods are needed. MoM can be used to discretize linear equations like the EFIE. The section concludes with the addition of material properties. The EFIE assumes PEC boundaries for computational ease. However, PEC does not exist in the real world. Adding a linear loss term will allow material effects to be studied.

Chapter 3

MODELING A METAL PATTERNED FLAKE

The computational design algorithm developed and used throughout this dissertation is fully described in this chapter. An overview of the procedure is given in section 3.1. This general model will be applied throughout the thesis, with various cost functions defined in future chapters to explore scattering optimization.

Section 3.2 derives the necessary equations to define the starting geometric model (i.e., MoM applied to a flat perfectly conducting plate). The shape of the full plate can then be modified by removing elements from the impedance matrix. The incident fields used to excite the system can then be defined with a linear matrix equation to solve for the current coefficients. This equation can be modified with a linear term to introduce material properties such as impedance. Scattering parameters (e.g., RCS and extinction coefficients) are defined in terms of the current coefficients.

Section 3.3 describes how the full plate solution can be modified, so new shapes can be attempted without regenerating the full EFIE for each new shape. This is the basis of how shape synthesis can occur with great computational efficiency. Section 3.4 provides numerical validation of the custom code for PEC plate and one patterned surface using the commercial software package FEKO.

3.1 Overview of the Shape Synthesis Concept for Particle Scattering

The basic concept of shape synthesis is to use physics-based models to optimize an object's geometrical shape or material properties to accomplish some

particular task while maximizing (or minimizing) a given objective function. For instance, this concept has been employed by mechanical or structural engineers to synthesize the shape of a bridge that can handle a structural load while minimizing weight. While commonly employed for these types of applications shape synthesis has been less used in electromagnetic applications. Some examples include the design of an antenna shape to radiate in a desired direction [8-22]. In this research, I employed shape synthesis to design particles with desired metallic geometries to maximize the scattering of electromagnetic waves.

Figure 3.1 shows the basic particle architecture. Here, a square 2D flake of size W , on a side is broken into an array (N_x by N_y) of smaller square pixels. It is assumed that each pixel can either be metal or non-metal. The optimized design aims to determine an optimal pattern for a given set of operational conditions. It should be noted that a brute-force approach to this problem would be, in general, an intractable computational problem. The number of pattern combinations is given by $2^{N_x N_y}$, which can be a very large number even for a small number of metallic regions. Thus, an efficient algorithm is needed that solves two main issues. First, it is imperative to develop a very efficient electromagnetic analysis code that can be used to predict the EM scattering from each test pattern in a short amount of time. Second, the efficient analysis code must be integrated into an efficient iterative algorithm that intelligently uses modern optimization methods to search through the vast solution space

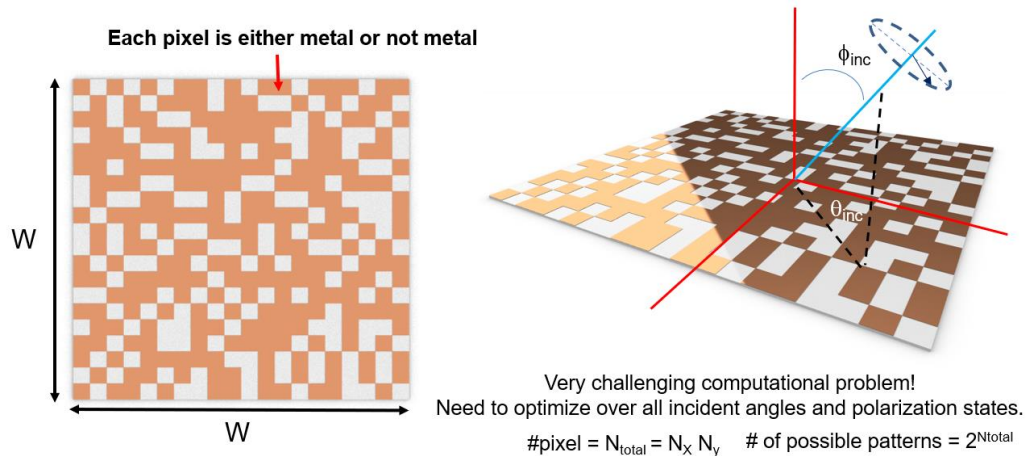


Figure 3.1: Illustration of square flakes with patterned metal. The metallic pattern is designed to maximize scattering over a band of frequencies over all incident angles and polarization states.

To address the first challenge, I developed a predictive code based on the Method of Moments (MoM). MoM, as mentioned previously, is a well-established methodology for solving EM scattering problems based on rigorous integral equations. The main computational burden of MoM is computing a large coupling matrix that is needed to predict the local effect of each pixel on itself and every other pixel. Calculating this matrix can be quite expensive in terms of computer time and resources. A second computational bottleneck is solving a large system of equations, or matrix inversion, for the unknown current distribution on the flakes. As described later in this chapter, I have developed custom MoM code that significantly reduced the computational burden from hours to seconds for this particular application.

This custom MoM code was then integrated within an iterative optimization algorithm illustrated in Figure 3.2. Here the MoM code was used as the forward model to compute the desired scattering properties (e.g., RCS or C_{ext}) over a range of

operational conditions (e.g., frequencies, incident angles and polarization states). The results were then inputted to an optimization algorithm (e.g., genetic algorithms, particle swarm optimization, etc. ...), which intelligently varied the pattern and repeated this process until a solution is achieved.

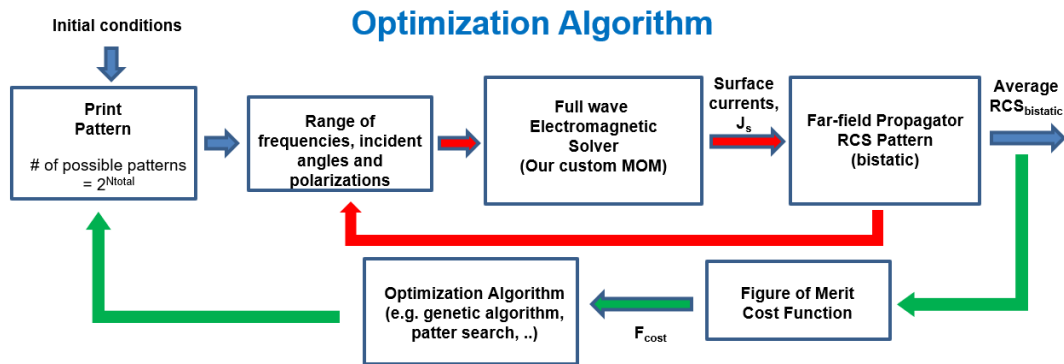


Figure 3.2: Illustration of optimization algorithm which iteratively tests printed patterns until an optimal design is reached.

In the next few sections, I describe the details of the customized MoM code, including the methods developed to improve the computational efficiency and the optimization algorithm that was integrated into the overall code and tested.

3.2 Method of Moments Applied to a Patterned Flake

This section describes the specific MoM implementation used for this research. This method employs Peterson's formulation to describe scattering from a flat, perfectly conducting plate [25]. Consider the geometry illustrated in Figure 3.3. Here an electrically thin square plate, at $z=0$, is broken into a grid of squares called pixels. Each pixel can be either composed of a PEC or free space. The pixel is further

discretized into a grid of smaller cells of size a . Each MoM basis function is assigned to this smallest length scale which is also assumed to be much smaller than the operational wavelength (i.e., $a \ll \lambda$). This rectangular grid easily enables polarizations to be broken into \hat{x} and \hat{y} when applying the EFIE. This approach also allows the grid to be pixelated for shape synthesis. Thus, by removing a pixel, the shape of the plate will be changed. The predictive model must also ensure that the current across each pixel is not constant.

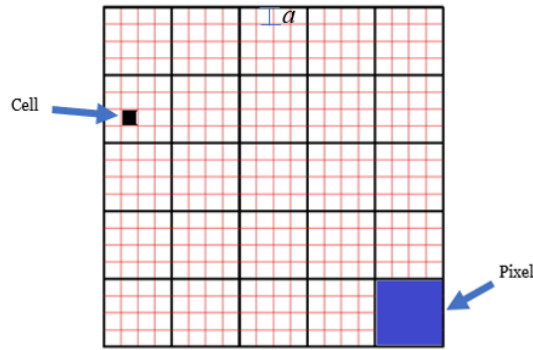


Figure 3.3: Meshing of the square plate

3.2.1 Method of Moments Applied to a PEC Plate

In this section, I will describe the MoM method applied to the geometry and grid shown in Figure 3.3. Since the plate is placed at $z = 0$ the auxiliary vector potential $\bar{\mathbf{A}}$ is reduced to the 2-D form

$$\bar{\mathbf{A}} = \iint [\hat{x}J_x(x', y') + \hat{y}J_y(x', y')] \frac{e^{-jkR}}{4\pi R} dx' dy' \quad (3.1)$$

$$R = \sqrt{(x - x')^2 + (y - y')^2} \quad (3.2)$$

Using the mesh shown above, the EFIE for a PEC from equation 2.48 can be rewritten as

$$\bar{\mathbf{E}}_x^{inc} = -\hat{x} \cdot \frac{\nabla \nabla \cdot \bar{\mathbf{A}} + k^2 \bar{\mathbf{A}}}{j\omega\epsilon_0} \quad (3.3)$$

$$\bar{\mathbf{E}}_y^{inc} = -\hat{y} \cdot \frac{\nabla \nabla \cdot \bar{\mathbf{A}} + k^2 \bar{\mathbf{A}}}{j\omega\epsilon_0} \quad (3.4)$$

Following the procedure outlined in section 2.2.2, the current is expanded into a series representation using the well-known “roof-top” basis functions defined in equations 3.7-3.8. These functions are centered on the edge between two cells at the point (x_n, y_n) . It is a triangle in the direction of current flow and a pulse in the orthogonal direction, modeling current flowing from one cell into the next.

$$J_x(x, y) = \sum_{n=1}^M j_{xn} B_{xn}(x, y) \quad (3.5)$$

$$J_y(x, y) = \sum_{n=1+M}^N j_{yn} B_{yn}(x, y) \quad (3.6)$$

$$B_{xn}(x, y) = t(x; x_n - a, x_n, x_n + a) p(y; y_n - a, y_n, y_n + a) \quad (3.7)$$

$$B_{yn}(x, y) = t(y; y_n - a, y_n, y_n + a) p(x; x_n - a, x_n, x_n + a) \quad (3.8)$$

$$p(x; x_1, x_2) = \begin{cases} 1, & x_1 < x < x_2 \\ 0, & \text{else} \end{cases} \quad (3.9)$$

$$t(x; x_3, x_4, x_5) = \begin{cases} \frac{x-x_3}{x_4-x_3}, & x_3 < x < x_4 \\ \frac{x_5-x}{x_5-x_4}, & x_4 < x < x_5 \end{cases} \quad (3.10)$$

This is a rather long and semi-complicated function that can be hard to understand without plotting. The roof-top function of 3.7-3.8 is therefore illustrated in figure 3.4.

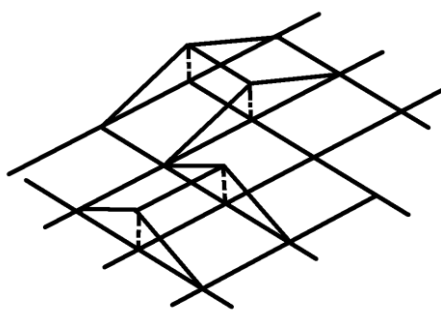


Figure 3.4: Roof-top basis function

The location of the center points, therefore, depends on whether the current is \hat{x} or \hat{y} polarized. This is shown in Figure 3.5, where the red horizontal arrows define the center point of B_{xn} while the blue vertical arrows define the center points of B_{yn} .

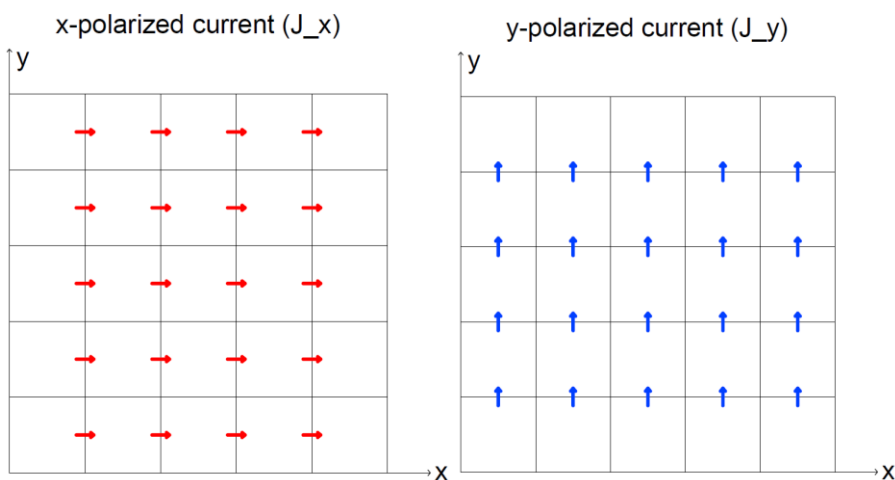


Figure 3.5: Defining (x_m, y_n) for B_{xn} (right) and B_{yn} (left)

The current expansion functions are tested with the “razor blade” functions to create the N linear equations necessary to solve for the N unknowns. The razor blade function is defined as

$$T_{xm}(x, y) = p \left(x; x_m - \frac{1}{2}a, x_m, x_m + \frac{1}{2}a \right) \delta(y - y_m) \quad (3.11)$$

$$T_{ym}(x, y) = p \left(x; y_m - \frac{1}{2}a, y_m, y_m + \frac{1}{2}a \right) \delta(x - x_m) \quad (3.12)$$

This is illustrated in Figure 3.6

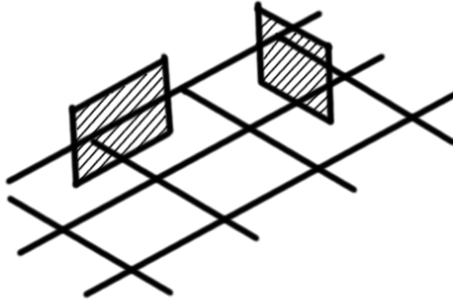


Figure 3.6: Razor-blade function

Following the MoM approach from section 2.2.2 and applying the above testing and basis function, the matrix equation given in equation 3.13 is formed

$$\begin{bmatrix} \mathbf{A} & \mathbf{B} \\ \mathbf{C} & \mathbf{D} \end{bmatrix} \begin{bmatrix} \mathbf{j}_x \\ \mathbf{j}_y \end{bmatrix} = \begin{bmatrix} \mathbf{e}_x \\ \mathbf{e}_y \end{bmatrix} \quad (3.13)$$

One approach is to compute the four integrals directly. The basis function needs to be integrated in x and y as well as the testing functions. A less computationally intensive approach exploits even symmetry. The integrals can be rewritten as a 2-D convolution:

$$\mathbf{A} = -\frac{1}{j\omega\epsilon_0} T_{xm} * \left(\frac{\partial^2}{\partial x^2} + k^2 \right) (B_{xn} * G) \quad (3.14)$$

$$\mathbf{B} = -\frac{1}{j\omega\epsilon_0} T_{xm} * \left(\frac{\partial^2}{\partial x \partial y} \right) (B_{yn} * G) \quad (3.15)$$

$$\mathbf{C} = -\frac{1}{j\omega\epsilon_0} T_{ym} * \left(\frac{\partial^2}{\partial x \partial y} \right) (B_{xn} * G) \quad (3.16)$$

$$\mathbf{D} = -\frac{1}{j\omega\epsilon_0} T_{ym} * \left(\frac{\partial^2}{\partial y^2} + k^2 \right) (B_{yn} * G) \quad (3.17)$$

Where G is the 2D free-space Green's function given by

$$G(x, y) = \frac{e^{-jk\sqrt{x^2+y^2}}}{4\pi\sqrt{x^2+y^2}} \quad (3.18)$$

and the convolution is defined as

$$U * V = \iint U(x', y') V(x - x', y - y') dx' dy' \quad (3.19)$$

that is evaluated at $x=y=0$. Every operator in equations 3.14-3.17 is linear, and the order can be rearranged. After reordering the operations, the following results

$$\mathbf{A} = -\frac{1}{j\omega\epsilon_0} \left[\frac{\partial^2}{\partial x^2} + k^2 (T_{xm} * B_{xn}) \right] * G \quad (3.20)$$

$$\mathbf{B} = -\frac{1}{j\omega\epsilon_0} \left[\left(\frac{\partial^2}{\partial x \partial y} \right) (T_{xm} * B_{yn}) \right] * G \quad (3.21)$$

$$\mathbf{C} = -\frac{1}{j\omega\epsilon_0} \left[\left(\frac{\partial^2}{\partial x \partial y} \right) (T_{ym} * B_{xn}) \right] * G \quad (3.22)$$

$$\mathbf{D} = -\frac{1}{j\omega\epsilon_0} \left[\frac{\partial^2}{\partial y^2} + k^2 (T_{ym} * B_{yn}) \right] * G \quad (3.23)$$

The expression in the bracket can be solved analytically, reducing computer computation requirements. $T * B$ reduces to

$$(T_{xm} * B_{xn}) = aq \left(x; x_m - x_n - \frac{3}{2}a, x_m - x_n + \frac{3}{2}a \right) p \left(y; y_m - y_n - \frac{1}{2}a, y_m - y_n + \frac{1}{2}a \right) \quad (3.24)$$

$$(T_{xm} * B_{yn}) = at(x; x_m - x_n - a, x_m - x_n, x_m - x_n + a) t(y; y_m - y_n - a, y_m - y_n, y_m - y_n + a) \quad (3.25)$$

$$(T_{ym} * B_{xn}) = at(x; x_m - x_n - a, x_m - x_n, x_m - x_n + a) t(y; y_m - y_n - a, y_m - y_n, y_m - y_n + a) \quad (3.26)$$

$$(T_{ym} * B_{yn}) = ap \left(x; x_m - x_n - \frac{1}{2}a, x_m - x_n + \frac{1}{2}a \right) q \left(y; y_m - y_n - \frac{3}{2}a, y_m - y_n + \frac{3}{2}a \right) \quad (3.27)$$

where $q \left(x; -\frac{3a}{2}, \frac{3a}{2} \right)$ is the spline function defined as

$$q \left(x; -\frac{3a}{2}, \frac{3a}{2} \right) = \begin{cases} 0, & x < -\frac{3a}{2} \\ \frac{9}{8} + \frac{3x}{2a} + \frac{x^2}{2a^2}, & -\frac{3a}{2} < x < -\frac{a}{2} \\ \frac{3}{4} - \frac{x^2}{a^2}, & -\frac{a}{2} < x < \frac{a}{2} \\ \frac{9}{8} - \frac{3x}{2a} + \frac{x^2}{2a^2}, & \frac{a}{2} < x < \frac{3a}{2} \\ 0, & x > \frac{3a}{2} \end{cases} \quad (3.28)$$

Applying the operators on the left hand side of the bracket in equation 2.20-

2.23 to $T * B$ gives

$$\left(\frac{\partial^2}{\partial x^2} + k^2 \right) (T_{xm} * B_{xn}) = \frac{1}{a} p \left(x; -\frac{3a}{2}, -\frac{a}{2} \right) - \frac{2}{a} p \left(x; -\frac{a}{2}, \frac{a}{2} \right) + \frac{1}{a} p \left(x; \frac{a}{2}, \frac{3a}{2} \right) + k^2 a q \left(x; -\frac{3a}{2}, \frac{3a}{2} \right) \Big|_{x=x-x_m+x_n} p \left(y; y_m - y_n - \frac{a}{2}, y_m - y_n + \frac{a}{2} \right) \quad (3.29)$$

$$\left(\frac{\partial^2}{\partial x \partial y} \right) (T_{xm} * B_{yn}) = \quad (3.30)$$

$$\frac{1}{a} \{ p(x; -a, 0) p(y; -a, 0) - p(x; -a, 0) p(y; 0, a) - p(x; 0, a) p(y, -b, 0) p(x; 0, a) p(y, 0, b) \}_{x=x-x_m+x_n, y=y-y_m+y_n}$$

$$\left(\frac{\partial^2}{\partial x \partial y}\right)(T_{ym} * B_{xn}) \quad (3.31)$$

$$= \frac{1}{a} \{p(x; -a, 0)p(y; -a, 0) - p(x; -a, 0)p(y; 0, a) - p(x; 0, a)p(y, -b, 0)p(x; 0, a)p(y, 0, b)\}_{x=x-x_m+x_n, y=y-y_m+y_n}$$

$$\left(\frac{\partial^2}{\partial y^2} + k^2\right)(T_{ym} * B_{yn}) = \quad (3.32)$$

$$\frac{1}{a} p\left(y; -\frac{3a}{2}, -\frac{a}{2}\right) - \frac{2}{a} p\left(y; -\frac{a}{2}, \frac{a}{2}\right) + \frac{1}{a} p\left(y; \frac{a}{2}, \frac{3a}{2}\right) +$$

$$+ k^2 a q \left(y; -\frac{3a}{2}, \frac{3a}{2}\right) \Big|_{y=y-y_m+y_n} p\left(x; x_m - x_n - \frac{a}{2}, x_m - x_n + \frac{a}{2}\right)$$

Equations 3.29-3.32 need to be convoluted with Green's function given in equation 3.18. This is done at $x = y = 0$, so the convolution definition in equation 3.19 is reduced to

$$U * V = \iint U(x', y') V(-x', -y') dx' dy' \quad (3.33)$$

This calculation must be done computationally. Note this is only a 2D integration thus four integrals have successfully been reduced to only two.

3.2.2 Polarized Incident Field

In the previous section, the focus was on discretizing the current at the plate. In this section, the source is examined. The model looks at scattering in the far field, so an incoming plane wave is chosen as the source with polarization:

$$E_{\theta}^{inc} = \hat{\theta} E_{\theta}^{inc} + \hat{\phi} E_{\phi}^{inc} \quad (3.34)$$

$$E_{\theta}^{inc} = E_0 e^{jk(x \sin \theta_{in} \cos \phi_{in} + y \sin \theta_{in} \sin \phi_{in})} \quad (3.35)$$

$$E_{\phi}^{inc} = E_0 e^{jk(x \sin \theta_{in} \cos \phi_{in} + y \sin \theta_{in} \sin \phi_{in})} \quad (3.36)$$

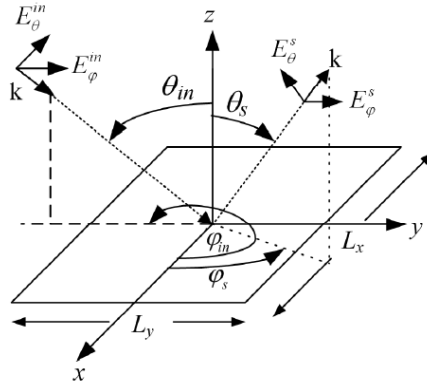


Figure 3.7 Incident and scattered wave polarization [33]

However, at the plate, the source must be described in terms of \hat{x} and \hat{y} to match the meshing defined in section 3.1.1. This can be calculated by taking the dot product:

$$E_x^{inc} = (\hat{\theta} \cdot \hat{x})E_{\theta}^{inc} + (\hat{\phi} \cdot \hat{x})E_{\phi}^{inc} \quad (3.37)$$

$$E_y^{inc} = (\hat{\theta} \cdot \hat{y})E_{\theta}^{inc} + (\hat{\phi} \cdot \hat{y})E_{\phi}^{inc} \quad (3.38)$$

Which becomes

$$E_x^{inc} = E_0(\cos\theta_{in}\cos\phi_{in} - \sin\phi_{in})e^{jk(x\sin\theta_{in}\cos\phi_{in}+y\sin\theta_{in}\sin\phi_{in})} \quad (3.39)$$

$$E_y^{inc} = E_0(\cos\theta_{in}\sin\phi_{in} + \cos\phi_{in})e^{jk(x\sin\theta_{in}\cos\phi_{in}+y\sin\theta_{in}\sin\phi_{in})} \quad (3.40)$$

This is discretized by integrating against the razor-blade testing function equation 3.7-3.8 to get

$$e_{xm} = \int_{x_m - \frac{a}{2}}^{x_m + \frac{a}{2}} E_x^{inc}(x, y_m) dx \quad (3.41)$$

$$e_{ym} = \int_{y_m - \frac{a}{2}}^{y_m + \frac{a}{2}} E_x^{inc}(x_m, y) dy \quad (3.42)$$

The Method of Moments has now been fully applied and the EFIE has been discretized in the form of equation 2.76-2.79. In a typical MoM, this would be solved using mathematical tricks (CGFFT) in trying to speed calculations. However, for optimization, I instead will calculate the inverse of $\begin{bmatrix} \mathbf{A} & \mathbf{B} \\ \mathbf{C} & \mathbf{D} \end{bmatrix}$. Now, the current can be resolved for multiple incoming waves as one might when calculating average scattering values.

3.2.3 Scattering Parameters

In this section, the scattering parameters for a PEC plate is provided. The backscattering coefficients were derived in section 2.2.1.6 in equation 2.64. The basis functions of the expanded currents in equations 3.5-3.10 are substituted into equation 2.64 and the bistatic radar cross section becomes

$$\sigma(\theta, \varphi) = \frac{\eta^2 k^2}{4\pi} \left| \sum_{n=1}^M j_{xn} \cos\varphi \cos\theta \Psi(\theta, \varphi) + \sum_{n=M+1}^N j_{yn} \sin\varphi \cos\theta \Psi(\theta, \varphi) \right|^2 + \frac{\eta^2 k^2}{4\pi} \left| \sum_{n=1}^M -j_{xn} \sin\varphi \Psi(\theta, \varphi) + \sum_{n=M+1}^N j_{yn} \cos\varphi \Psi(\theta, \varphi) \right|^2 \quad (3.24)$$

where

$$\Psi(\theta, \varphi) = a^2 e^{jksin\theta(x_n \cos\varphi + y_n \sin\varphi)} \quad (3.25)$$

The monostatic RCS is found when the observation angle is the same as the incident scattering angle. The extinction coefficient can be found by substituting equation 3.24 into equation 2.71.

3.3 Efficient Impedance Matrix Formulation

The MoM algorithm described in the previous sections is based on a well-established method for solving scattering problems. The computational complexity of a solution for any given test pattern is largely dependent on the time and memory

required to; (1) compute the components of the impedance matrix using equations 3.20-3.23 and (2) solve the resulting system of linear equations, (equation 3.13) for the unknown surface current coefficients. Computing the impedance matrix can be particularly time and memory-intensive given that it requires evaluating a double numerical integral for each component of a $2N \times 2N$ matrix where N is the number of basis functions. For even moderately electrically large problems filling the impedance matrix can take many hours. Moreover, if this process is repeated for each test pattern in an iterative optimization algorithm, such as the one described in Figure 3.2, the total time to the solution would be impractical. Thus, it is necessary to explore novel approaches to reduce the problem's computational complexity.

As illustrated in Figure 3.8, each component of the impedance matrix, Z_{ij} , is proportional to the coupling of the surface current at location i to a surface current at location j . If the flake is fully metalized (i.e., no patterns), then the entire Z matrix will be full (i.e., no zero components). However, for a patterned flake in which some areas are non-metalized, the Z matrix components will be zero for those particular rows and columns. I exploited this concept to significantly reduce the computational complexity of a design problem. For a flake of a fixed electrical size that is discretized to a given number of pixels, I precompute the entire impedance matrix assuming the flake is fully metalized.

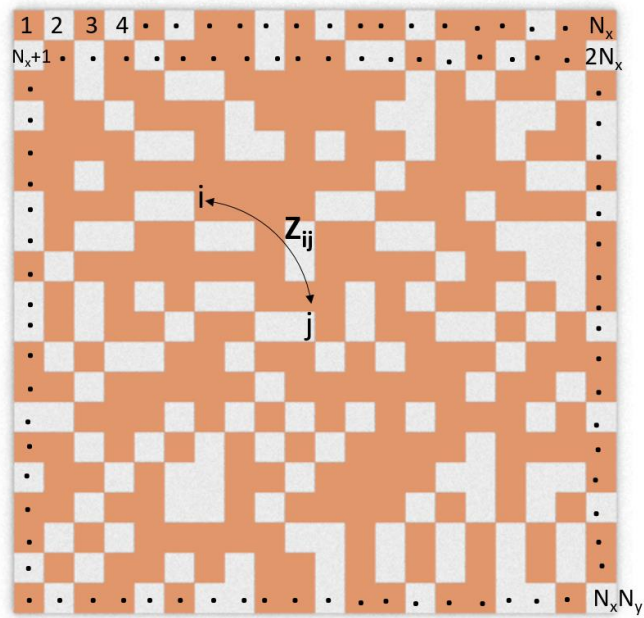


Figure 3.8 Illustration of the coupling, Z_{ij} , within the impedance matrix.

This computation can take over 12 hours to complete. However, once it is determined, I can store the matrix in memory and use it for any arbitrary pattern of the same size flake. Specifically, the impedance matrix is modified by having the plate pixels be on (metal) or off (hole). This is done by removing elements from the precomputed impedance matrix. First, consider a single cell. Each cell is surrounded by four edges corresponding to rows and columns in the impedance matrix. The algorithm removes a cell by locating the corresponding edges and removing them from the impedance matrix. An example is shown below.

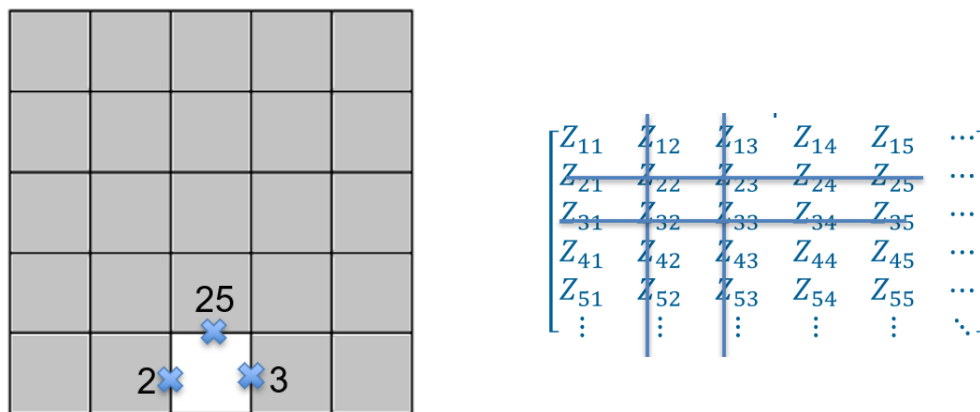


Figure 3.9: Removing cells from the impedance matrix

A problem arises with this model if two pixels' corners are touching (an example is shown in figure 3.10). When defining the meshing, the current is only allowed to flow in x and y. Current flowing across the touching corners cannot be modeled. However, high current flow is expected. Other groups have found that not modeling the touching corners leads to a frequency shift in the final design [20]. They chose to post-process and remove the touching corners after fabrication. For small particles, this is not a viable option. Instead, the computational model is adapted. Cells have already been grouped into pixels to allow for current variations across a single pixel. A single cell is left on (metal) when two pixel corners are touching. This will allow current flow across the touching corners. This fix is shown in figure 3.9. Blue represents a pixel being off (free space), while yellow is where metal is placed.

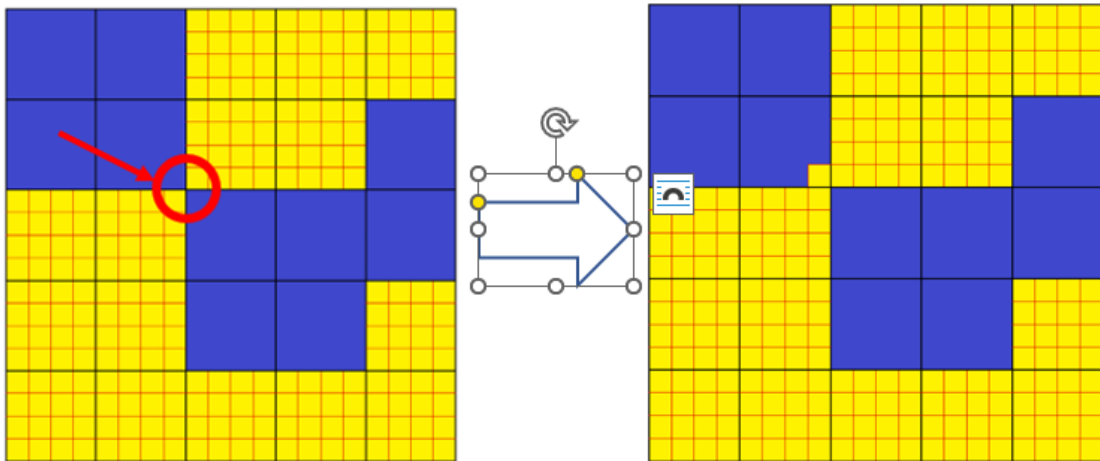


Figure 3.10: Corner fix

Other time-saving methods were also employed to reduce solution time for any given test pattern. For example, I assumed symmetric patterns such as the mirror symmetry shown below for some applications.

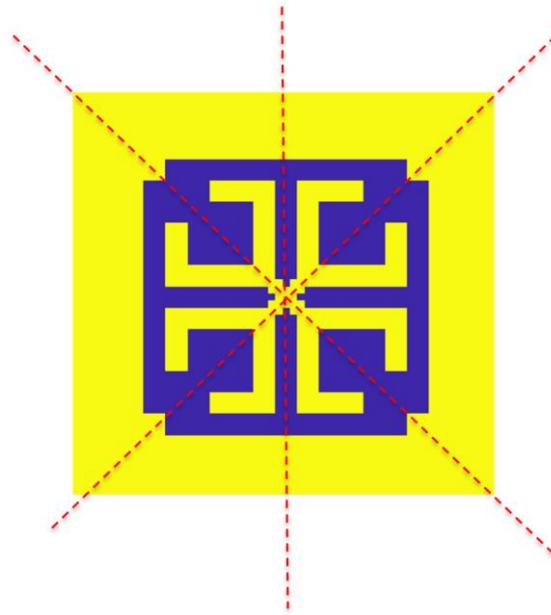


Figure 3.11 Enforcing symmetric patterns reduced the computational time for the design algorithms.

These modifications to the standard MoM algorithm significantly affected the total computation time. As an illustrative example, consider a plate composed of 44 x 44 pixels. This results in an impedance matrix that is 3872 x 3872 in size. Listed in Table 3.1 are the computation times for the various steps in the MoM calculation using a high end PC. By a significant amount filling the impedance matrix takes the most time per solution. This even includes all the shortcuts such as symmetry. Thus if the entire process was repeated for each test pattern in the iterative solver, the total optimization time would be over 11 days assuming a particle swarm optimization of 100 different patterns per generation and 21 generations until convergence. It should be noted that this is only for a single frequency. The time to solution would increase linearly with the number of frequency points. However, by storing the full impedance matrix and using the algorithm given above to modify it per iteration the total time for

convergence was less than 15 minutes. *This amounts to a decrease in computation time of over three orders of magnitude.*

Table 3.1: Timing for solving matrix equations

MoM Solution	Time
Generate impedance Matrix (MATLAB)	19.2 minutes
Generate right hand side (i.e., incident field)	0.01 seconds
Solve system of equations for surface currents	0.4 seconds
Calculate RCS from surface currents	0.0014 seconds

3.4 Model Validation

To numerically validate the custom MoM code, I performed several computational experiments.

3.4.1 Fully Metallized Square Plate

As a first test, a fully metallized PEC plate was validated by comparing my results to a commercial code (FEKO). For this comparison, I computed the average monostatic RCS of the metal plate illuminated by a plane wave with incident angles varying in elevation $\theta = [0, \frac{\pi}{2}]$ and azimuth $\varphi = [0, \frac{\pi}{4}]$ at both TE ($\hat{\theta}$) and TM ($\hat{\phi}$) polarizations. This calculation was repeated for square plates of side length, L, varied from $[0.1\lambda, 0.5\lambda]$. The percent difference between my results and FEKO was found to be 0.047% on average. The percent difference at each length is listed in the table below and plotted in figure 3.12.

Table 3.2: Percent difference between custom code and FEKO

Plate Length (λ)	Percent Dif (%)
0.1	0.1564
0.15	0.0830
0.2	0.0410
0.25	0.0200
0.3	0.0150
0.4	0.0039
0.5	0.0094

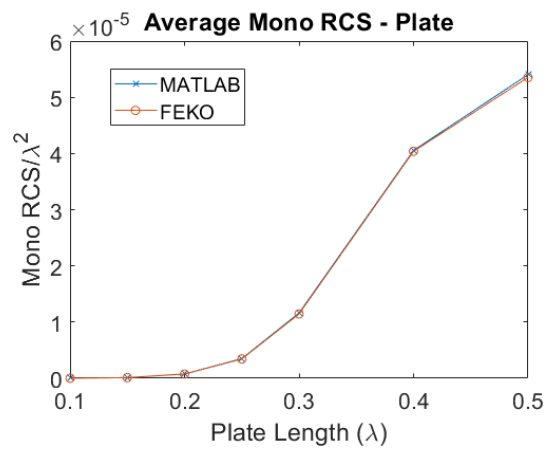


Figure 3.12: Plate average monostatic RCS (MATLAB vs FEKO)

A single plate with side length 0.3λ is then taken. A single slice of the monostatic RCS at $\varphi = 0$ is found for $\sigma_{\theta\theta}$ and plotted in figure 3.13.

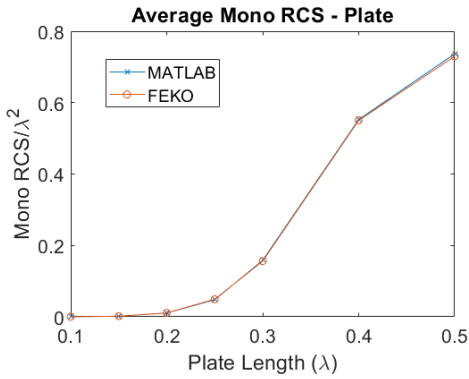


Figure 3.13: Average monostatic RCS at $\varphi = 0$ of full 0.3λ plate

3.4.2 Patterned Square Plate

Next, consider the pattern shown in figure 3.14 with a side length 0.3λ . It has 11 by 11 pixels, and each pixel contains 4 by 4 cells.

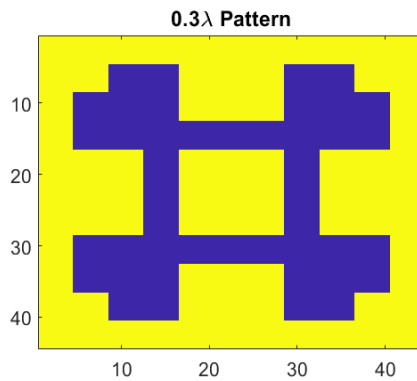


Figure 3.14: Patterned plate with side length of 0.3λ

The monostatic RCS for $\sigma_{\theta\theta}$ was calculated using incident angles $\theta = [0, \frac{\pi}{2}]$ and $\varphi = [0, \frac{\pi}{2}]$ both with 26 points used and plotted in figure 3.15.

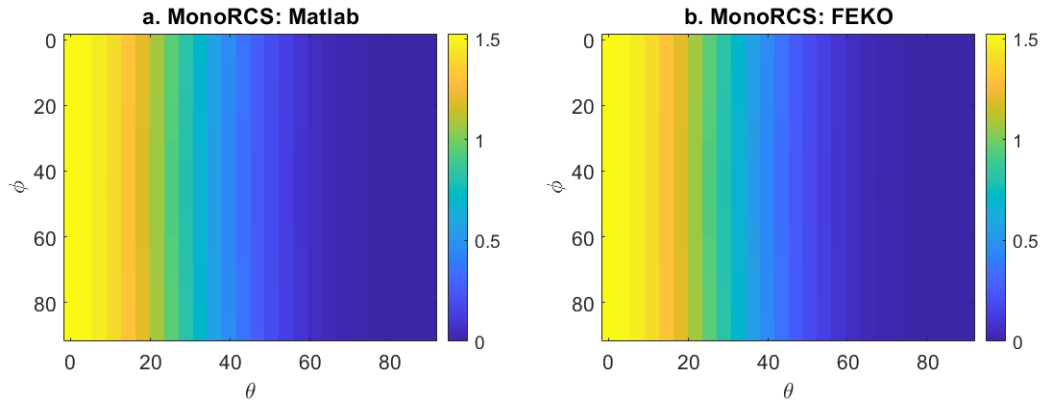


Figure 3.15: Average monostatic RCS (σ/λ^2) plotted in a. MATLAB and b. FEKO of pattern 0.3λ plate

A slice at $\phi = 0$ is taken and plotted in figure 3.16. The average percent difference of all angles calculated was $1.8822 * 10^{-3}$.

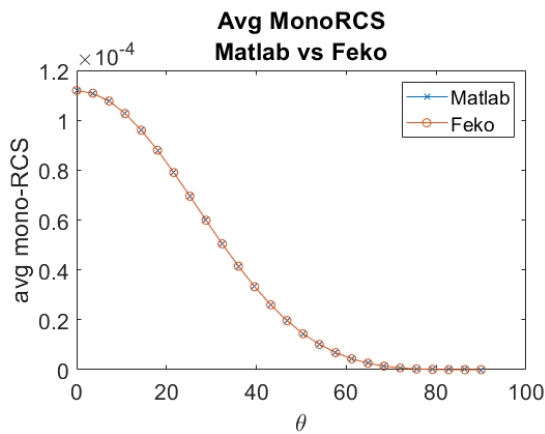


Figure 3.16: Average monostatic RCS at $\phi = 0$ of pattern 0.3λ plate

3.5 Overview of Optimization Procedure

The flowchart shown in figure 3.17 illustrates the algorithm applied to various scattering conditions. It begins by supplying the necessary parameters such as frequency, incident angles, length of the plate, and material impedance (if applicable). A square plate will be used as the starting geometry. It is meshed using rectangular cells rather than the normal triangular ones in anticipation of creating a grid. The EFIE is solved using the defined mesh for the impedance.

This thesis implements the code in MATLAB and optimizes using the built-in optimization toolbox. The pixelated grid is a non-continuous non-linear integer optimization, so MATLAB's toolbox supplies three options: pattern search, genetic algorithm, and particle swarm. The trade-offs of these options are discussed in section 3.5. Once the algorithm has been chosen, they all begin the same way. A new geometry is made from a full plate by removing pixels. Geometry repair fixes a known problem when two corners touch. Finally, an optimizer (particle swarm, genetic algorithm, pattern search) evaluates a cost function that optimizes the chosen scattering parameters. Once the optimizer's exit conditions are met, a final optimized design is outputted to the user.

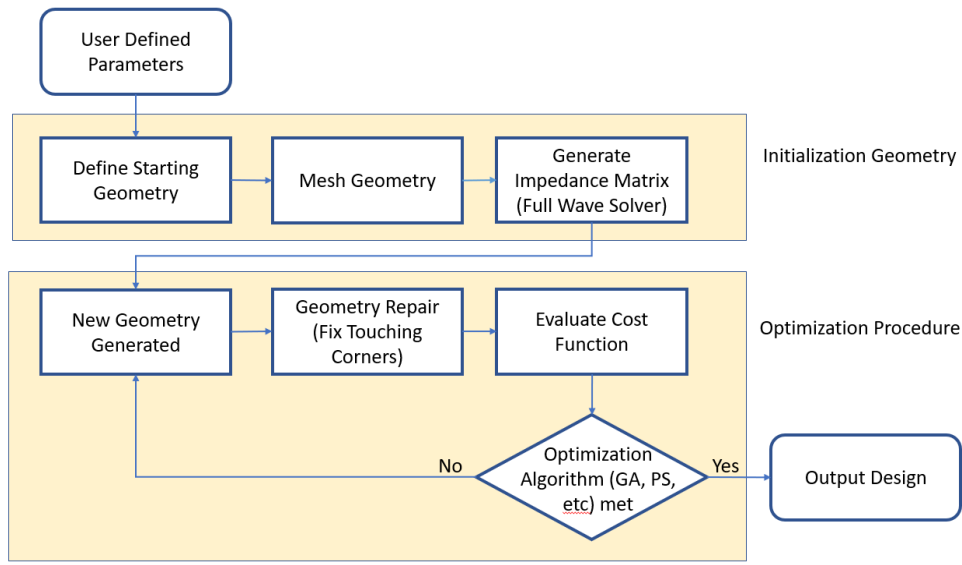


Figure 3.17: Flow diagram describing the optimization algorithm used.

3.5.1 Optimizers

This section will review the three optimizers in MATLAB’s built-in toolbox that can be used for this problem. In future chapters, different cost functions will be examined to optimize different scattering parameters, but the core of the problem is always the same. Pixels are removed from the plate, and the scattering parameter of interest is found. The code knows what pixels to remove with an array of ones and zeros, where one means a metal pixel is kept, while zero means the pixel is removed. The array will be optimized with the chosen optimization algorithm. This is a non-differentiable integer problem that restricts the optimizer. The choices are pattern search, genetic algorithm, and particle swarm. A discussion of each will be given in the following sections describing how they work and their trade-offs. Each of these algorithms seeks a minimum, so the cost function fed into each must be written to reflect this.

3.5.1.1 Pattern Search

Pattern search is different from the other two optimizers in that it only has one initial guess, which the user specifies. After the initial guess is made, pattern search will evaluate a nearby point. As soon as a lower value is found, the algorithm moves to that point and then repeats. Nearby points are assessed, and the algorithm moves to the first point found to be less than the current point. The optimizer will exit once no nearby points are less than the current point.

This offers many benefits. An initial guess of no pixels being placed can be made. The evaluated “nearby point” will always be a singular pixel then. The first few iterations of the algorithm will quickly complete because fewer pixels means the matrix is small. This also leads to the final design being the fewest possible pixels placed, which means less material when manufacturing the design. However, this downfall is that a local minimum can be found before the global minimum. If there are no nearby points less than the current point, the algorithm exits and has no way of knowing another minimum exists. In general, pattern search was only used in this thesis to conduct initial test runs. It is helpful to test new cost functions, but the final design should be found using one of the other optimizers.

3.5.1.2 Genetic Algorithm

The genetic algorithm is a stochastic algorithm that starts with a large population of random initial guesses. Random individuals from the initial population will be matched and used as “parents” to create the next generation. This new generation is referred to as the children. Inspired by natural selection, this continues with the “best” children of each generation being used to create the following generation. Eventually, the population tends towards the global minimum.

Because a large initial population is chosen, the cost function is evaluated multiple times per single iteration. This leads to the optimizer running much slower than pattern search. The trade-off is that the local minimum has a higher probability of being found due to a large population. The genetic algorithm is stochastic and does not promise the global minimum will be found. In practice, as long as a large enough initial population is chosen, the algorithm approaches the global minimum.

3.5.1.3 Particle Swarm

Like the genetic algorithm, particle swarm is a stochastic algorithm that begins with multiple initial guesses. The difference is particle swarm attempts to act like a swarm of insects moving toward a target (the local minimum). Each initial particle will evaluate the cost function and then randomly guesses a nearby solution. It reevaluates these points and notes which modifications saw the greatest improvement. All particles will then attempt to coalesce toward the area with the greatest change. This continues until a majority of particles have swarmed towards one solution as the global minimum

Because it is stochastic, like the genetic algorithm, it has the same trade-offs in theory (slower runs, but more likely to find the global minimum). Particle swarm outperformed the other methods for this study. It returned better results at faster speeds than the genetic algorithm, so it was used exclusively when generating results found throughout the thesis.

3.6 System

In the following sections, the computer used was an Intel® Core™ i7-10700k CPU with 8 cores and 128GBs of RAM. The operating system is Windows 10 and is

implemented in MATLAB. Two toolboxes were utilized, the optimization toolbox and the parallel processing toolbox.

3.7 Summary

The model has been fully developed and will be applied to a multitude of models in the latter sections. An outline of the general optimization algorithm was presented, and different optimization algorithms were examined. The necessary equations were derived for the solution of a flat PEC plate. All these parameters can be calculated computationally. Modification to the impedance matrix was shown to modify the plate geometry. This allows new patterns to be solved from the initial geometry with great computational efficiency. Calculating scattering parameters from a new pattern requires 1) removing elements from a matrix 2) matrix inverse and 3) matrix multiplication. None of these operations are computationally expensive. The model was then validated in FEKO. The chapter concludes with the optimization procedure. Particle swarm will be used exclusively from here on.

Chapter 4

COMPUTATIONAL RESULTS

The model described in chapter 3 is now implemented to explore optimizing patterns for backscattering and forward scattering. Section 4.1 focuses on maximizing the backscattering using monostatic RCS. The cross-polarized ($\sigma_{\theta\phi}$ and $\sigma_{\phi\theta}$) scattering is essentially zero, so only the co-polarized ($\sigma_{\theta\theta}$ and $\sigma_{\phi\phi}$) scattering is optimized. I assume a plate symmetry described in 4.1.1 where only 1/8th of the plate is optimized, significantly reducing the number of optimization variables. This assumption is used throughout the section to reduce optimization run times. The section begins with single-frequency optimization at different plate lengths assuming perfect conditions, PEC material, and an ideal pattern. When manufacturing the flakes, multiple designs are printed on a single sheet using materials with finite conductivity and then cut out. The ability to perfectly cut out each flake design is a difficult problem for small flakes. I update the optimization algorithm to include this error. I look at both no-registration and partial-registration designs showing that even some control over the registration error can improve results. Two multi-frequency results are attempted. One with the plate length set to half-wavelength at the center frequency. The next attempts to capitalize on high improvement seen at a plate length $L = 0.2\lambda$ with some success. Finally, the designs introduce finite conductivity to explore material effects.

Section 4.2 moves to investigate forward scattering. The algorithm minimizes the forward scattering by maximizing the extinction scattering. Again, the algorithm

only uses co-polarized scattering. The section follows a similar outline as 4.1. Single-frequency response at different plate lengths is optimized with the same high improvement seen at $L = 0.2\lambda$. The section moves to multi-frequency patterns, with one plate length set to the half-wavelength and the second attempting to use the high improvement seen at $L = 0.2\lambda$. The section concludes with material effects by introducing finite conductivity to designs.

Section 4.3 finishes the chapter by introducing the cross-polarized scattering term for the monostatic RCS. There are now two terms, the co- and cross-polarized scattering that the optimization algorithm needs to improve. Direct averaging of both terms is used. The cross-polarized term is so much smaller than the co-polarized term that direct averaging both leads to the co-polarized term dominating with minimal improvement to the cross-polarized term. Instead, improvement is tracked. The first scheme uses the average improvement of both co- and cross-polarized scattering. The algorithm finds that the cross-polarized improvement is so much larger than the co-polarized term that it dominates the average. The second attempt keeps co- and cross-polarized scattering within a ratio so that no term can dominate. No solution is found using this scheme. The algorithm has assumed a plate symmetry until this point to reduce run times. I removed this assumption which significantly increased run times, but optimized patterns were found. The results for the three different schemes are compared to each other, and the final scheme is shown to produce optimal results. Finite conductivity is added to the designs to explore its effects.

4.1 Optimization of Co-polarized Backscattering from Patterned Plates

Maximizing the backscattering using the co-polarized monostatic RCS is first explored. The cost function becomes an average of the monostatic RCS over different parameters (incident angles, frequencies, and lateral shifts) to return as much energy as possible to the source location. The cross-polarization ($\sigma_{\theta\phi}, \sigma_{\phi\theta}$) is essentially zero and does not affect the average. Only the co-polarized scattering ($\sigma_{\theta\theta}, \sigma_{\phi\phi}$) is considered in this section when taking the average.

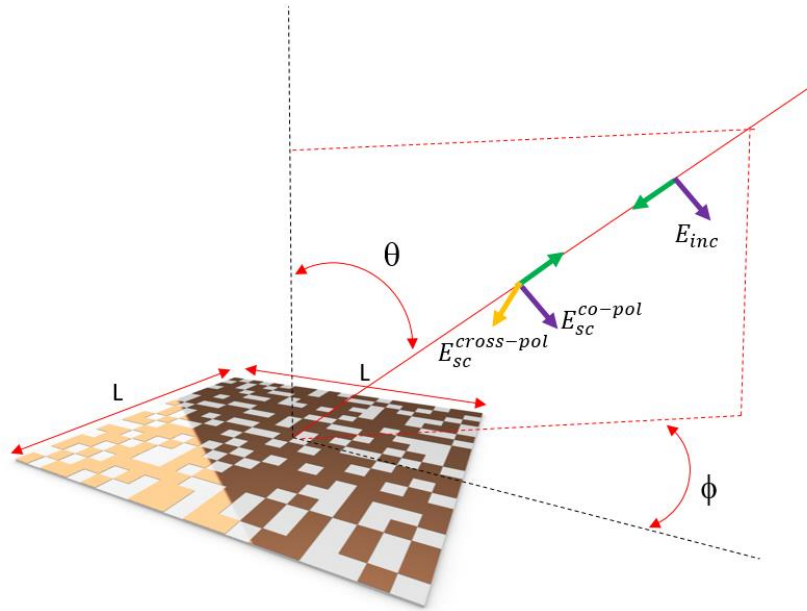


Figure 4.1: Illustration of the coordinate system used to calculate a single particle's backscatter or mono-static RCS.

The formulation used allows for frequency-agnostic solutions. The length of the plate is in units of wavelength, not meters. The patterns found can be scaled to any frequency of interest by multiplying by the appropriate wavelength squared.

This chapter is organized as follows. In section 4.1.1, I will discuss pattern optimization at a single frequency. This analysis also assumes perfect manufacturing of the individual patterned flakes. Sections 4.1.2 and 4.1.3 discuss the optimization of patterns that assumes some manufacturing errors during the pattern registration of individual flakes. This is a practical issue routinely encountered during most scalable manufacturing processes. Pattern designs that are insensitive to registration have “glide symmetry.” For most manufacturing processes, however, the registration is somewhere between perfect and unregistered. In section 4.1.3, I explore the design of optimized patterns assuming some degree of registration. Section 4.1.4 explores the optimal design of patterned flakes over a band of frequencies. In section 4.1.5, I explore the effect of finite conductivity. All previous simulations assumed PEC features that do not exist in the real world. Real flakes fabricated from metal have a large but finite conductivity that can be quantified using the concept of surface impedance.

4.1.1 Backscattered Optimization of Patterned Flakes at a Single Frequency – Assumes Perfect Registration

Generally, one is interested in maximizing the return to the source for a backscattering problem. The model used here will maximize the average monostatic RCS, equation 4.1.

$$\sigma_{avg}^{co} = \frac{1}{2N_{\phi}N_{\theta}} \sum_{\phi_i=1}^{N_{\phi}} \sum_{\theta_i=1}^{N_{\theta}} (\sigma_{\theta\theta} + \sigma_{\phi\phi}) \quad (4.1)$$

N_{ϕ} is the number of incident ϕ azimuthal angles and N_{θ} is the number of incident θ elevation angles. $\sigma_{\theta\theta}$ is the monostatic RCS from a $\hat{\theta}$ polarized incident field in the $\hat{\theta}$ polarized scattered direction. Likewise, $\sigma_{\phi\phi}$ is the monostatic RCS from

a $\hat{\phi}$ polarized incident field in the $\hat{\phi}$ polarized direction. A maximum is sought here. However, optimization algorithms typically seek to minimize a function. A minus sign remedies this, so the cost function becomes

$$cost = -\sigma_{avg} \quad (4.2)$$

The model developed in chapter 3 is now optimized for a range of plate lengths illustrated in figure 3.2 from 0.1λ to 1.5λ . The optimized pattern predicts geometric symmetry ensuring the monostatic RCS spreads evenly with respect to the incident angles. Only 1/8 of the plate needs to generate a new shape that can be reflected and rotated throughout the rest of the square. Figure 4.2 illustrates this. Yellow represents PEC, and blue is free space.

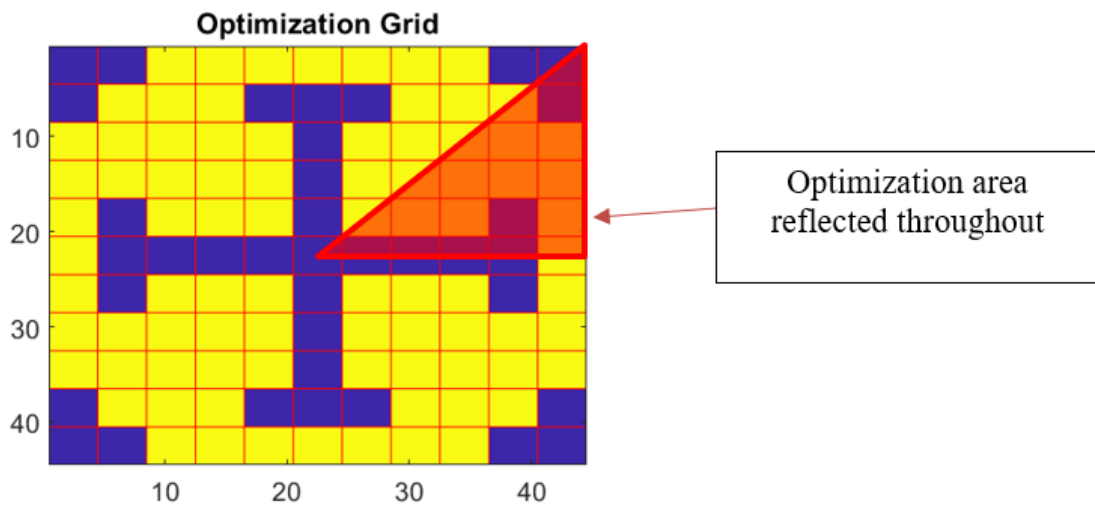


Figure 4.2: Pattern symmetry used for optimization. Pixels in the red triangle are reflected throughout the pattern. Yellow is PEC, and blue is free space

The incident angle θ is optimized over $\left[0, \frac{\pi}{2}\right]$ with 20 points, and ϕ is optimized over $\left[0, \frac{\pi}{4}\right]$ with 10 points. The optimized patterns are presented below.

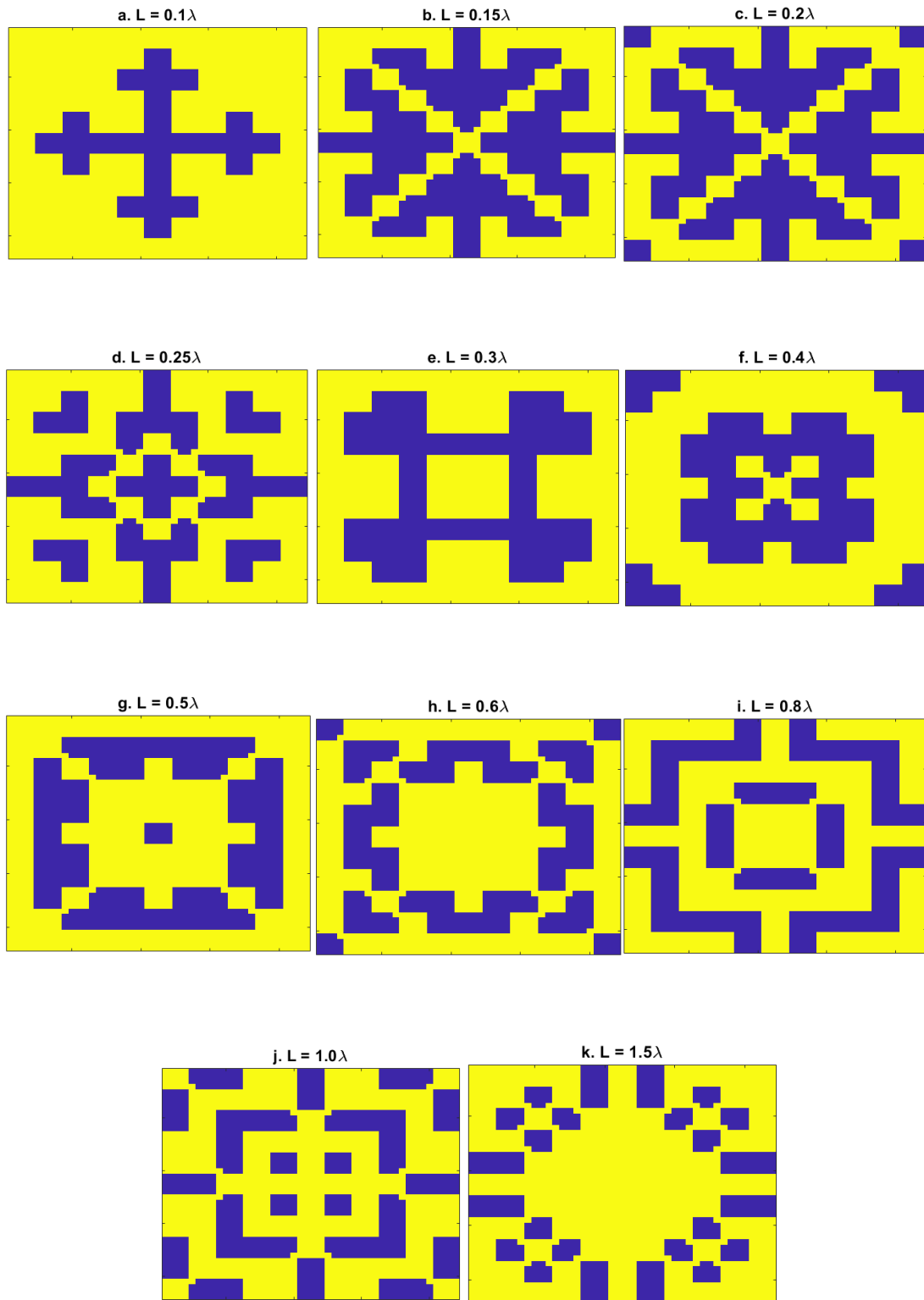


Figure 4.3: Optimized backscattering patterns using co-polarized monostatic RCS where yellow represents PEC and blue represents free space

σ_{avg} is plotted in figure 4.4. The left-hand side images show σ_{avg} over the entire range of plate lengths. Current practice expects that as the plate length approach 0.5λ , an optimized pattern will minimally enhance backscattering. This is the plate length where a fully flooded metalized plate is already optimized for a given frequency. *Unexpectedly, a patterned plate with a length 0.2λ significantly increased the scattering from a fully metalized plate.* A more constrained image is shown in the right-hand graph.

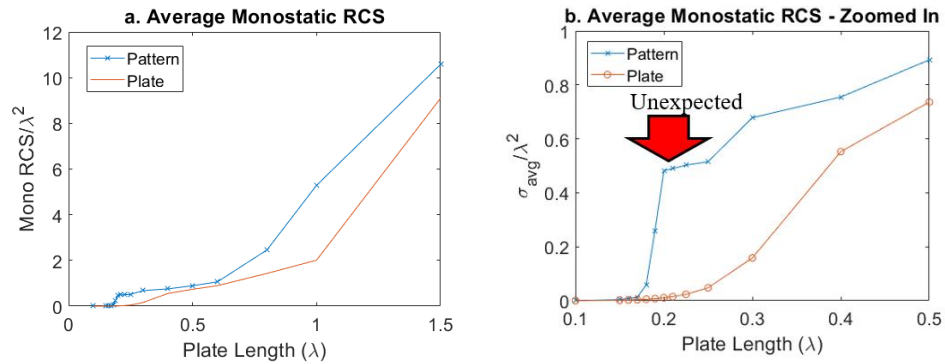


Figure 4.4: Average Monostatic RCS over a range of plate lengths

The “enhancement factor” defined here as

$$EF = \frac{\sigma_{pattern}}{\sigma_{plate}} \quad (4.3)$$

is the average monostatic RCS for a geometric pattern normalized by the average monostatic RCS of a fully flooded plate of the same size. *A plate with 0.2λ length was shown to have an EF of 45.*

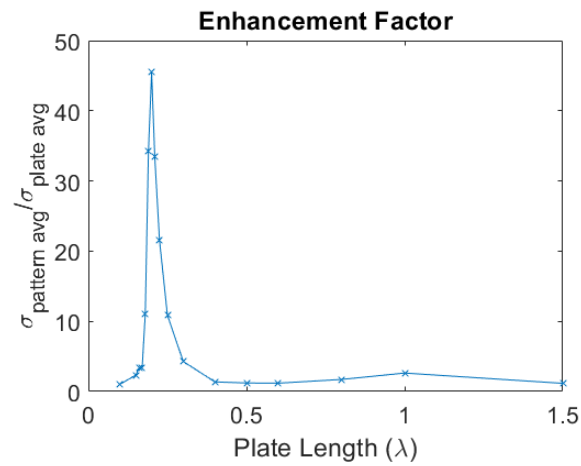


Figure 4.5: $EF = \frac{\sigma_{\text{pattern}}}{\sigma_{\text{plate}}}$

Two patterns' RCS values are presented in full to demonstrate the strength and weaknesses of this algorithm. The most significant improvement is seen at $L = 0.2\lambda$. The graph shows that the optimized pattern is orders of magnitude bigger than a plate of similar size.

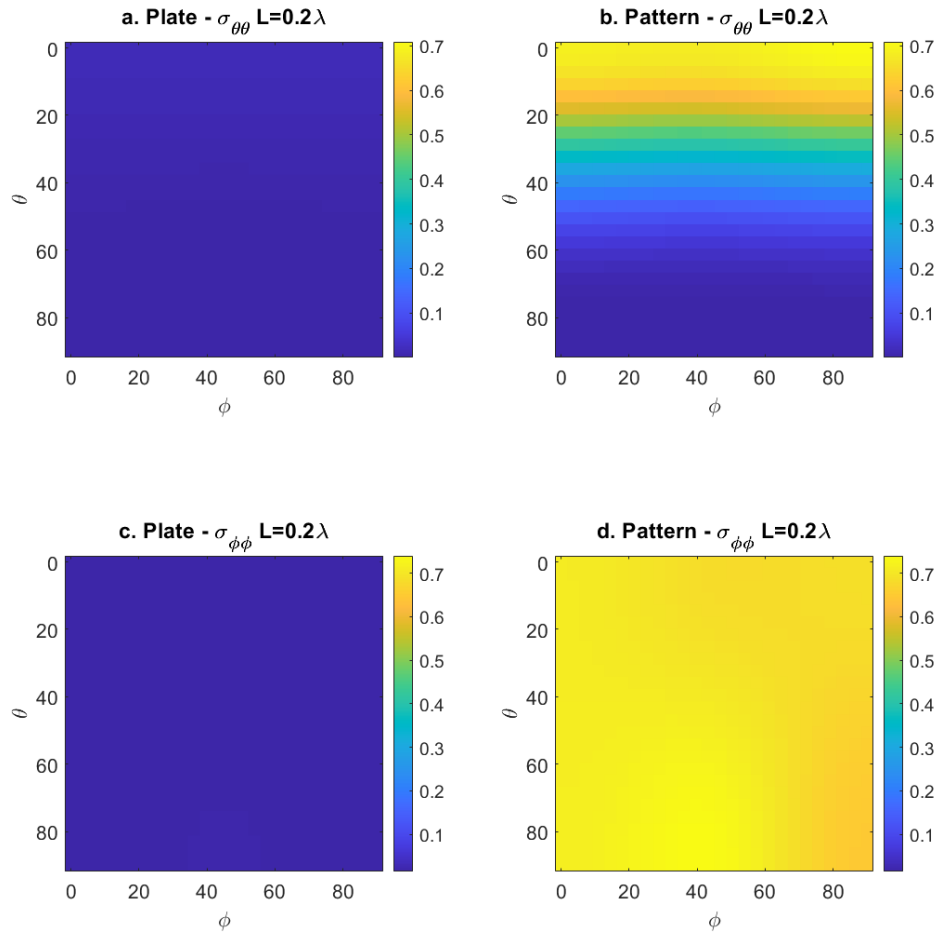


Figure 4.6: Plots of the monostatic RCS of plate length of $L = 0.2\lambda$ for $\sigma_{\theta\theta}$ for a. a plate, b. an optimized pattern, $\sigma_{\phi\phi}$ for c. a plate, and d. an optimized pattern

Likewise, the least amount of improvement is seen at $L = 0.5\lambda$. A slight improvement can be seen, but the RCS values are essentially the same. This is expected because this is the resonance length where a plate behaves optimally.

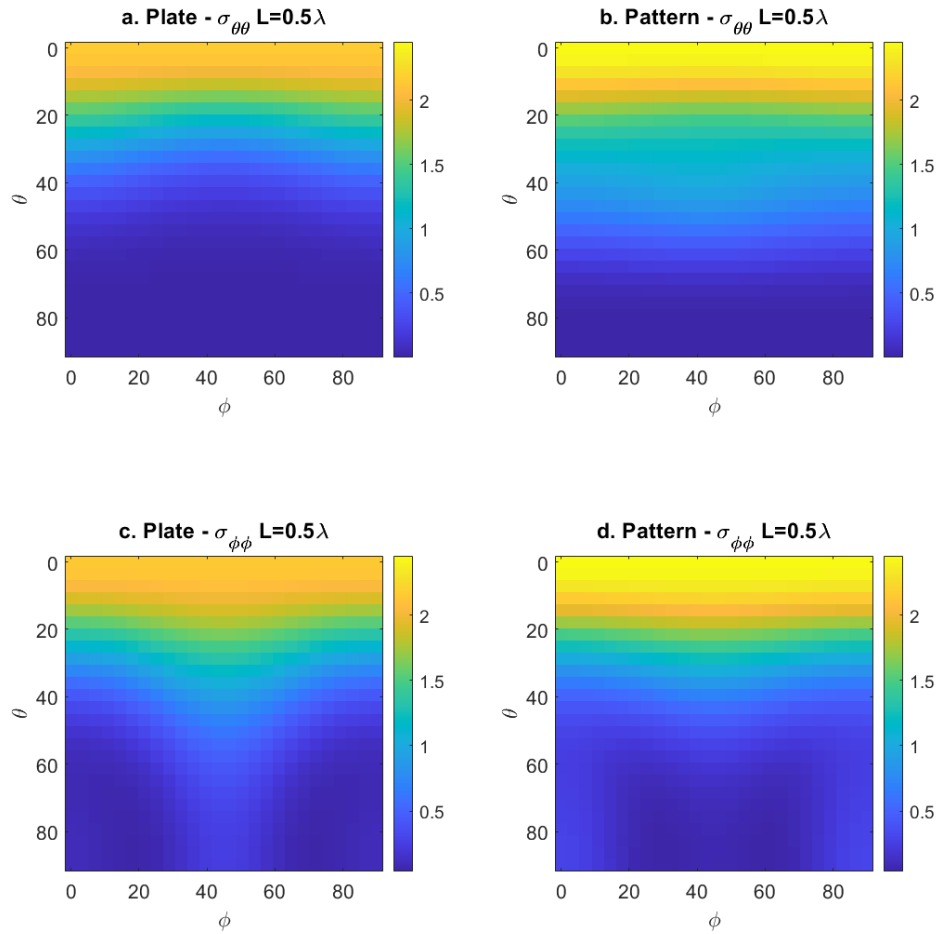


Figure 4.7: Plots of the monostatic RCS of plate length of $L = 0.5\lambda$ for $\sigma_{\theta\theta}$ for a) fully metalized plate, b) optimized pattern, $\sigma_{\phi\phi}$ for c) a plate, and d) an optimized pattern.

All of the optimized pattern's RCS $\sigma_{\theta\theta}$ is plotted at $\phi = 0$ to show the optimized pattern behavior over the entire range. We see for $L < 0.5\lambda$, the optimized pattern is always better than a plate.

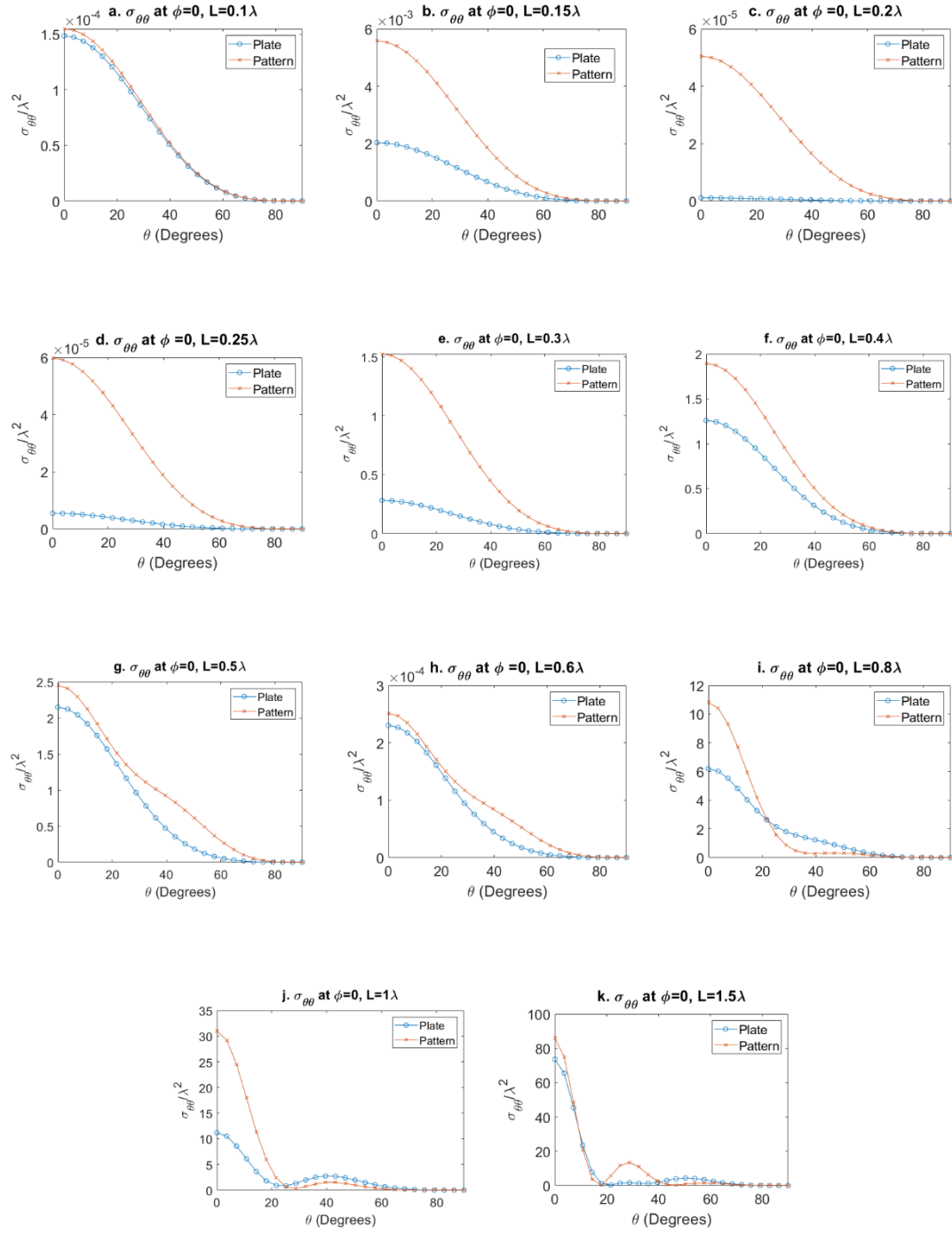


Figure 4.8: $\sigma_{\theta\theta}$ plotted at $\phi = 0, \theta \in [0^\circ, 90^\circ]$ for $L \in [0.1\lambda, 1.5\lambda]$

Next, I validate that I chose a sufficient number of optimization angles. The pattern's average monostatic RCS is recalculated with more incident angles. 90 points are taken in θ , and 45 points are taken in ϕ . Figure 4.9 plots the average monostatic RCS using a higher number of incident angles than the original number of angles used. An average percent difference of 14.09% was found. However, looking at the graph, the error significantly increases as the plate length increases. The median percent difference, 1.28%, was calculated. This is enough angles at most lengths to capture the average RCS.

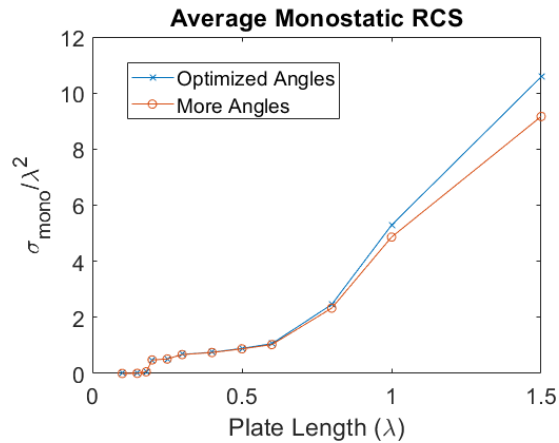


Figure 4.9: Comparing the average RCS with the optimized angles vs increasing the angles

Still, a possible error of 14% is not good. Figure 4.10 instead plots the EF of the increased number of incident angles of the pattern normalized by a similar length plate. The average percent difference of the EF of the optimized incident angles vs the EF of an increased number of incident angles is a minimal value ($2.3325 * 10^{-4}$).

The cost function only optimizes EF, not absolute values. This shows that the number of optimization angles chosen, 200, is sufficient.

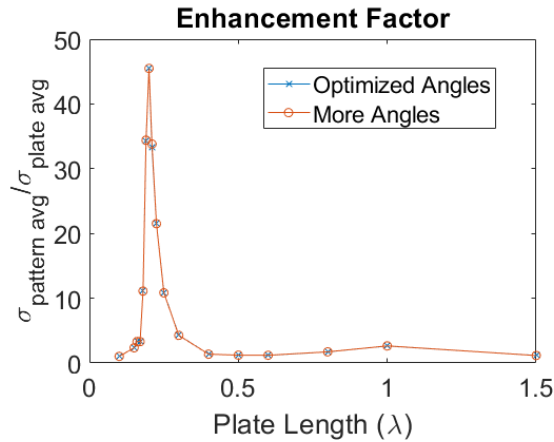


Figure 4.10: EF of optimized incident angles vs more incident angles

Runtime and the number of generations required for each run are shown in figure 4.11. Runtimes averaged 126 minutes. This is a highly efficient model as compared to current commercially available software.

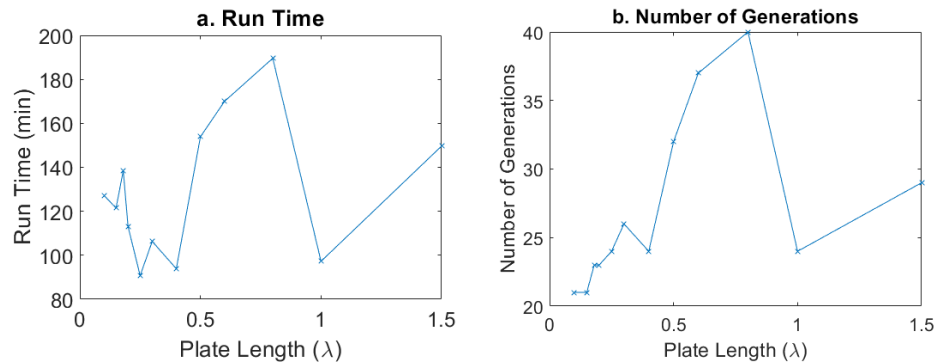


Figure 4.11: a. Runtimes and b. number of generations for the algorithm to find an optimized pattern

4.1.2 Backscattered Optimization of Patterned Flakes at a Single Frequency – Assumes No Registration

Current scalable manufacturing processes involve printing a large surface area containing many patterns using a roll-to-roll printer. Individual designs are cut from the original large surface using rotary die cutters. The spatial resolution of state-of-the-art systems is typically $\pm 0.5\text{mm}$. Small flakes (e.g., $3\text{ mm} \times 3\text{ mm}$) can result in a high degree of registration errors that vary from particle to particle. In this section, I explore the optimal design of patterns that are not sensitive to registration errors.

To this end, I updated the iterative optimization algorithm and cost function to account for the limitation of no registration.

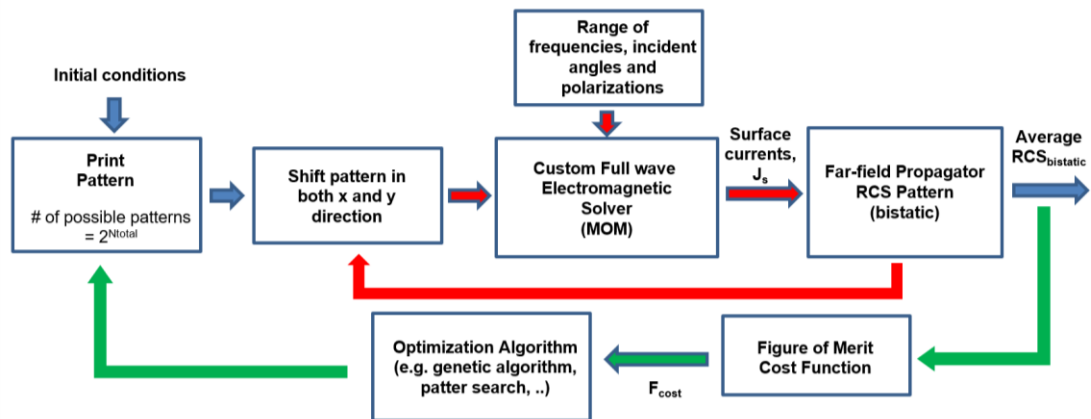


Figure 4.12: Illustration of optimization algorithm, which iteratively tests printed chaff patterns until an optimal design is reached. This algorithm was modified from the original one to account for random lateral shifts of the pattern (or random registration) during fabrication.

Consider a final pattern design with length L . A full PEC plate is generated, but now with size $3L$. A pattern of size L can be created and then replicated in a 3×3 grid.

This makes a design where the optimized pattern of interest sits at the center surrounded by itself, modeling the roll-to-roll process. This process is shown in figure 4.12. The red box represents where the cut could happen during manufacturing. The iterative optimization algorithm was modified to account for the lateral shift of the patterned surfaces, as shown in figure 4.13. As this box moves laterally, the average monostatic RCS is found at each individual point. These lateral movements are then themselves averaged and returned as the cost function:

$$\sigma_{avg} = \frac{1}{2N_{\phi}N_{\theta}N_d} \sum_{D_i=1}^{N_d} \sum_{\phi_i=1}^{N_{\phi}} \sum_{\theta_i=1}^{N_{\theta}} (\sigma_{\theta\theta} + \sigma_{\phi\phi}) \quad (4.4)$$

where N_d is the number of lateral movements in the x and y. D_i is the center position of the red box seen in figure 4.13. Yellow is metal, and blue is a hole.

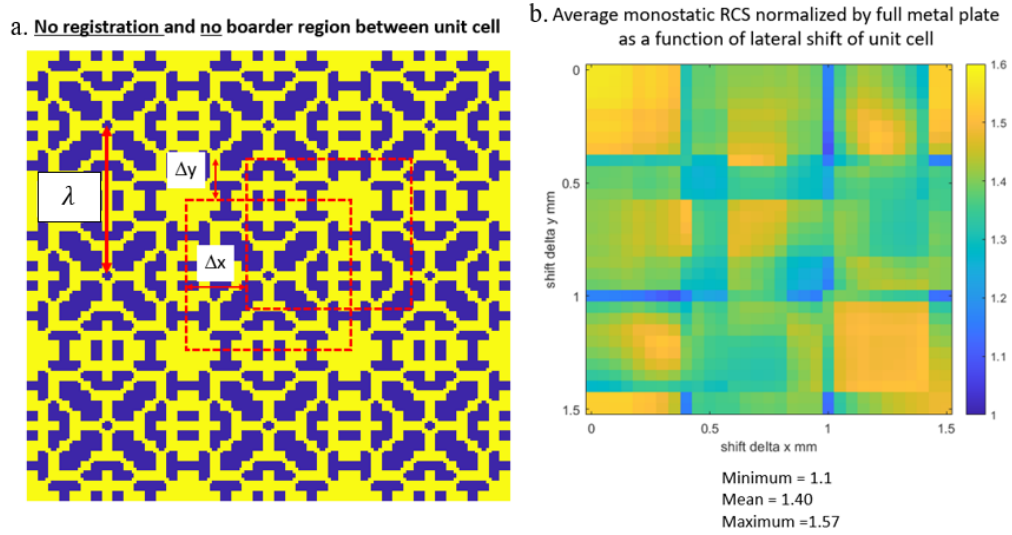


Figure 4.13: a. Optimized pattern showing lateral movement occurring during optimization b. average monostatic RCS at each lateral movement point

Figure 4.13a represents a pattern generated using this procedure. θ was varied between $\left[0, \frac{\pi}{2}\right]$ with 181 angles while ϕ was varied between $\left[0, \frac{\pi}{4}\right]$ with 8 angles. A plate length of $L = 0.3502\lambda$ was optimized. The range of measured EF for all cuts was found to be $1.1 \leq EF \leq 1.57$, with an average of 1.4. This is a wide tolerance. The average monostatic RCS is plotted at each lateral shift point and shown in figure 4.13b.

4.1.3 Backscattered Optimization of Patterned Flakes at a Single Frequency – Partial Registration

No registration harmed the EF. However, in reality, the particles are partially registered with errors that depend on the specific, scalable manufacturing equipment. The simulation was used to investigate the extent of the problem. Partial control over registration case was modeled to explore the effects of no registration on the average monostatic RCS.

A plate with length $L = 0.3502\lambda$ was optimized. The lateral registration was allowed to vary between $\pm 0.0584\lambda$. A PEC border of width 0.1167λ is placed to surround the individual pattern. The incident angles used were 181 elevation angles θ between $\left[0, \frac{\pi}{2}\right]$ and 12 azimuthal angles that varied from $\left[0, \frac{\pi}{4}\right]$. The optimized pattern is shown in figure 4.13.

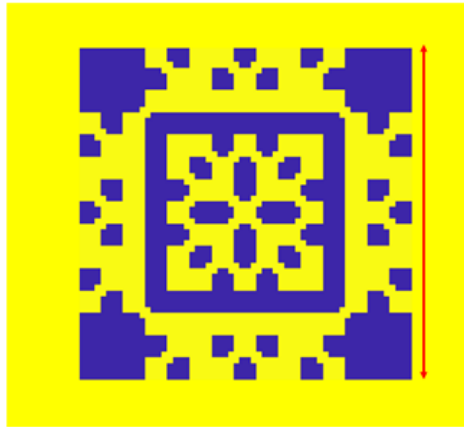


Figure 4.14: Optimized Pattern with some registration. Yellow is PEC and blue is free space.

Figure 4.15 plots the EF. The EF range is shown to be $1.56 \leq EF \leq 1.79$, with an average of 1.74. The EF range is smaller, with a higher average than no registration case. Lack of registration is shown to be a severe problem.

Average monostatic RCS normalized by full metal plate
as a function of lateral shift of unit cell

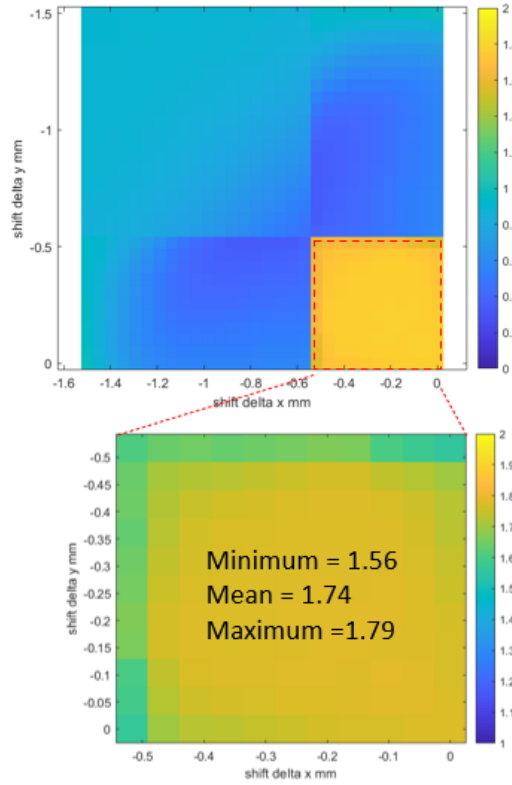


Figure 4.15: Average monostatic RCS normalized by full metal plate as a function of lateral movement

4.1.4 Backscattered Optimization of Patterned Flakes at Multiple Frequencies

The average monostatic RCS in equation 4.1 can be modified to include multiple frequencies.

$$\sigma_{avg} = \frac{1}{2N_{\phi}N_{\theta}N_f} \sum_{f_i=1}^{N_f} \sum_{\phi_i=1}^{N_{\phi}} \sum_{\theta_i=1}^{N_{\theta}} (\sigma_{\theta\theta} + \sigma_{\phi\phi}) \quad (4.5)$$

where f_i is a selected frequency and N_f is the total number of frequencies swept.

The general case describes the plate length in terms of wavelength. When dealing with multiple frequencies, multiple wavelengths are now involved, so this general frequency-agnostic case quickly becomes confusing. The plate parameters will now be given in terms of SI units of length (GHz and meters) to mitigate confusion.

Consider a frequency sweep between 7GHz to 13 GHz. The plate length is set to 1.4989cm, half-wavelength at 10GHz the center frequency. The formulation described in chapter 3 must remain in terms of wavelength. A plate will be generated in terms of its wavelength for each frequency optimized.

Plate lengths relative to 1.5 cm (half-wavelength at 10GHz) are shown below:

Table 4.1: 1.49898cm Plate Lengths in term of wavelength

Frequency (GHz)	Plate length (λ)
7	0.35
9	0.45
10	0.5
11	0.55
13	0.65

Optimized incident angles chosen were θ over $\left[0, \frac{\pi}{2}\right]$ with 20 points and ϕ over $\left[0, \frac{\pi}{4}\right]$ with 8 points. The entire run took 23.91 hour and 27 generations. The evaluation of the cost function at each iteration is shown in figure 4.16.

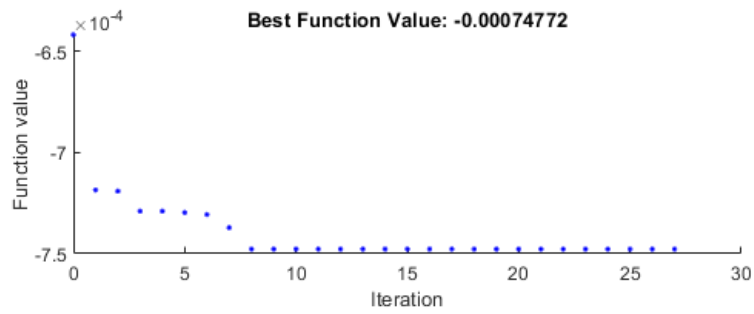


Figure 4.16: Cost function evaluations for 7-13GHz, plate length of 1.4989cm

The final pattern shown in figure 4.17 is a split ring resonator, a well-known metamaterial structure [1].

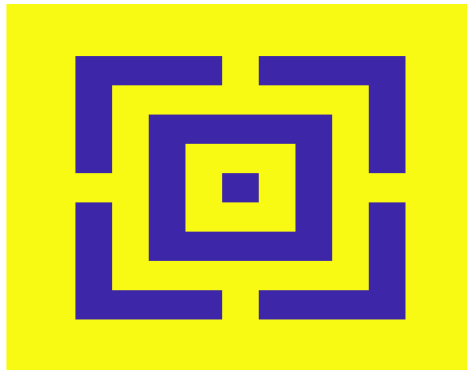


Figure 4.17: Optimized pattern for a plate length 1.4989cm at 7-13GHz where yellow is PEC and blue is free space

The average monostatic RCS of the pattern is plotted against a full PEC plate over the frequency range 5GHz to 15 GHz. The EF of the pattern vs the plate is plotted as well. The average EF of the optimized frequencies is 1.1997.

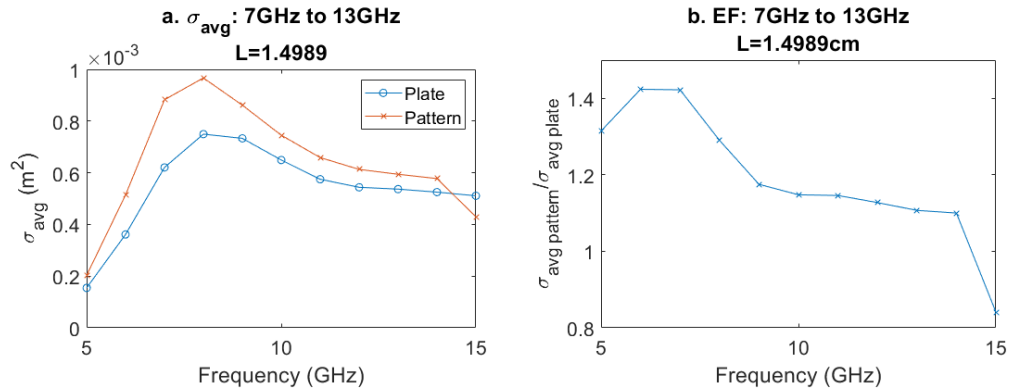


Figure 4.18: Plate length $L = 1.4989\text{cm}$ optimized over $[7,9,10,11,13]$ GHz a. Average monostatic RCS and b. EF over extended frequency range

Another multi-frequency optimization run was attempted to take advantage of the high EF seen at 0.2λ . The plate has a length of 1.1530 cm, half-wavelength for 13 GHz. Plate lengths relative to 1.1530 cm (half-wavelength at 13 GHz) are shown below:

Table 4.2: 1.1530cm Plate Lengths in term of wavelength

Frequency (GHz)	Plate length (λ)
7	0.2692
9	0.3462
10	0.3846
11	0.4231
13	0.5

A modification in the cost function was needed to ensure $EF > 1$ at all frequencies of interest, as shown in equation 4.6.

$$\begin{aligned}
 & \text{cost} \\
 & = - \begin{cases} \min \left(\frac{\sigma_{avgPattern}}{\sigma_{avgPlate}} \right), \frac{\sigma_{avgPattern}(f_i)}{\sigma_{avgPlate}(f_i)} < 1 \text{ for } f_i = 1, 2, \dots, N_F \\ \sigma_{avg}, & \text{else} \end{cases} \quad (4.6)
 \end{aligned}$$

where $\sigma_{avgPattern}$ is an array holding the average monostatic RCS of the pattern at each optimization frequency, $\sigma_{avgPlate}$ is an array holding the average monostatic RCS of the plate at each optimization frequency, f_i is a single frequency and N_f is the total number of frequencies swept.

The first stage ensures $EF > 1$ at each frequency of interest. If this is not achieved, the cost function returns $\min\left(\frac{\sigma_{avgPattern}}{\sigma_{avgPlate}}\right)$. This drives the normalized average monostatic RCS of each frequency to 1. After $EF > 1$ has been achieved, the second stage takes the average monostatic RCS over the frequency band as before, equation 4.4.

Optimized incident angles chosen were θ over $\left[0, \frac{\pi}{2}\right]$ with 20 points and ϕ over $\left[0, \frac{\pi}{4}\right]$ with 8 points. This run took 89.3 hours with 24 generations. A pattern better than a plate at every frequency was not found. This can be seen in figure 4.19. The cost function never passes -1.

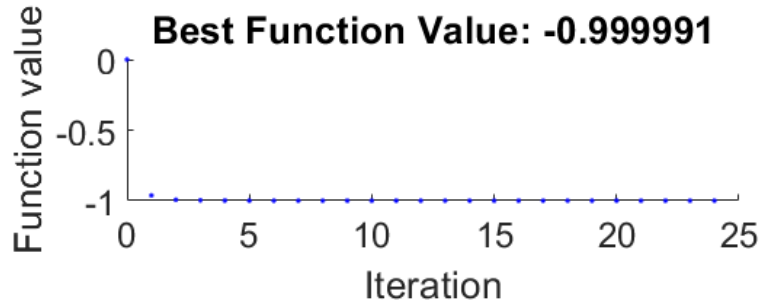


Figure 4.19: Cost function evaluations for 7-13GHz, plate length of 1.1530cm

The design is plotted in figure 4.20, where yellow is PEC and blue is free space.

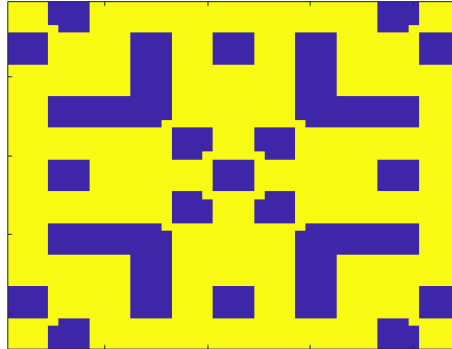


Figure 4.20: Optimized pattern for a plate length 1.1530cm at 7-13GHz where yellow is PEC and blue is free space

The average monostatic RCS is plotted against a full PEC plate. The EF is graphed next to it and had an average of 1.1452.

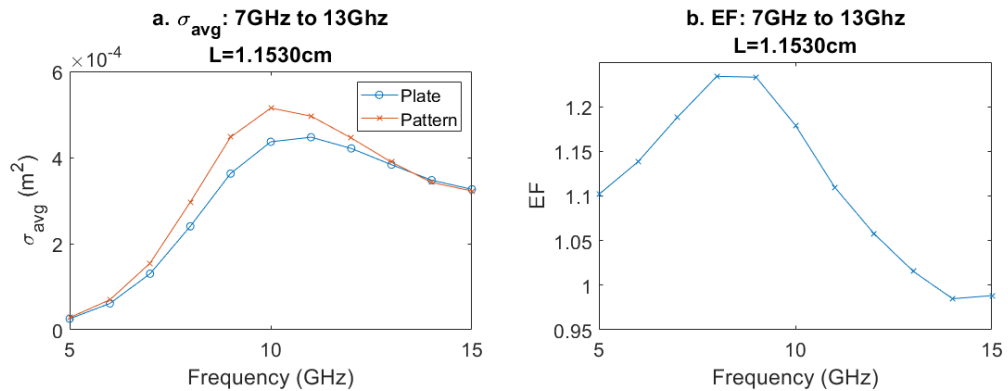


Figure 4.21: Plate length $L = 1.1530\text{cm}$ optimized over [7,9,10,11,13] GHz a. Average monostatic RCS and b. EF over extended frequency range 5 GHz to 15 GHz

This design required four times the amount of computation time and was not able to improve at each optimized frequency. However, the optimized pattern does have some improvement over the frequency band. Singular flakes are generally not of interest. A cartridge contains several particles that disperse as a cloud. The smaller the area of a single particle, the more particles can fit in a cartridge. Decreasing the particle's length reduced the particle's area by 60%. However, there was only a 95% average decrease.

4.1.5 Effects of Finite Conductivity on Backscattered Optimized Patterns

PEC is a useful conceptual model when exploring the effects of scattering. However, it does not exist in the real world. Real metals have conductivity. Chapter 2.2.2b showed that a linear term added to the EFIE models this phenomenon, equation 2.74-2.76.

The single-frequency response patterns were modified with the impedance sheet approximation using a $2\mu\text{m}$ thickness. The conductivity assumed is shown in table 4.3 along with the corresponding Z_L .

Table 4.3: 1.1530cm Plate Lengths in terms of wavelength

σ (S/m)	$Z_L(\Omega)$
PEC	0
$5 * 10^7$	0.01
$5 * 10^6$	0.1
$2 * 10^6$	0.25
$5 * 10^5$	1

The average monostatic RCS with the values given in table 4.3 are plotted in figure 4.22 over the entire range and just at the peak.

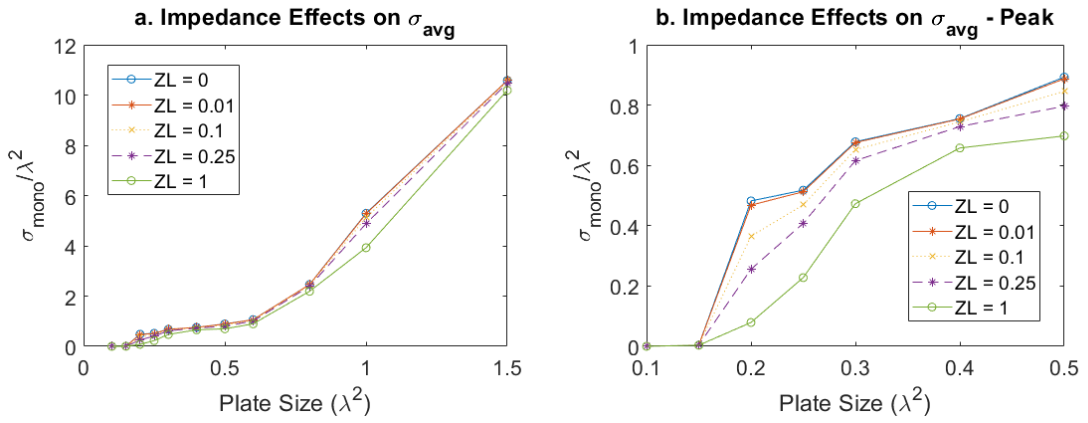


Figure 4.22: Average monostatic RCS of optimized patterns with impedance effects

The peak found at 0.2λ is shown to decrease significantly as impedance increases. This can be seen even more clearly in figure 4.23, where the EF is plotted.

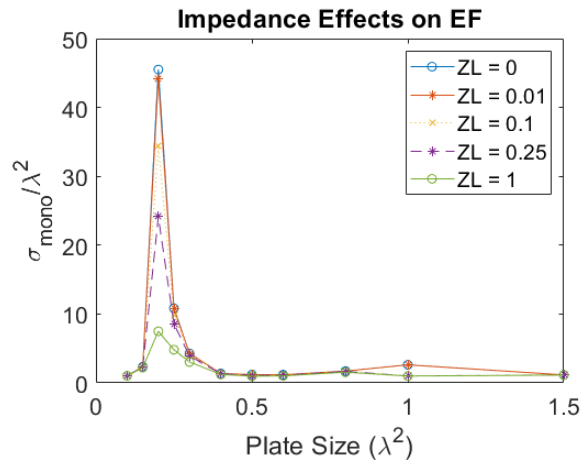


Figure 4.23: Impedance effect on EF of optimized patterns

4.1.6 Summary of Computational Results for Backscatter

This section explored the optimization of co-polarized ($\sigma_{\theta\theta}$, $\sigma_{\phi\phi}$) backscattering. The single-frequency response was first examined for multiple plate lengths. Each length saw some improvement, but a high EF was seen at 0.2λ .

A limitation to our manufacturing was identified. During manufacturing, a person prints multiple patterns using a roll-to-roll process and then cuts out individual designs. The cut location does not have good registration. The cost function was adapted to include this limitation. As expected, the EF decreased significantly from perfect registration (EF=4.28) to no registration ($1.1 \leq EF \leq 1.57$) and now had a wide tolerance depending on the cut location. Section 4.3 shows improvement if some registration is available, decreasing EF tolerance to $1.56 \leq EF \leq 1.79$.

A multi-frequency response was optimized in section 4.4. The optimized frequencies were 7GHz, 9GHz, 10GHz, 11GHz, and 13GHz. A plate length of $L=1.49898\text{cm}$ was first chosen. This is the half-wavelength of 10GHz. The optimized pattern found was a ring resonator-like design, a well-known metamaterial design. Improvement was seen across the frequency band.

Next, the high EF at 0.2λ was utilized for multi-frequency optimization. Now a plate length of $L=1.1530\text{ cm}$ was chosen. Regarding each frequency's wavelength, the plate length now ranged between 0.2 and 0.5. The cost function was modified to improve the pattern performance over the plate at each optimized frequency. This was not achieved in practice though the improvement was seen over the frequency band of interest.

The section concludes by introducing material properties with impedance sheet approximation. The high EF initially seen at 0.2λ is shown to decrease significantly. This might lead to reduced performance in physically manufactured designs.

4.2 Optimization of Co-polarized Forward Scattering from Patterned Plates

In forward wave scattering, the plane wave travels through a medium, and the area of interest is the other side of the medium. The power attenuates as it goes through the medium. Attenuation can occur through two effects 1) absorption and 2) scattering. The extinction cross-section mathematically combines these phenomena. The higher the extinction cross-section, the less power arrives in the forward scattered area. Maximizing the extinction cross-section is needed. Single-frequency optimization is first explored for different plate lengths. Optimization over a frequency band is next. Finally, the chapter concludes with material effects.

4.2.1 Forward Scattered Optimization of Patterned Flakes at a Single Frequency

The formulation found in chapter 3 is frequency independent; all lengths are in terms of the wavelength. The average extinction cross-section is given as

$$C_{ext}^{avg} = \frac{1}{2N_{\phi}N_{\theta}} \sum_{\phi_i=1}^{N_{\phi}} \sum_{\theta_i=1}^{N_{\theta}} (C_{ext}^{\theta\theta} + C_{ext}^{\phi\phi}) \quad (4.7)$$

N_{ϕ} is the number of incident ϕ azimuthal angles and N_{θ} is the number of incident θ elevation angles. $C_{ext}^{\theta\theta}$ is the extinction cross-section from a $\hat{\theta}$ polarized incident field in the $\hat{\theta}$ polarized scattered direction. Likewise, $C_{ext}^{\phi\phi}$ is the extinction cross-section from a $\hat{\phi}$ polarized incident field in the $\hat{\phi}$ polarized direction. The optimizer needs to maximize this value. Optimization algorithms (particle swarm, genetic algorithm, etc...) seek a minimum, so the cost function is written as

$$cost = -C_{ext}^{avg} \quad (4.8)$$

The algorithm forces pattern symmetry, as shown in figure 4.1, again reducing the number of optimization pixels to increase speed. Plate lengths ranging from 0.1λ

to 1.5λ were optimized. The incident angles θ is optimized over $\left[0, \frac{\pi}{2}\right]$ with 20 points, and ϕ is optimized over $\left[0, \frac{\pi}{4}\right]$ with 10 points. Figure 4.24 plots the optimized patterns where yellow is PEC and blue is free space.

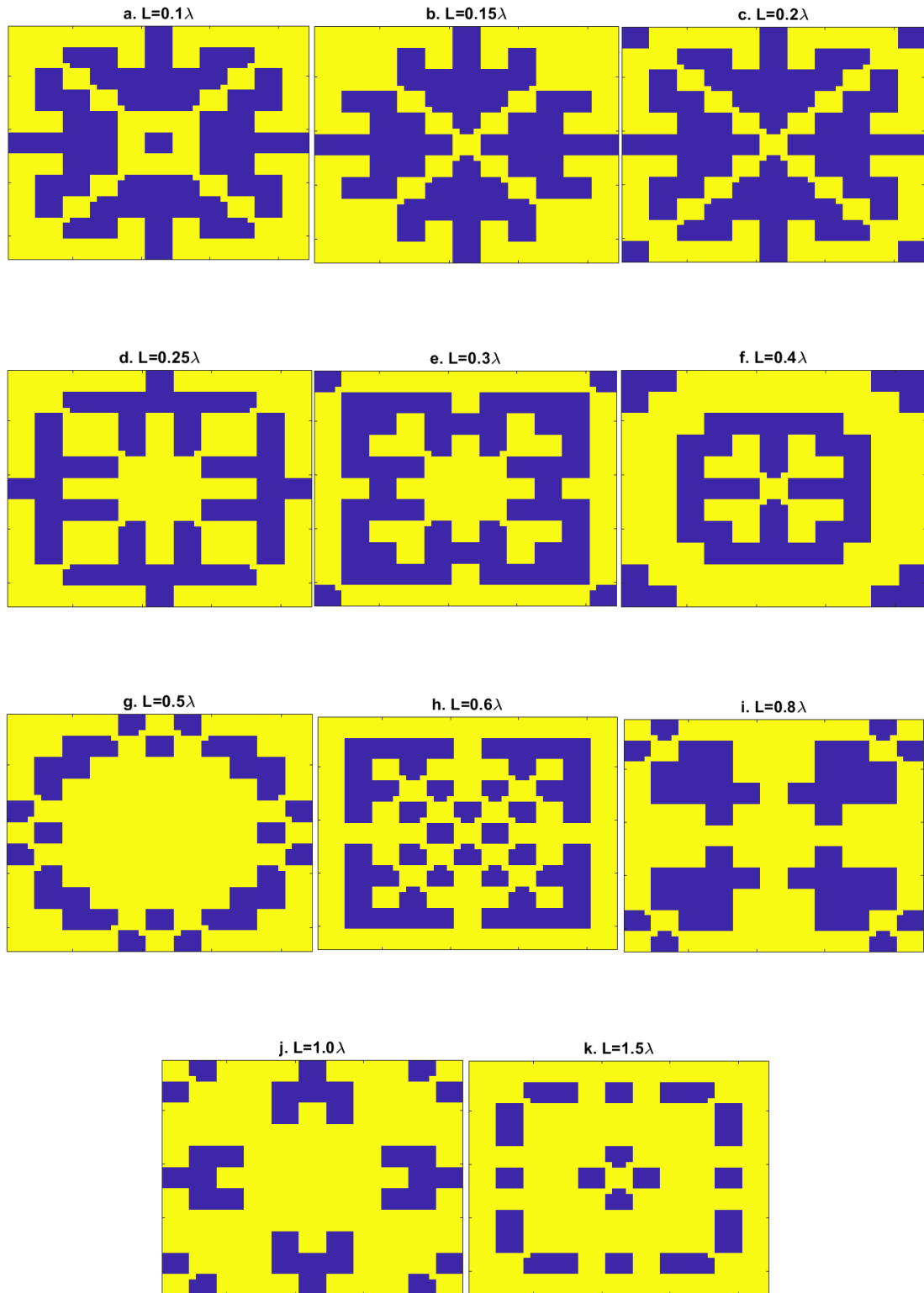


Figure 4.24: Optimized forward scatter patterns for plate length $L \in [0.1\lambda, 1.5\lambda]$.
Yellow is PEC, blue is a free space

The average extinction cross-section C_{ext}^{avg} is plotted in figure 4.25 and a zoom-in between plate lengths 0.1λ and 0.5λ .

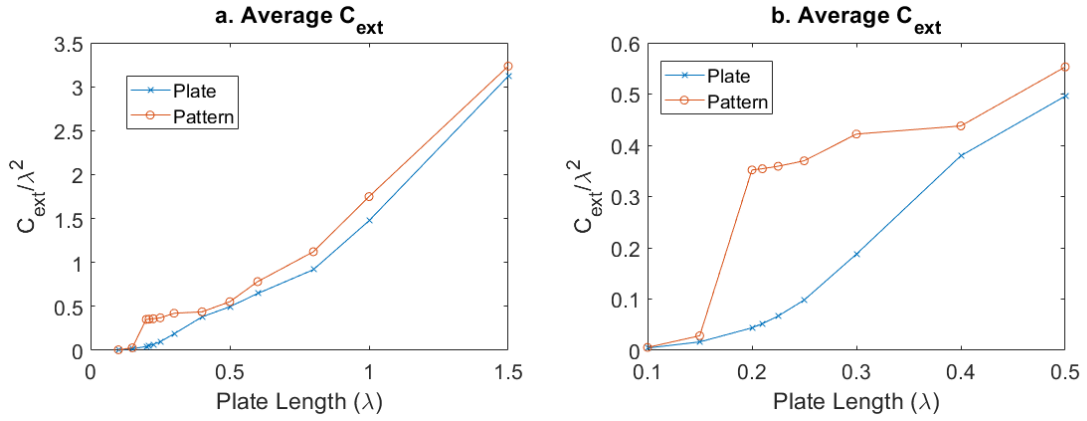


Figure 4.25 a. C_{ext}^{avg} over a range of plate lengths b. Zoomed in view over 0.1λ to 0.5λ

The “enhancement factor” is now defined as

$$EF = \frac{C_{ext}^{pattern}}{C_{ext}^{plate}} \quad (4.9)$$

to track the improvement of the average extinction cross-section of the pattern $C_{ext}^{pattern}$ over the average extinction cross-section C_{ext}^{plate} of the plate. The EF is plotted in figure 4.26.

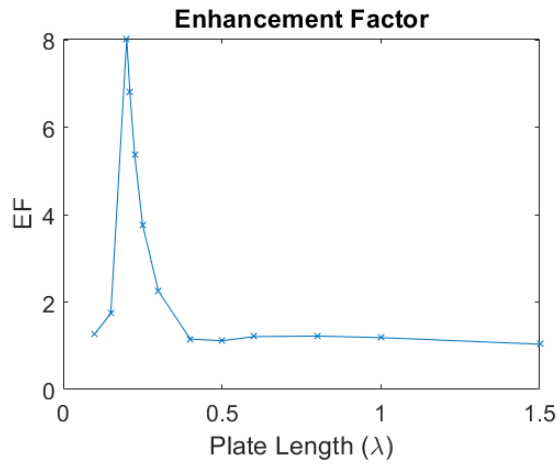


Figure 4.26: $EF = \frac{C_{ext}^{pattern}}{C_{ext}^{plate}}$

Like with backscattering, a significant improvement is seen at 0.2λ . The optimized pattern is, in fact, the same for this length for both forward scattering and backscattering. C_{ext} for both polarizations are plotted at this pattern to show the big improvement.

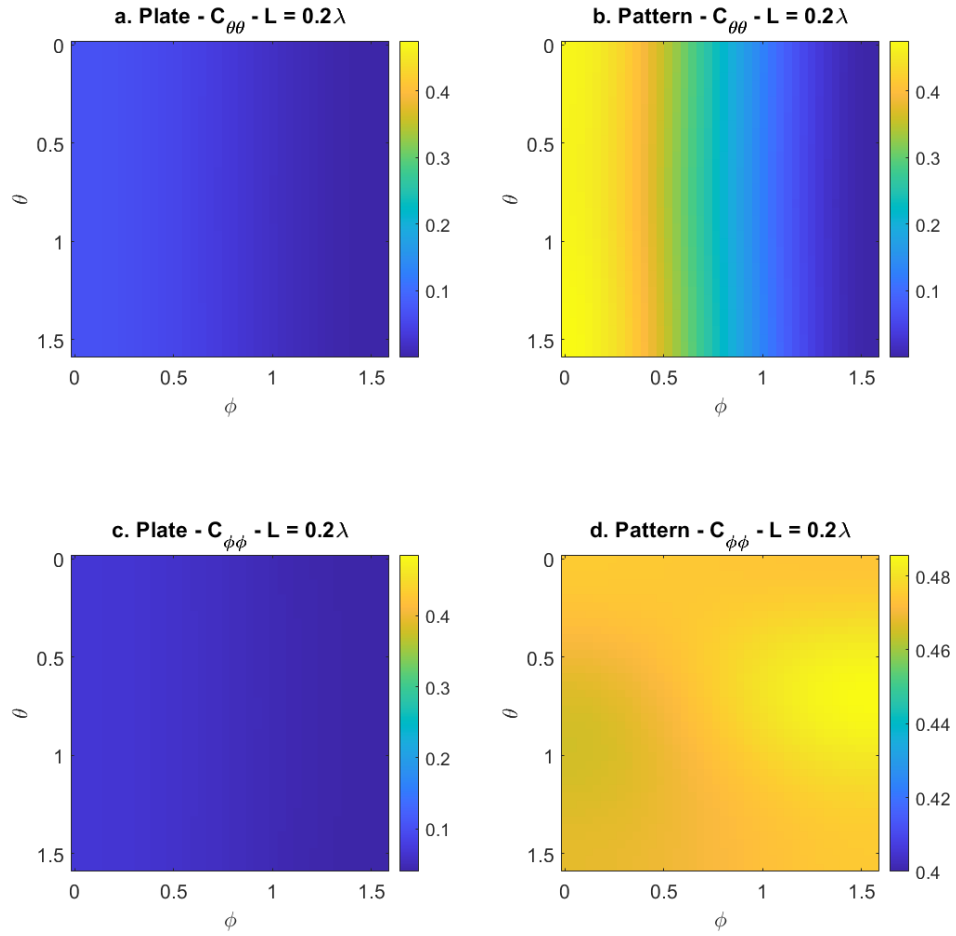


Figure 4.27: C_{ext} is plotted for the optimized pattern at $L = 0.2\lambda$ a. Plate's $C_{\theta\theta}$ b. Patterns's $C_{\theta\theta}$ c. plate's $C_{\phi\phi}$ d. Patterns's $C_{\phi\phi}$

The improvement seen at the resonance length, $L = 0.5\lambda$, is also shown. Again, the optimization algorithm did find much improvement.

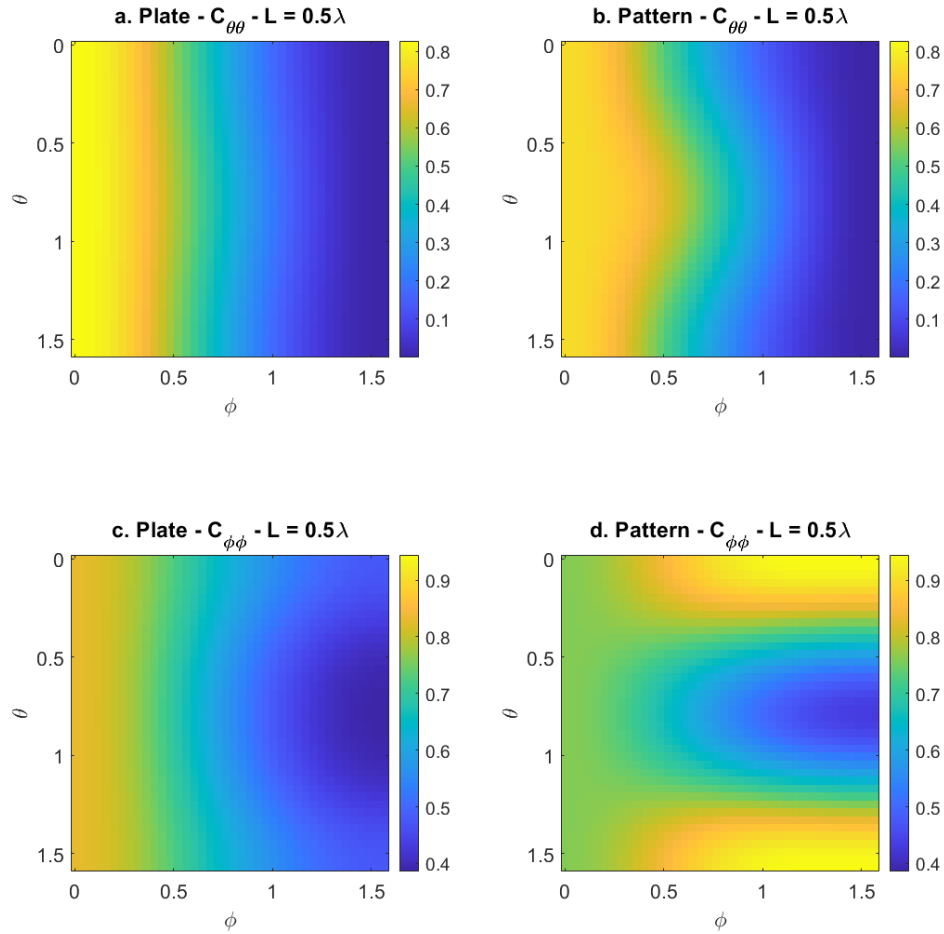


Figure 4.28: C_{ext} is plotted for the optimized pattern at $L = 0.5\lambda$ a. Plate's $C_{\theta\theta}$ b. Patterns's $C_{\theta\theta}$ c. plate's $C_{\phi\phi}$ d. Patterns's $C_{\phi\phi}$

All of the optimized patterns' $C_{\theta\theta}$ are plotted at $\phi = 0$ to track the algorithm's capabilities. As expected, the resonance length sees the most negligible improvement. The optimizer can see higher performance as the plate's length moves away from that value.

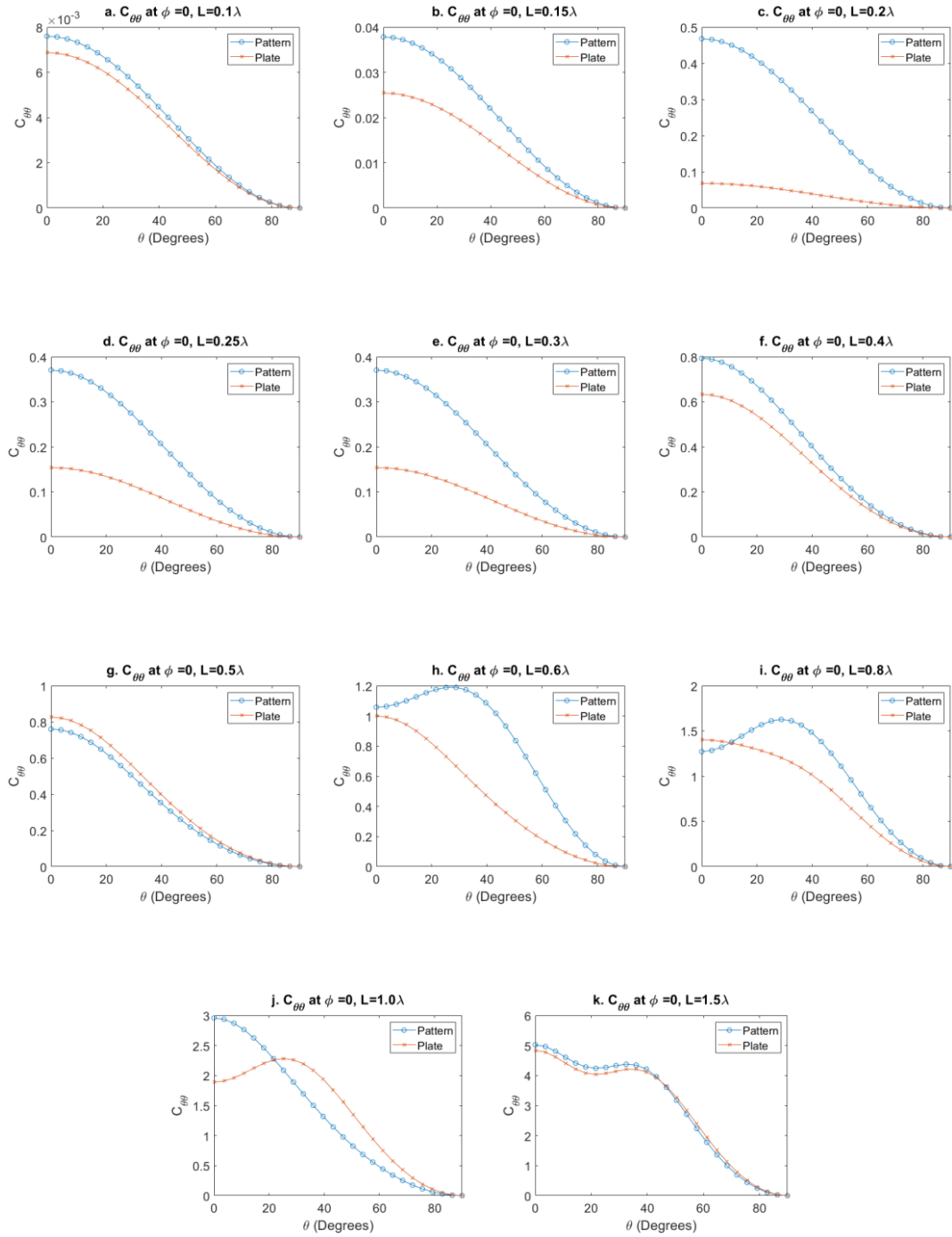


Figure 4.29: The RCS of the optimized forward scatterer vs. the optimized backscatterer patterns

The average monostatic RCS is calculated at the same incident angles for the optimized forward scattering patterns in figure 4.30. For smaller plate lengths, the average monostatic RCS for both optimized forward (C_{ext}) and back (σ) scattering matches implying the scattering term of extinction is dominating. However, once the plate length exceeds 0.25λ the monostatic RCS becomes less for an optimized forward scatterer.

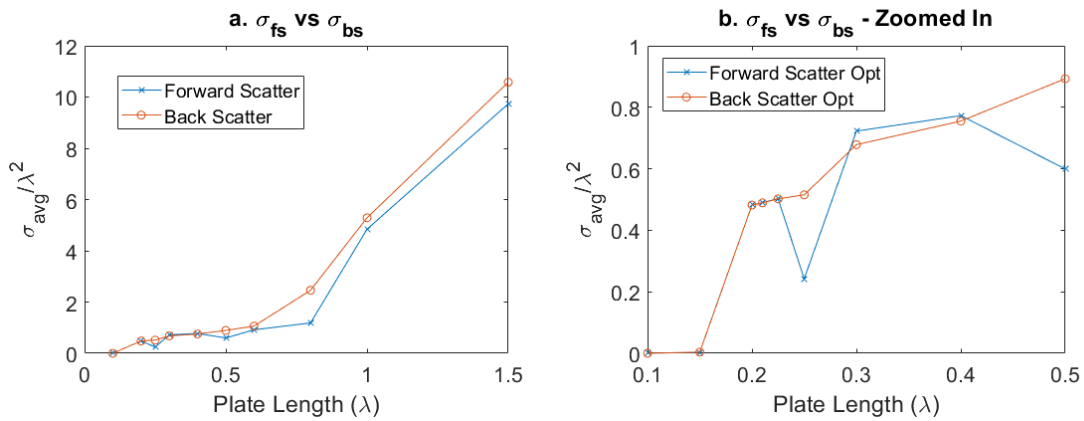


Figure 4.30 The RCS of the optimized forward scatterer vs. the optimized backscatter patterns

I increased the number of optimization angles to 90 points in θ and 45 points in ϕ and recalculated the average extinction cross-section for the optimized patterns. Figure 4.31 plots this. The mean percent difference was only 0.237%.

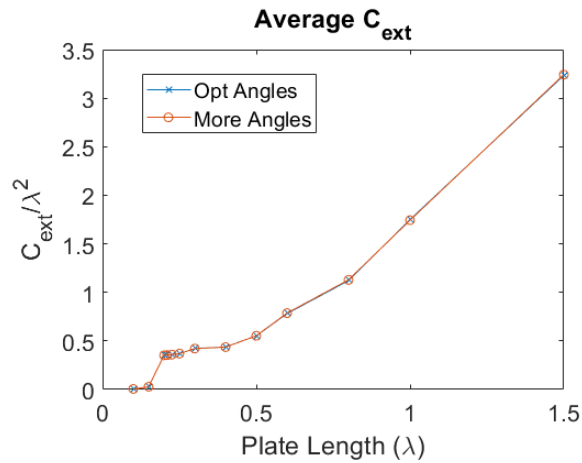


Figure 4.31: Comparing average C_{ext} of optimized angles vs increasing angles

Calculating the EF of more incident angles vs the optimized incident angles further shows minimal differences. The average percent difference is 1.5596×10^{-4} . The cost function used only cares about EF. This indicates that both the optimized angles and increased sampling points produced the same results. The number of optimization angles chosen is sufficient.

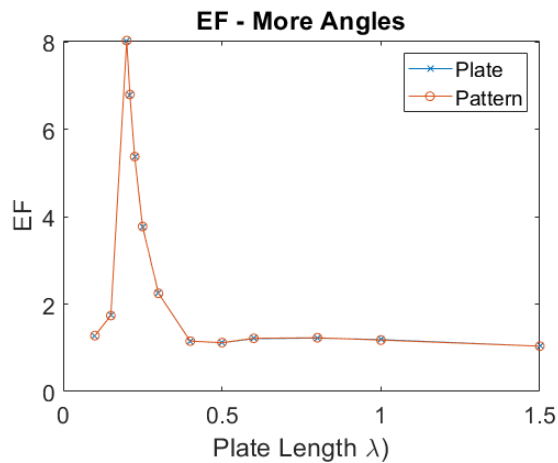


Figure 4.32: EF of optimized incident angles vs more incident angles

Run times and the number of generations for each plate length are plotted in figure 4.33. The average runtime was 315 minutes. The average number of generations needed was 31.

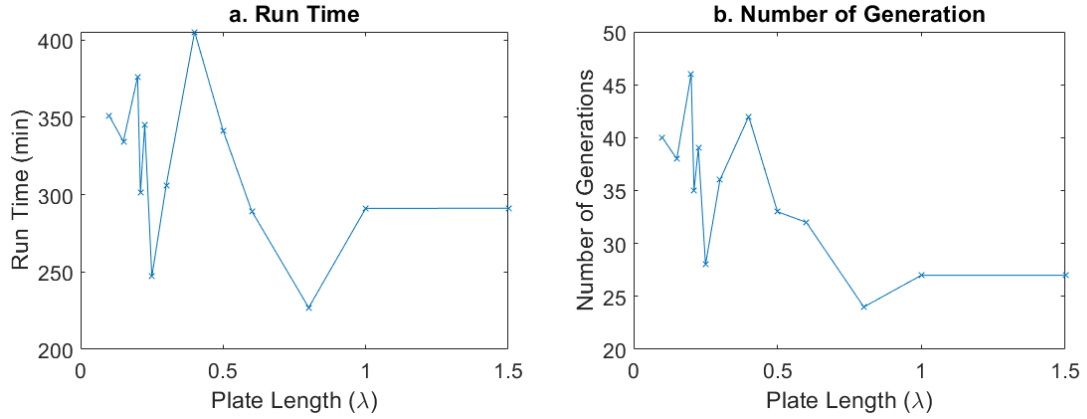


Figure 4.33: Optimized forward scatter a. runtime and b. number of generations

4.2.2 Forward Scattered Optimization of Patterned Flakes at Multiple Frequency

The average extinction cross-section can be modified to include multiple frequencies.

$$C_{ext}^{avg} = \frac{1}{2N_f N_\phi N_\theta} \sum_{f_i=1}^{N_f} \sum_{\phi_i=1}^{N_\phi} \sum_{\theta_i=1}^{N_\theta} (C_{ext}^{\theta\theta} + C_{ext}^{\phi\phi}) \quad (4.10)$$

where f_i is a selected frequency and N_f is the total number of frequencies swept.

A frequency sweep is done for 7 GHz, 9 GHz, 10 GHz, 11 GHz, and 13 GHz. A plate length is set to the center frequencies, 10GHz, half-wavelength, 1.1530 cm. The plate lengths at each frequency relative to their wavelength are given in table 4.1.

The incident optimization angles are again set to θ over $\left[0, \frac{\pi}{2}\right]$ with 20 points and ϕ over $\left[0, \frac{\pi}{4}\right]$ with 8 points. The optimization algorithm converged after 23 generations over 94 hours.

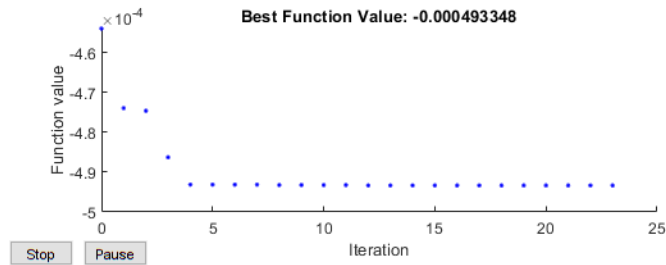


Figure 4.34 Cost function evaluations for 7-13GHz, plate length of 1.4989cm

The resulting pattern is shown below. Once again, a split-ring resonator-like pattern emerged.

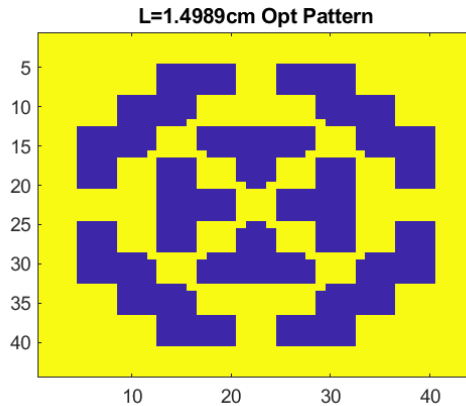


Figure 4.35 Optimized pattern for a plate length 1.4989cm at 7-13GHz where yellow is PEC and blue is free space

The average extinction cross-section C_{ext} , is plotted against the full non-patterned PEC plate from 5GHz to 15 GHz. The EF is also graphed, averaging 1.07 over the optimized frequencies. While the optimized pattern did perform slightly better than a non-patterned plate, the performance over the chosen frequencies, 7GHz to 13GHz, is minimal.

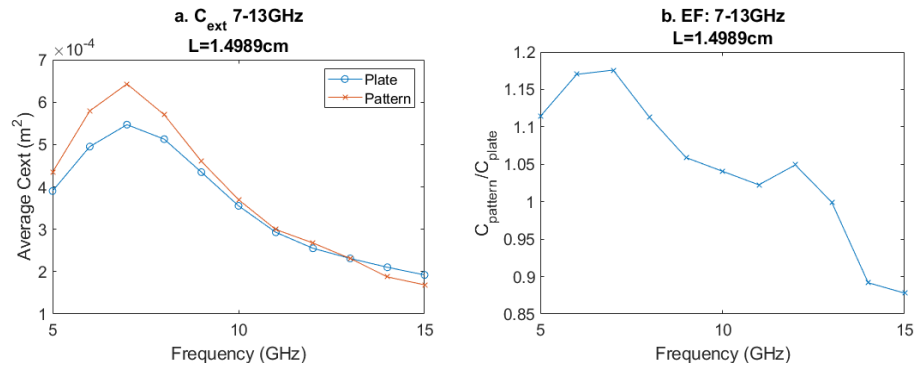


Figure 4.36 The L=1.4989 pattern's a. average C_{ext} b. EF plotted from 5GHz to 15GHz

The next optimized plate length attempts to capitalize on the high EF capabilities seen at 0.2λ over the chosen optimization frequencies 7, 9, 10, 11, 13 GHz, so it is set to $L = 1.11530\text{cm}$. The corresponding plate length in terms of wavelength λ is given in table 4.2. The incident optimization angles are again set to θ over $\left[0, \frac{\pi}{2}\right]$ with 20 points and ϕ over $\left[0, \frac{\pi}{4}\right]$ with 8 points. A solution was found after 81 hours and 23 generations. The cost function evaluation at each generation is plotted below.

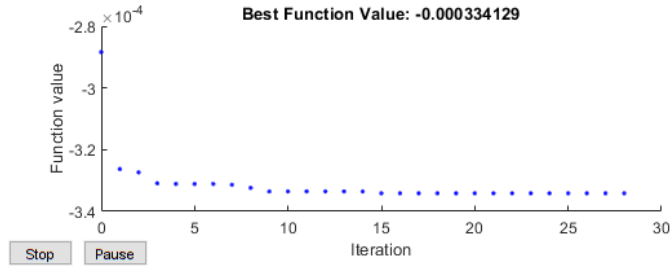


Figure 4.37: Cost function evaluations for 7-13GHz, plate length of 1.1530cm

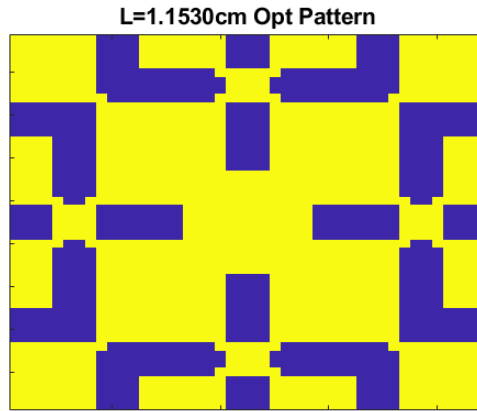


Figure 4.38: Optimized pattern for a plate length 1.1530cm at 7-13GHz where yellow is PEC and blue is free space

The average extinction cross-section C_{ext} and EF of the optimized pattern and full PEC plate is plotted over an extended frequency range from 5 to 15GHz. An average EF in the optimization frequency range is 1.13. Although a better average was found here, the graph clearly shows that the pattern does not behave as well as a full PEC plate in the optimization frequency range.

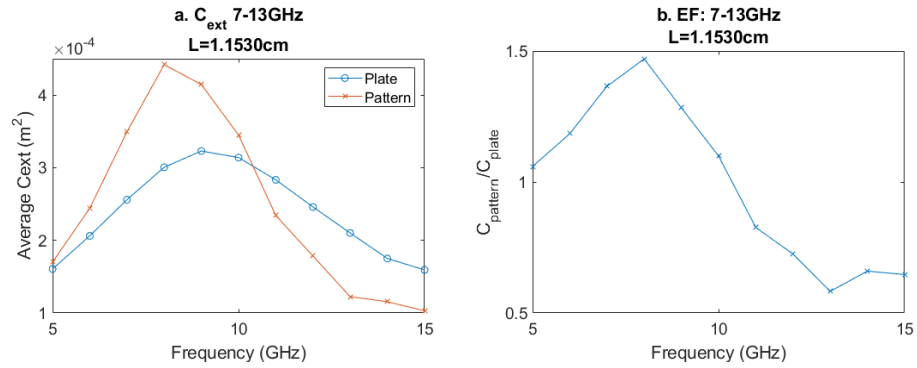


Figure 4.39: The $L=1.1530\text{cm}$ pattern's a. average C_{ext} b. EF plotted from 5GHz to 15GHz

4.2.3 Effects of Finite Conductivity on Forward Optimized Patterns

Material effects on the average extinction cross-section are explored. The optimized patterns from section 5.1 are modified using the impedance sheet approximation described in chapter 2.2.2b. The values used for Z_L are 0, 0.01, 0.1, 0.25, and 1. Table 4.3 relates the impedance sheet Z_L to conductivity σ . The average extinction cross-section and the EF are plotted in figure 4.40.

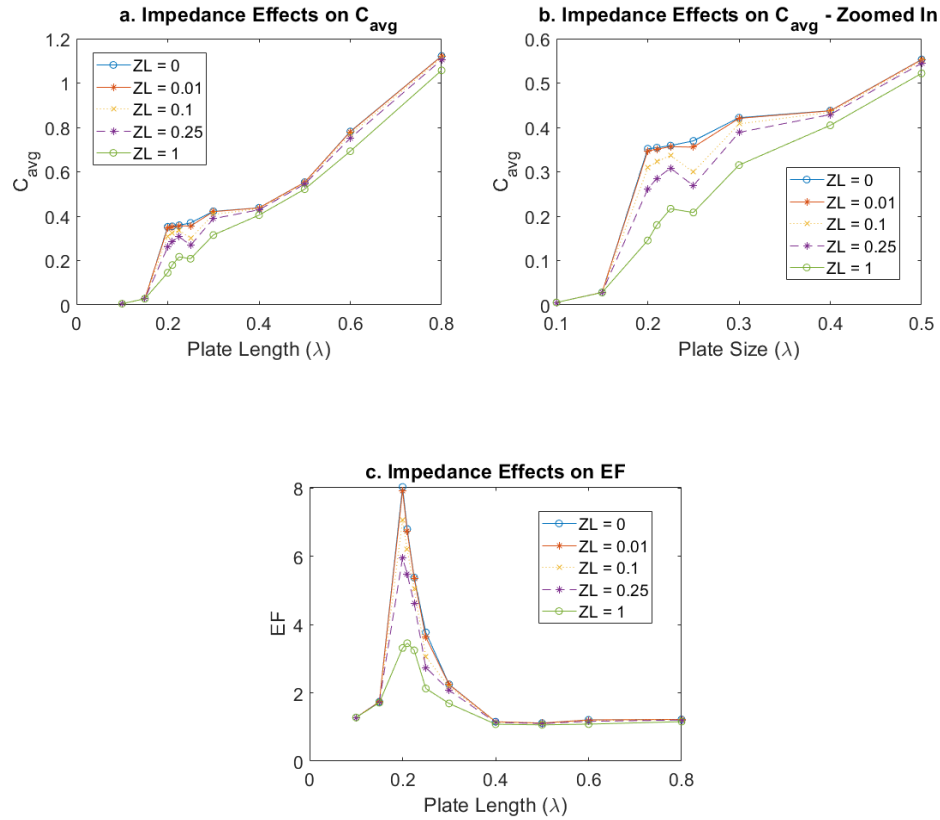


Figure 4.40: Impedance effects on the single frequency optimized patterns a. The average C_{ext} at each length b. a zoomed-in view for $L \in [0.1, 0.5]$ and c. the enhancement factor (EF) variation with surface impedance

The introduction of material properties affects plate lengths with a high increase in EF. The significant improvement found at 0.2λ decreases as Z_L increases just as in backscattering.

4.2.4 Summary of Results for Optimizing Forward Scattering Patterns

The chapter investigated optimizing patterns for minimizing forward scattering through absorption or scattering. The total scattering effects from both can be expressed as an equivalent area, the extinction cross-section. Maximizing C_{ext} means

maximizing attenuation. I first attempted to optimize the single-frequency response over a range of wavelengths. The same high EF at $L=0.2\lambda$ found in the backscattering optimization was also found here with the same pattern. Multi-frequency runs were attempted with some success over 7GHz to 13GHz. A ring resonator-like pattern emerged when the plate length was set to half-wavelength at the center frequency. However, neither design saw great improvement. The chapter ends by examining material effects on single-frequency patterns. Once again, the high EF seen at $L=0.2\lambda$ is diminished as impedance increases.

4.3 Optimization of Co and Cross-Polarized Back Scattering

In previous sections, the goal was to maximize the scattering parameters. This led to the cross-polarized term being disregarded. Compared to the co-polarized scattering terms, the cross-polarization is much smaller. In this section, the effects of the cross-polarized terms ($\sigma_{\theta\phi}, \sigma_{\phi\theta}, C_{ext}^{\theta\phi}, C_{ext}^{\phi\theta}$) are now considered during optimization.

Introducing this new term (cross polarization) presents a unique challenge; ensuring improvement of one scattering is not detrimental to the other. Three different schemes will be investigated to accomplish this 1) symmetric designs, 2) symmetric with ratio controlling the co and cross-polarization, and 3) non-symmetric designs with ratio controlling for the co and cross-polarization.

4.3.1 Optimization Schemes for Co- and Cross-Polarized Backscattering

Three different scenarios are considered. First, the plate symmetry used in previous sections and seen in figure 4.1 is used. The cost function is updated using the EF of the cross-polarized RCS and the EF of the co-polarized. Both EFs are driven to

be greater than one to ensure performance is at least as good as a PEC plate for both the cross-polarized and co-polarized scattering terms. The cost function then returns the average of the two EFs. The cross-polarization will be shown to increase significantly and thus dominate the average.

The second scenario keeps the ratio of the co-polarized EF and cross-polarized EF within a defined bound. This corrects attempts to correct for the cross-polarized RCS domination

The final scenario removes the plate symmetry. [1] demonstrated a non-symmetric shape, an arrow, can significantly affect scattering parameters. The optimization algorithm now attempts to optimize every pixel without regard to symmetry. As expected, the run times significantly increase, but non-intuitive patterns with increased scattering performance than the symmetric patterns are found.

4.3.2 Symmetric Designs with No Ratio Control for Co- and Cross-polarized Backscattering

The most apparent attempt is to repeat the algorithm defined in chapters 4 and 5, but now considering the average cross-polarized RCS defined as

$$\sigma_{avg}^{cross} = \frac{1}{2N_{\phi}N_{\theta}} \sum_{\phi_i=1}^{N_{\phi}} \sum_{\theta_i=1}^{N_{\theta}} (\sigma_{\theta\phi} + \sigma_{\phi\theta}) \quad (4.11)$$

The cross-polarized scattering is orders of magnitudes smaller than the co-polarized defined in equation 4.1. The values must be normalized to ensure that the co-polarization scattering does not dominate. The enhancement factor (EF) defined in equation 4.2 is used. The cost function is defined as the cross-polarization EF is averaged against the co-polarization EF.

$$cost_{sym,no\ ratio} = \frac{EF_{co} + EF_{cross}}{2} = \frac{1}{2} \left[\left(\frac{\sigma_{pattern}}{\sigma_{plate}} \right)_{co} + \left(\frac{\sigma_{pattern}}{\sigma_{plate}} \right)_{cross} \right] \quad (4.12)$$

The symmetry defined in figure 4.1 is assumed to be true again. Only 1/8 of the pattern needs to be optimized, and that section is then rotated and reflected. This significantly reduces the number of optimized points, so faster runtimes can be achieved.

4.3.3 Symmetric Designs with Ratio Control for Co- and Cross-polarized Backscattering

A problem exists with the previous cost function. The average improvement is taken, so one term can dominate the average. This can be corrected by forcing the ratio of the co- and the cross-polarized RCS to be some bounds. The cost function is therefore updated to

$$cost_{sym,ratio} = \begin{cases} \frac{1}{a} \frac{\sigma_{avg,co}}{\sigma_{avg,cross}} & \frac{\sigma_{avg,co}}{\sigma_{avg,cross}} < a \\ b * \frac{\sigma_{avg,cross}}{\sigma_{avg,co}} & \frac{\sigma_{avg,co}}{\sigma_{avg,cross}} > b \\ \frac{EF_{co} + EF_{cross}}{2} & , else \end{cases} \quad (4.13)$$

where the ratio is bounded to $a < \frac{\sigma_{avg,co}}{\sigma_{avg,cross}} < b$. $\sigma_{avg,co}$ is the average co-polarized RCS and $\sigma_{avg,cross}$ is the average cross-polarized RCS.

4.3.4 Non-symmetric Designs with Ratio Control for Co- and Cross-polarized Backscattering

Previous work [18,20,34-35] has shown that non-symmetric patterns can significantly affect the scattering parameters. [34] used arrows to reduce scattering. [25] used rotational symmetry rather than reflection for RCS reduction. An optimization scheme for an arbitrary antenna is given in [20] that uses no symmetry.

All geometrical symmetry is removed from my designs to attempt maximizing radiation. Every pixel is now its own optimization variable. The cost function 4.13 is used again.

4.3.5 Results of the Optimized Co- and Cross-polarized Backscattering Patterns

The algorithm was used to optimize seven patterns from 0.1λ to 0.5λ . The incident angles were varied over $\theta \in \left[0, \frac{\pi}{2}\right]$ with 20 points and $\phi \in \left[0, \frac{\pi}{4}\right]$ with 10 points.

The optimized patterns are shown below

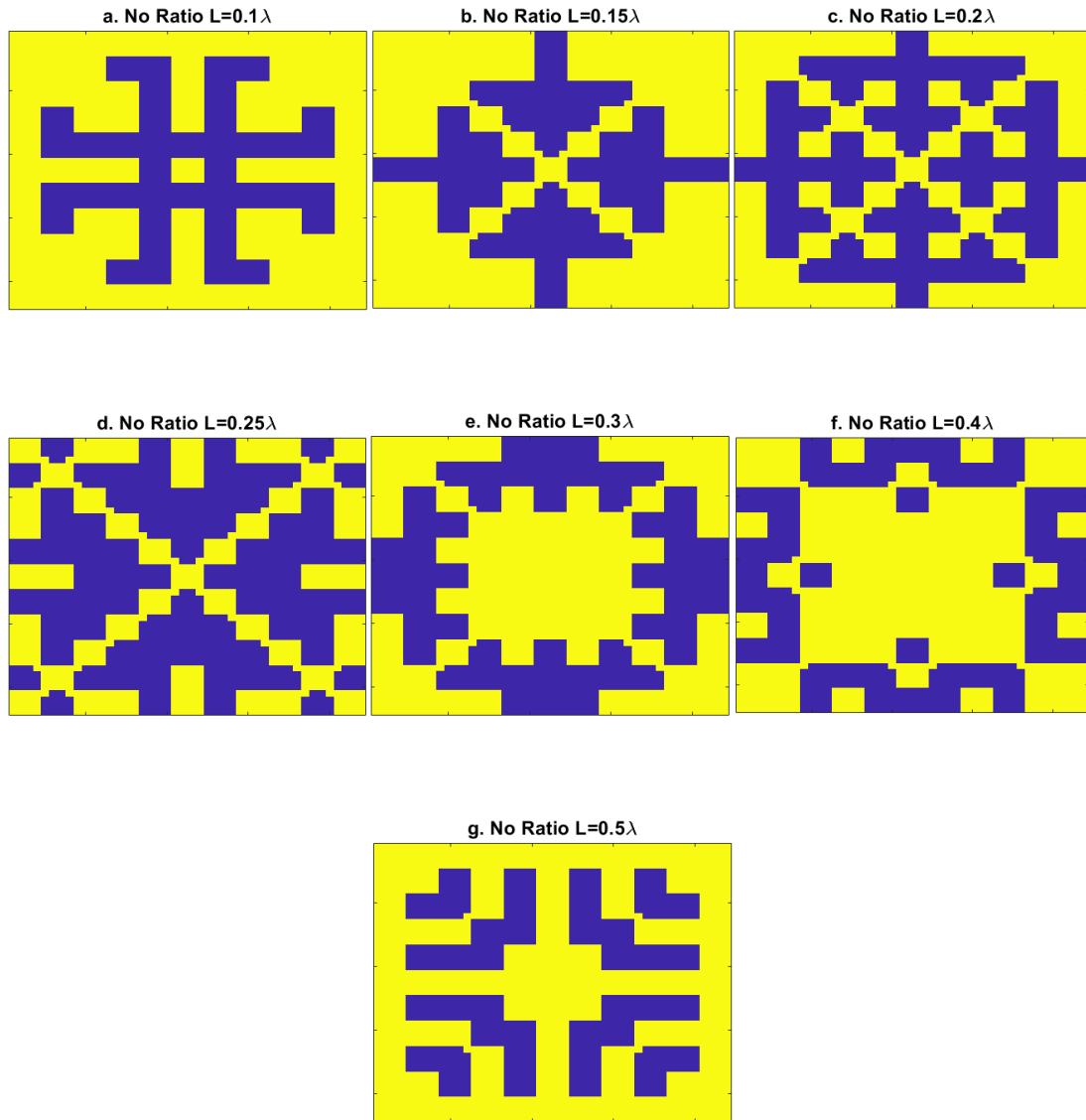


Figure 4.41: Symmetric patterns and no attempt at ratio control varying between 0.1λ to 0.5λ lengths. Yellow is PEC and blue is free-space

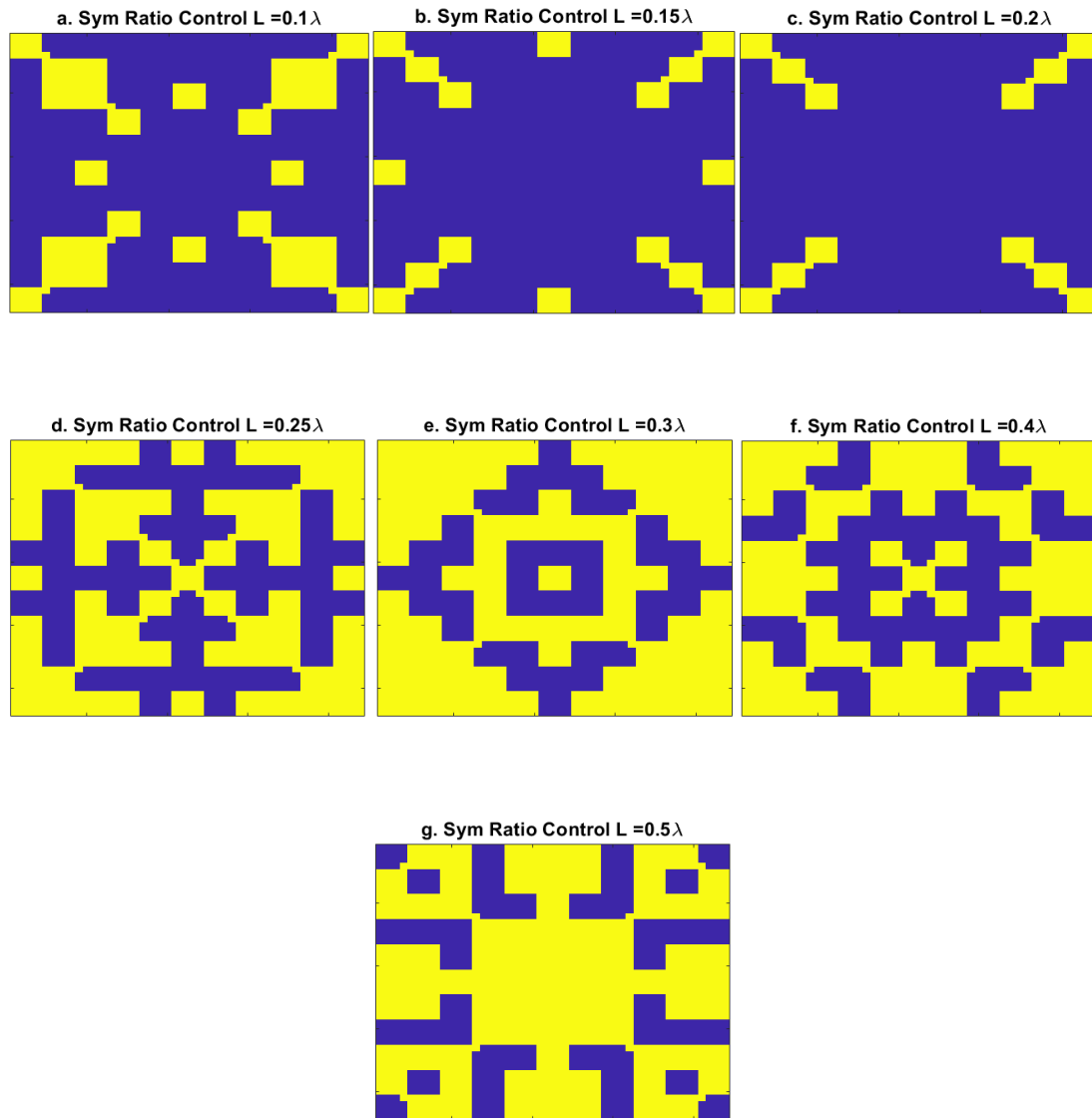


Figure 4.42: Symmetric patterns and ratio control ($9 < \frac{\sigma_{co}}{\sigma_{cross}} < 11$) varying between 0.1λ to 0.5λ lengths. Yellow is PEC and blue is free-space.

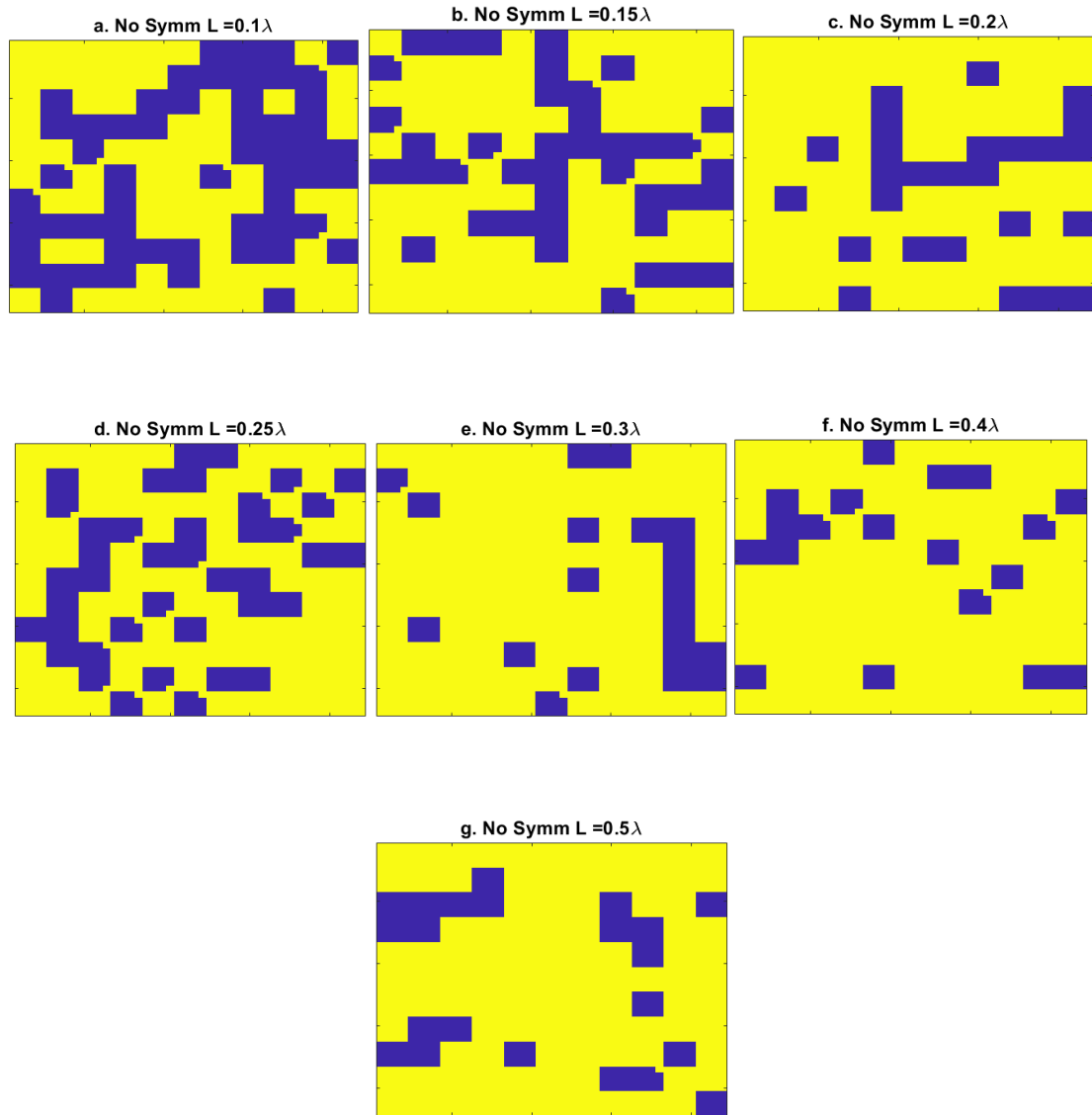


Figure 4.43: Non-symmetric patterns and ratio control ($9 < \frac{\sigma_{co}}{\sigma_{cross}} < 11$) varying between 0.1λ to 0.5λ lengths. Yellow is PEC and blue is free-space

For figure 4.41, a familiar ‘x’ shape is seen in $L = 0.15\lambda$ to 0.3λ , which was previously found in previous chapters. They appear to make a saltire arrow [34-35] used as an artificial magnetic conductor for cross-section reduction. Figure 4.42 shows

symmetric patterns where a ratio control ($9 < \frac{\sigma_{co}}{\sigma_{cross}} < 11$) is attempted. The most obvious result here is that for $L < 0.2$, essentially, no solution was found. Figure 4.43 shows ratio control where symmetry is no longer required. None of the patterns found are intuitive.

The raw RCS values of the co and cross-polarized RCS are plotted below, along with the enhancement factor. The co-RCS is compared against the optimized patterns found in section 4.1 as “the best” improvements.

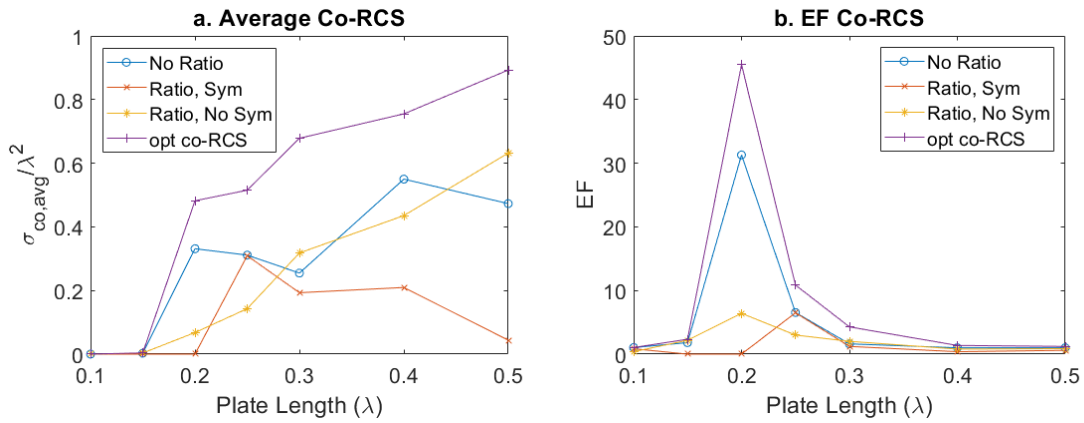


Figure 4.44: a. Average co-polarized RCS and b. EF for no ratio control with symmetry, ratio control with symmetry, ratio control with no symmetry, optimized co-polarized designs

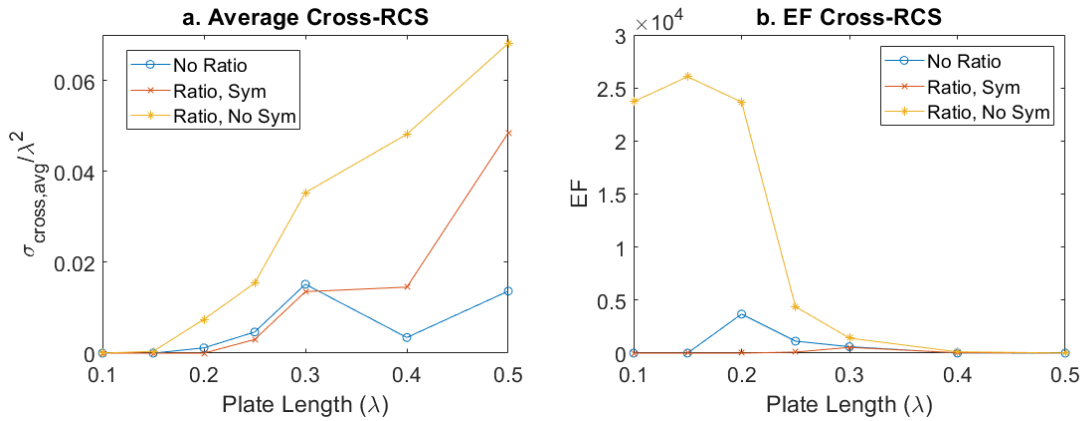


Figure 4.45: a. Average cross-polarized RCS and b. EF for no ratio control with symmetry, ratio control with symmetry, ratio control with no symmetry, optimized cross-polarized designs

It can be seen more clearly that forcing ratio control with symmetry restriction leads to no solution by looking at the EF of the co- and cross-polarized RCS. For $L < 0.25\lambda$, the EF for both values was less than one (i.e., no improvement over a fully metalized plate).

The ratio-controlled non-symmetric patterns offer the most balance. The raw co-RCS seen in figure 4.45 tracks the optimized co-EF pattern from chapter 4 at a reduced magnitude. However, for $L = 0.4\lambda$, the co-EF is 0.79, and for $L = 0.5\lambda$, the co-EF is 0.87. As the length approaches the resonant length, this scheme did not produce results better than a metalized plate. This allowed for more energy to be reflected in the cross-RCS, which increased linearly with plate length and is higher than the other schemes. This is further supported by the cost function value seen in figure 4.46. The ratio controlled non-symmetric patterns is orders of magnitudes greater than the other schemes.

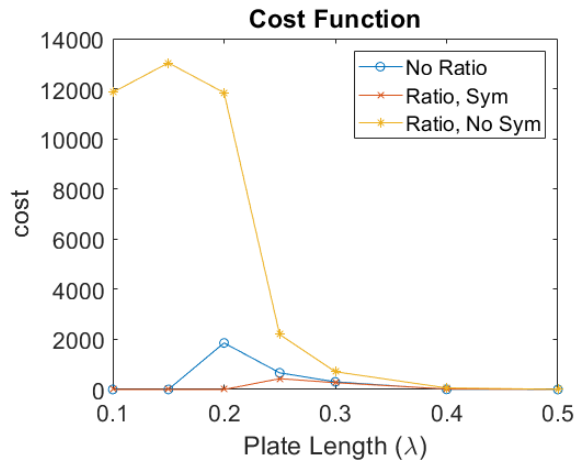


Figure 4.46: Cost function for co- and cross-polarized RCS schemes

This improvement required more optimization variables, leading to higher run times and the number of generations. The average runtime for symmetric no-ratio patterns was 5.2 hours, with an average of 37 generations. The average runtime for ratio-controlled non-symmetric patterns was 9.9 hours, with an average of 56 generations, almost double. However, these are both reasonable average runtimes and should not be a reason to favor one scheme over the other.

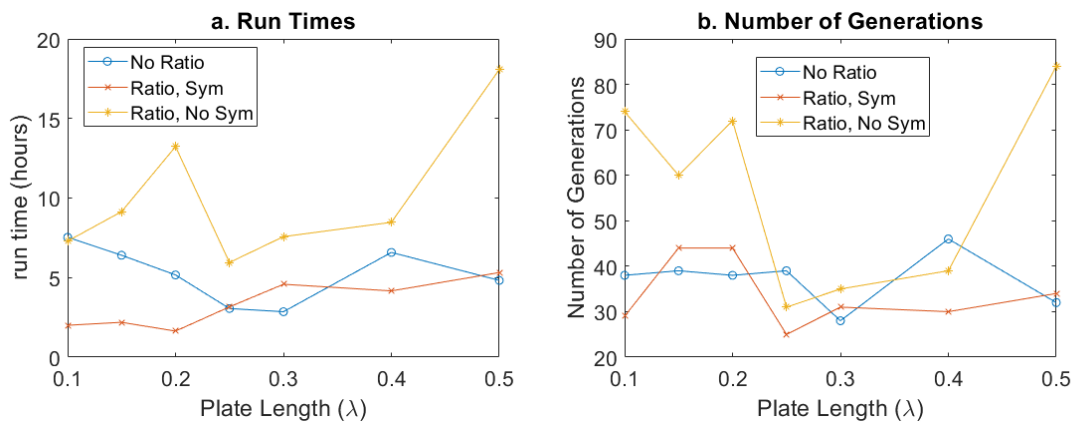


Figure 4.47: Co- and cross-polarized a. run times and b. number of generations

A concern with the non-symmetric pattern might be that the RCS is not equally radiating power in all directions. The best, $L = 0.2\lambda$, and the worst, $L = 0.5\lambda$, improvements are presented. All polarizations of the pattern are plotted below $(\sigma_{\theta\theta}, \sigma_{\theta\phi}, \sigma_{\phi\phi})$. $\sigma_{\theta\phi}$ and $\sigma_{\phi\theta}$ are same pattern, so only the one is plotted. Some interesting radiation patterns are formed. What matters, though, is that the RCS in a given direction is more likely to be greater than a non-optimized flake.

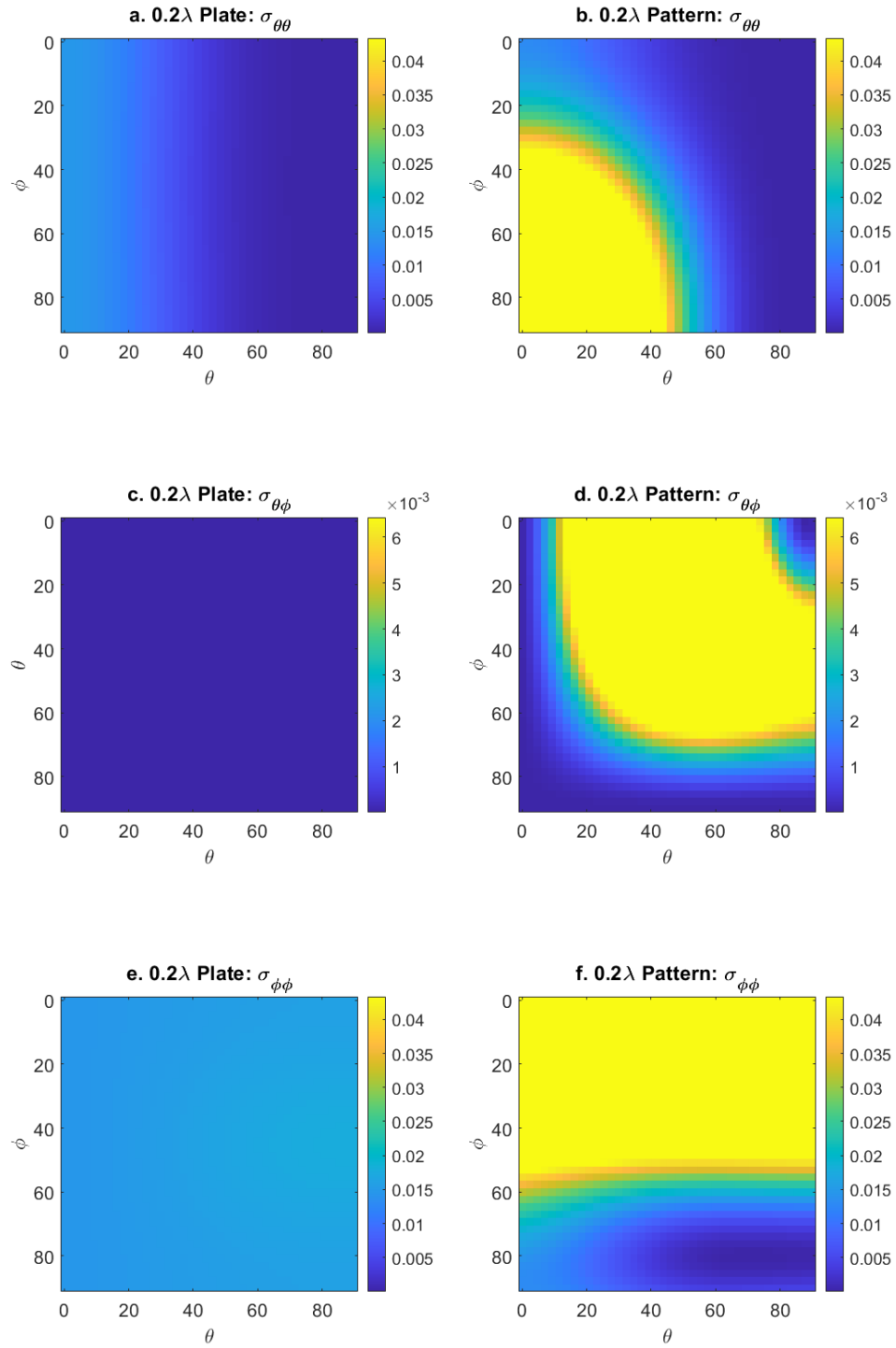


Figure 4.48: RCS for an optimized non-symmetric plate with length $L = 0.2\lambda$ a. $\sigma_{\theta\theta}$ a. $\sigma_{\theta\phi}$ a. $\sigma_{\phi\phi}$

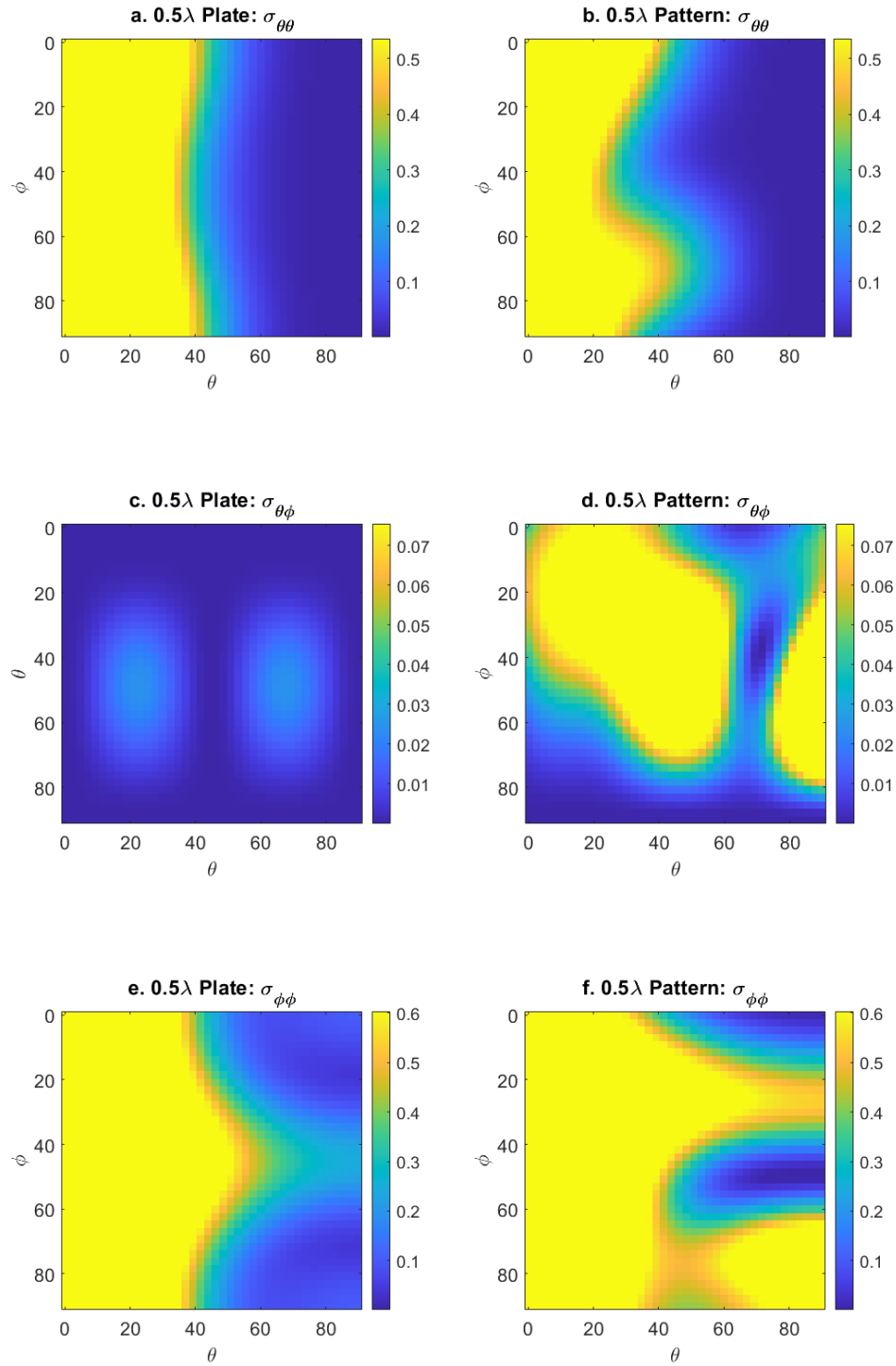


Figure 4.49: RCS for an optimized non-symmetric plate with length $L = 0.5\lambda$ a. $\sigma_{\theta\theta}$ b. $\sigma_{\theta\phi}$ c. $\sigma_{\phi\phi}$

4.3.6 Effects on Finite Conductivity on Co and Cross-polarized Backscattering Optimized Patterns

Material effects are next considered on the no-symmetry ratio-controlled patterns (figure 4.43). The impedance values from table 4.3 are once again used for the linear loss term Z_L .

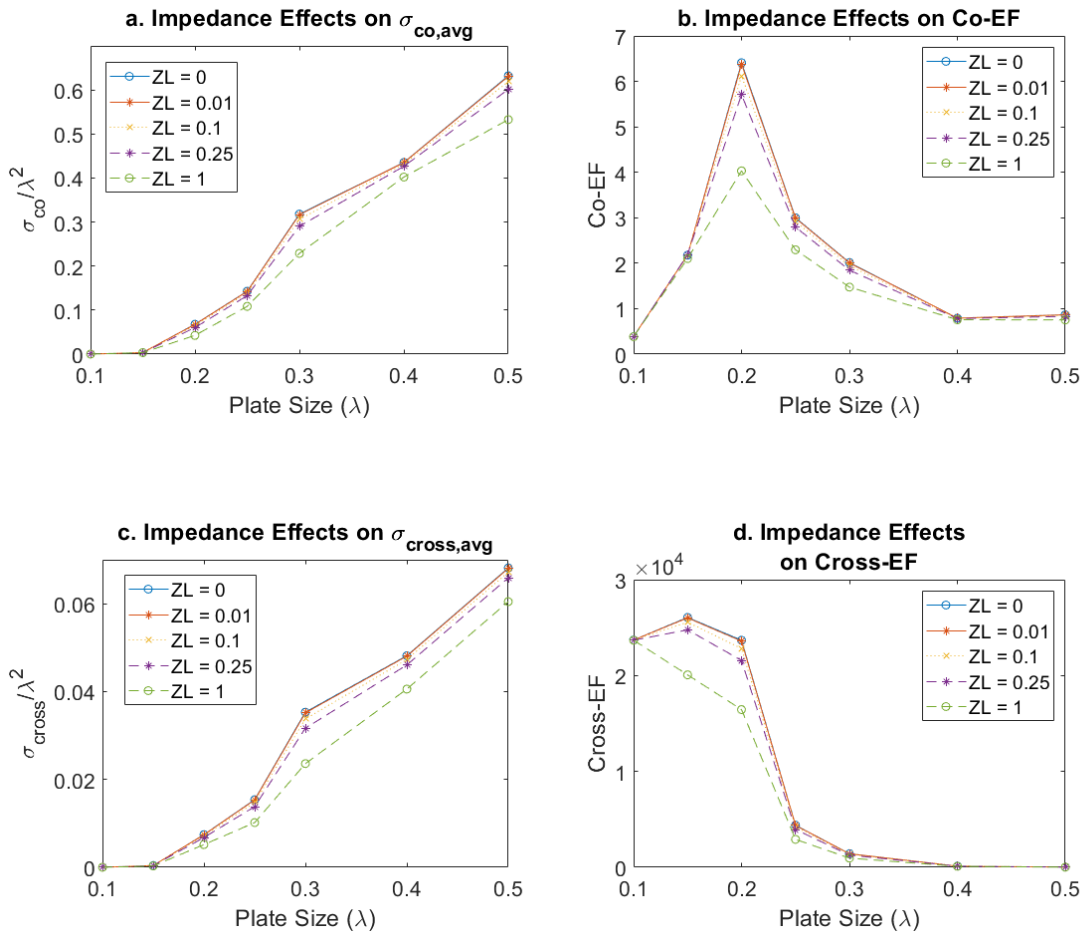


Figure 4.50 Impedance effects on a. the average σ_{co} b. co-polarized EF c. the average σ_{cross} and d. cross-polarized EF for non-symmetric plates

A similar peak seen for chapter 4's co-polarized EF (figure 4.23) once again appears. The effect of Z_L is not as drastic now because it didn't start as high. The effects on the cross-polarized EF are minimal. A decrease in performance is seen at the high improvement area, $L = 0.2\lambda$, but even in the worse case $Z_L = 1$, performance is only decreased by 20%.

4.3.7 Summary of Results for Optimizing Patterns for Co and Cross-Polarized Backscattering

The cross-polarized scattering terms have been optimized under various conditions. The final result led to unintuitive patterns that could only be found using a computational optimizer. The no-symmetry ratio solutions were the best results. Both the co- and cross-polarized scattering were improved without one overpowering the other. These no symmetry patterns were taken, and material effects were added. The effects are minimal compared to chapter 4's co-RCS optimized patterns.

4.4 Concluding Remarks

This computational chapter is rather long. A list of essential findings is reported for the ease of the reader

- A high EF was seen for plate lengths $L = 0.2\lambda$ for both optimized forward and backscattering with the same 'x' pattern emerging. I believe this is due to LC resonator-like effect. This improvement, unfortunately, quickly drops after finite conductivity is introduced.
- A typical manufacturing problem, registration error, is identified. I showed that even small control over this error can improve results.
- When set to half-wavelength at the center frequency, the multi-frequency designs for both forward and backscattering returned ring resonator-like

designs. This helps build trust that the optimization algorithm works because it produces well-studied designs.

- The multi-frequency designs that attempt to capitalize on the high EF seen at $L = 0.2\lambda$ somewhat worked. There is a slight decrease in performance compared to the half-wavelength patterns, but generally, single-particle performance is not used in real-world applications. By decreasing the area, more particles could be packed into a single cartridge leading to an overall improvement of a particle cloud. However, further research must be completed to examine this region's material effects. As stated before, EF decreases once finite conductivity is introduced in this region.
- For optimizing co- and cross-polarized backscattering, removing the plate symmetry requirement is essential. I initially assumed the symmetry to decrease computational time with the idea that this forces the monostatic to be spread evenly in all directions. Non-optimal results occur with this assumption after introducing the cross-polarized term. Removing this assumption creates interesting scattering patterns. However, the optimized design is still more likely to return a higher monostatic RCS than a non-optimized plate of similar size.

Chapter 5

EXPERIMENTAL VALIDATION

In this chapter, I will discuss the experimental methods used as a validation study for the design codes developed in this research. It should be clearly noted that the experimental work was a joint effort from several researchers in my laboratory. In particular, Mr. Tom Lum designed and fabricated the particle cloud chamber discussed in section 5.2. Mr. Michael Richards developed the testing and calibration procedures as well as the associated software interface that was used to conduct testing of the patterned particles. He also performed detailed metrology on the printed particles. I wish to acknowledge and thank them both for their contributions to this work.

In section 5.1, I will discuss the fabrication of the printed chaff materials and metrology results. Section 5.2 explores the particle cloud test chamber designed and constructed to measure scattering from a cloud of suspended particles. Section 5.3 compares the experimental results with predicted results from this dissertation's computational models.

5.1 Fabrication of Patterned Particles

From the computational results provided in chapter 4, it was decided to focus on one of the designs for experimental validation. In particular, I focused on the optimal patterned design that assumed no particle registration (see chapter 4, section 4.1.2). Since pattern registration is a particular problem during fabrication, it was decided that this design would be the most robust. This design was sent to Molex

Corporation, which printed and “singulated” the particles for testing. Molex’s fabrication process uses a rotary screen printer to create large sheets containing arrays of particles. Individual particles are then singulated from the sheet using rotary die cutters. As mentioned previously, the cutting is non-exact and has registration errors, as discussed in chapter 4. In addition to the patterned particles, Molex also provided fully metalized, or flooded, particles of the same size that used the same conductive ink. These particles provided a convenient method for conducting an apples-to-apples comparison. The size of both the patterned and fully flooded particles was chosen to be 3mm x 3 mm and optimized for maximum scattering at 35GHz. Images of both the patterned and fully flooded particles can be seen in figures 5.1 and 5.2.

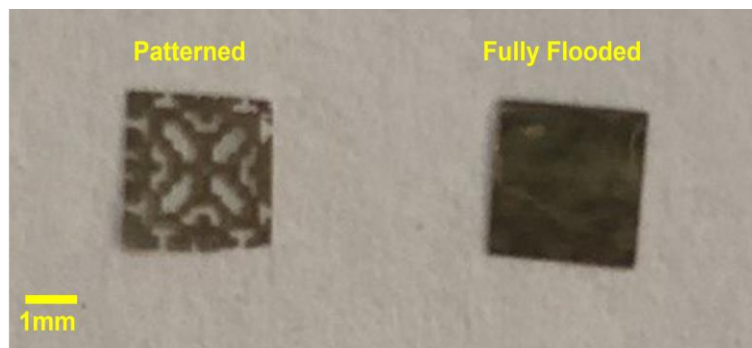


Figure 5.1: Pattern and fully flooded flakes

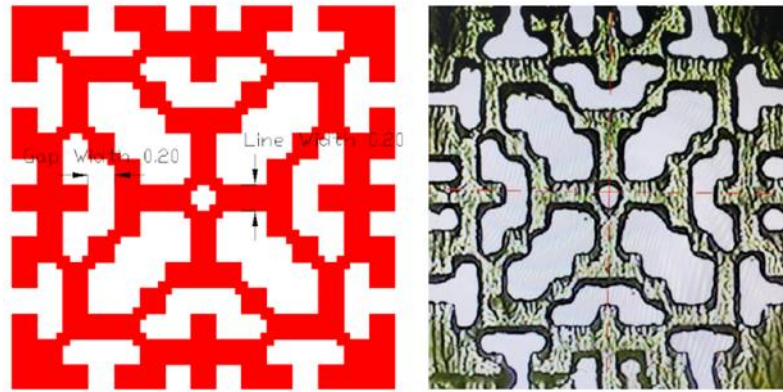


Figure 5.2: Printed chaff particle optimized for maximum scattering return assuming no registration

5.2 Metrology Results

Detailed metrology was conducted on the printed particles to determine the feature size and thickness of the metal coating. A Keyence VK-3000 laser confocal microscope, shown in figure 5.3, was used for these measurements. On the top row of the left side of figure 5.3 are microscope images of two different particles. These images clearly show the registration errors that cause a variation in the pattern from particle-to-particle. This type of error motivated me to choose the design that assumed no pattern registration.

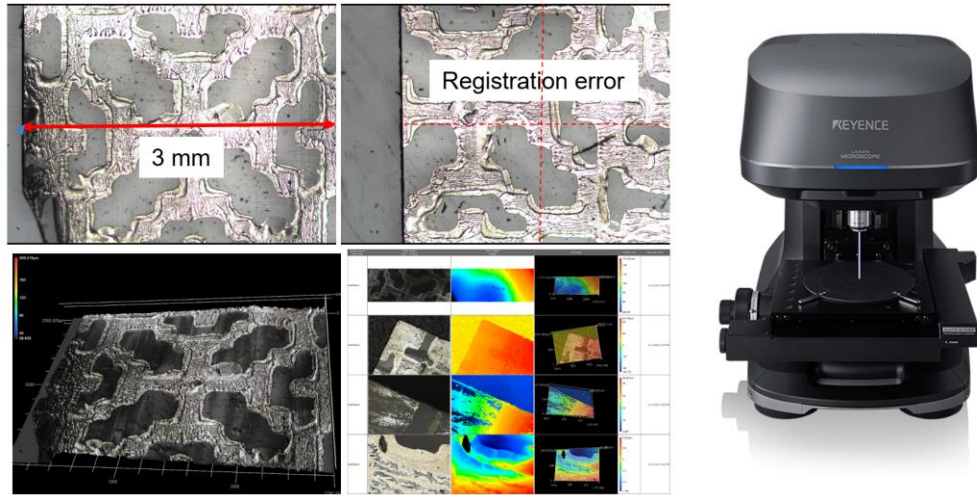


Figure 5.3: Registration error visible using Keyence VK-3000 laser confocal system.

To measure the thickness of the printed metallic inks, the VK-3000 was also used. Figure 5.4 provides an example of the data captured from the VK-3000, showing both the roughness of the metallic layer and the edge thickness.

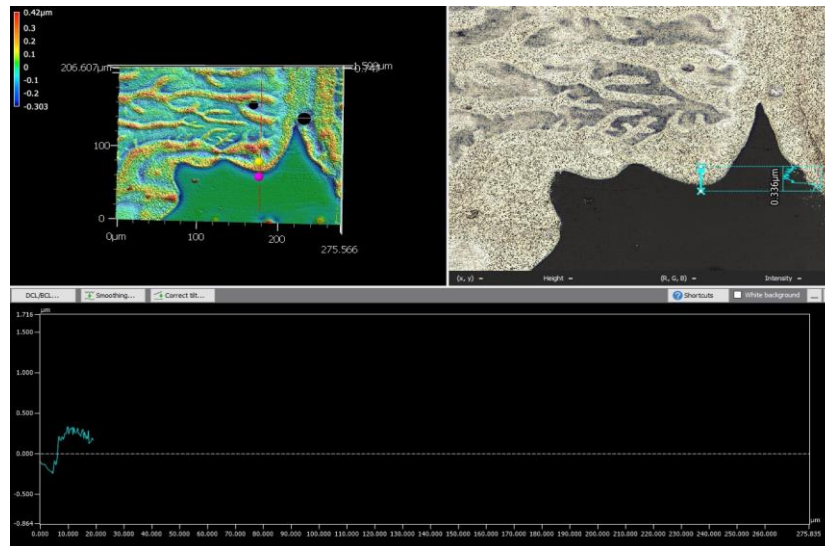


Figure 5.4: Patterned chaff test particle 1 at 50 times zoom for Thickness measurement

Data was collected from a random set of chaff particles at various locations on each particle. The data collected showed the average metal thickness to be approximately ~1.0 microns. Based on the measured average metal coating thickness, calculations were performed to determine the electrical thickness of the layer in terms of skin depth. A skin depth of δ , would indicate a distance in which the wave's amplitude has decreased by $1/e$ or 37% of its value at the surface. For conductive surfaces, it is desirable that the thickness is multiple skin depths to prevent transmission of energy through the metallic surface. These particle's skin depth was calculated based on the assumption that the metallic ink qualified as a good conductor, leading to the formula below being utilized.

$$\delta \approx \sqrt{\frac{2}{\omega\mu\sigma}} \quad (5.1)$$

where, ω , denotes the angular frequency, σ , denotes the electrical conductivity of the metal and μ is the magnetic permeability. Figure 5.5 plots the skin depth versus conductivity at 35 GHz. Also shown on the plot is the measured average thickness of the chaff particles described above. The result indicates that the metal printed on the particle would need a conductivity of 7×10^6 S/m for the skin depth to be one micron. Based on data provided by the vendor, Molex, the printed metallic ink's conductivity is approximately 10^7 S/m. At this conductivity, the metallic thickness is slightly larger than one skin depth; however, less than a desirable thickness of 4 to 5 skin depths. This could lead to performance issues in the chaff cloud as described in chapter 4, section 4.1.5.

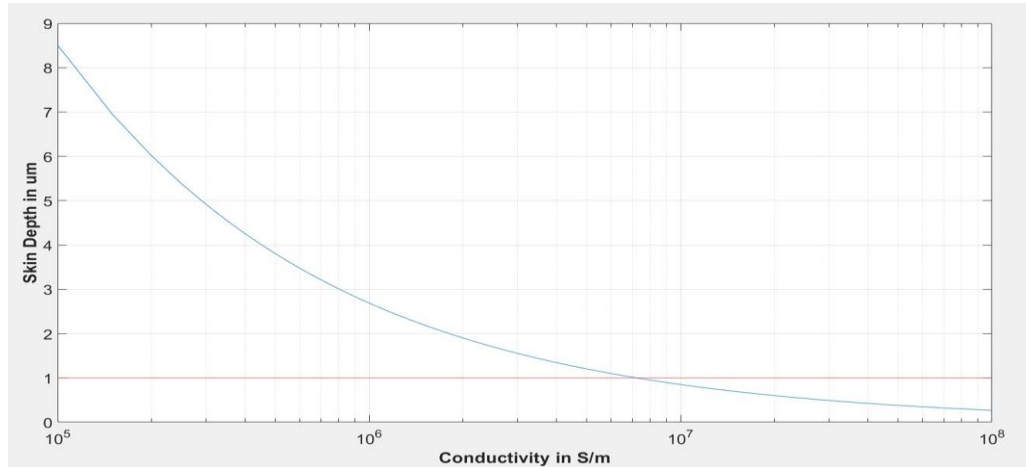


Figure 5.5: Skin depth at 35 GHz as a function of metal conductivity. Solid red line indicates the measured average thickness of the printed metal chaff.

Another critical aspect of the particles that was examined was the surface roughness of the metal. Using the VK-3000, the particles were found to have a vein-type structure, with high levels of variance between peaks and valleys (see figures 5.6 and 5.7). Average surface roughness of 0.9 microns in height variance was measured, which is significant when compared to the average metal thickness of the particles. However, the effect of this surface roughness on the scattering performance of the particles was not evaluated. The MoM code that was developed for this project assumed a smooth conductive surface. Future studies should be conducted to assess these fabrication errors more fully.

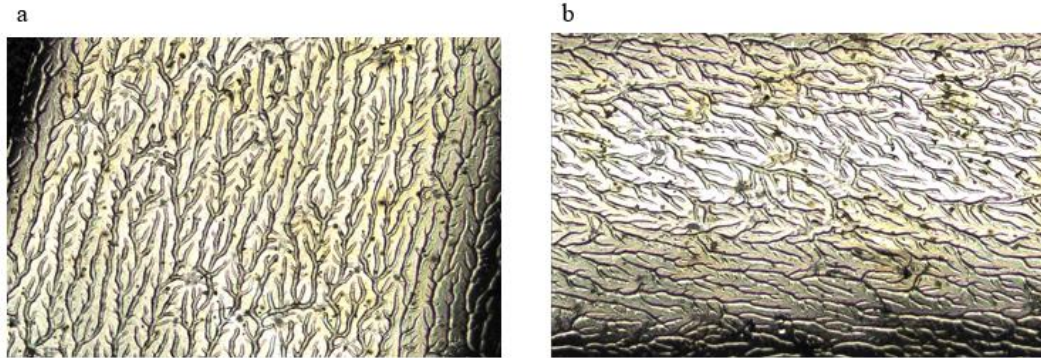


Figure 5.6: Fully flooded chaff particles at 5 times zoom showing the surface roughness of the printed metal materials a. and b. show two different chaff particles

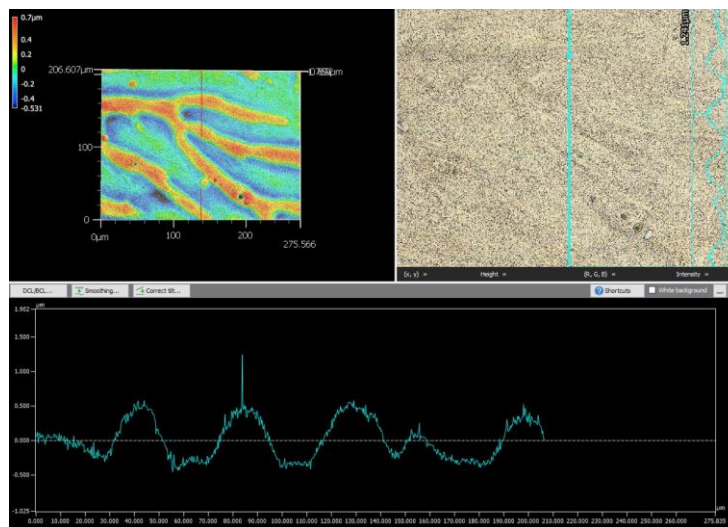


Figure 5.7: Roughness profile of chaff test particle

5.3 Particle Cloud Chamber

A particle chamber was designed and constructed to measure the scattering from a cloud of small particles directly. As mentioned earlier, Mr. Tom Lum designed and fabricated this system. The system was designed to create a suspension of particles in which the RF transmission through them could be measured using a free-space focused beam system (see Figure 5.8 and 5.9).

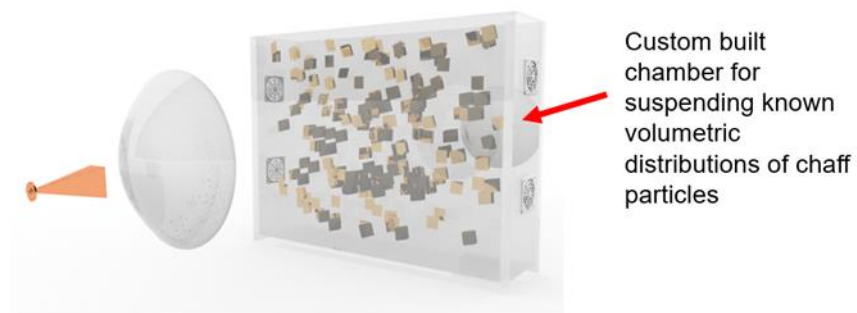


Figure 5.8: Experimental setup for measuring RCS of chaff particles. Particles are suspended in a random uniform distribution using fans.

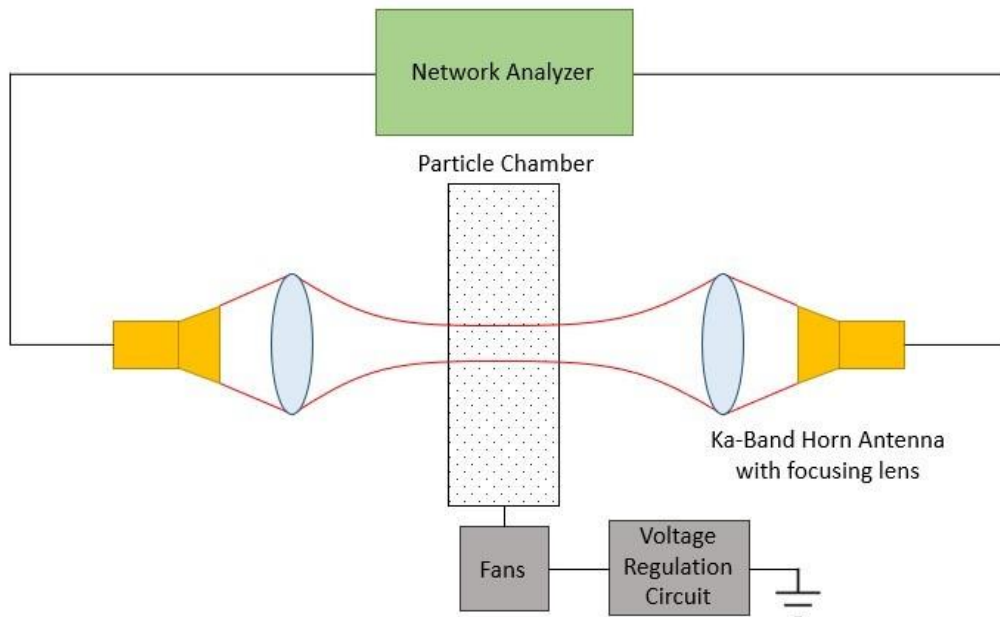


Figure 5.9: Diagram of particle chamber. Particles are suspended in a random distribution in the particle chamber. Horn antennas are connected to a network analyzer to measure S-parameters.

The concept is that the two lensed antennas are used to create a Gaussian beam that would be transmitted through a chamber in the middle between the two antennas. Within the chamber, particles would be suspended to create a random distribution or particle cloud. A high-frequency network analyzer is used to measure the transmission of RF energy through the chamber over a wide band of frequencies. The measured transmission is directly related to the RCS in the forward scattering direction. The number of particles can be varied between tests to measure transmission, or more specifically extinction, as a function of particle density.

The particle cloud chamber is shown in Figure 5.10. This system is 60" tall and 5" thick. A fixed amount of chaff particles are inserted at the bottom of the chamber, where various screen filters hold them in place. A set of blower fans are then controlled to suspend the particles within the center of the chamber. The free-space-focused beam system is then used to measure transmission (for assessing extinction coefficients) or reflection (for monostatic RCS) through the cloud of particles over a broad range of frequencies. The measurement is then repeated with various amounts of particle density (particles/m²) to assess their scattering properties and compare those results to numerical predictions. An example of a measurement is shown in Figure 5.11.

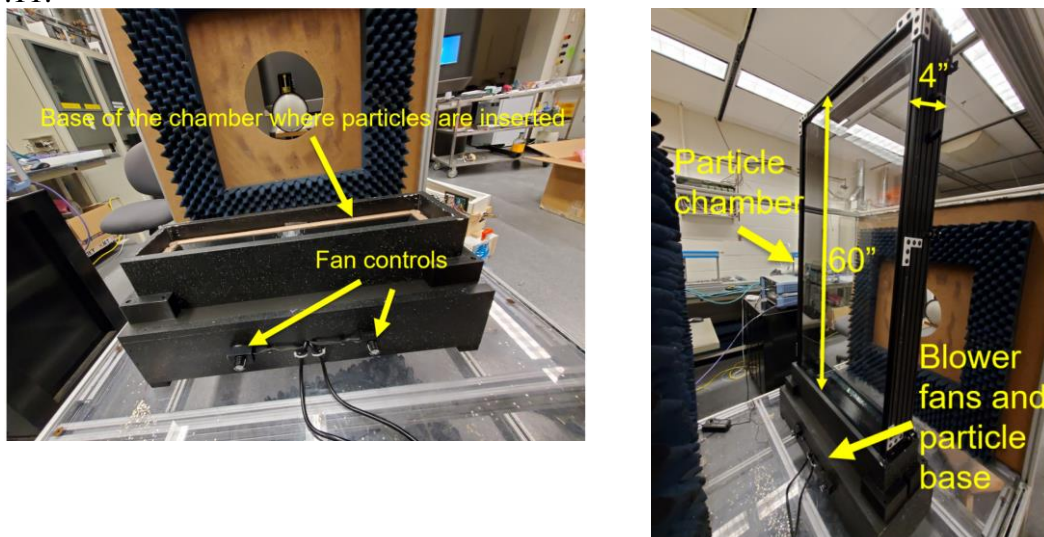


Figure 5.10: Experimental setup for measuring RCS of chaff particles. Three independently controlled blower fans are used for suspending particles in space during RF testing

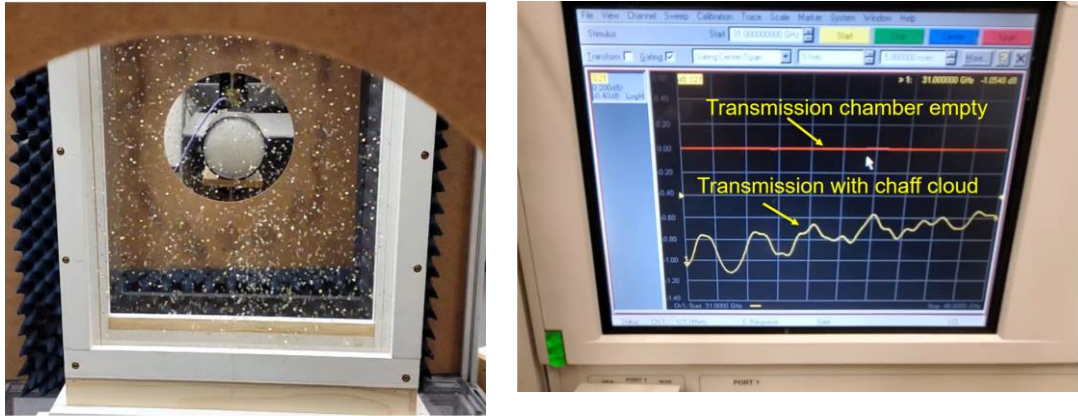


Figure 5.11: Images of chaff cloud chamber suspending particles during a test and the transmission results on the VNA.

5.4 Experimental Results

A set of experiments were conducted by Mr. Michael Richards and used to compare the experimental to the models developed in this thesis. The chaff cloud chamber was used to evaluate the transmission of RF energy from 26 GHz to 40 GHz for both patterned and fully flooded chaff particles. The particle concentration for both particle types was set by varying the amount of particles, determined by weight, placed in the chamber bottom. Specifically, the total particle weight was varied from 0.25 grams to 2.0 grams in steps of 0.25 grams (see figure 5.12).

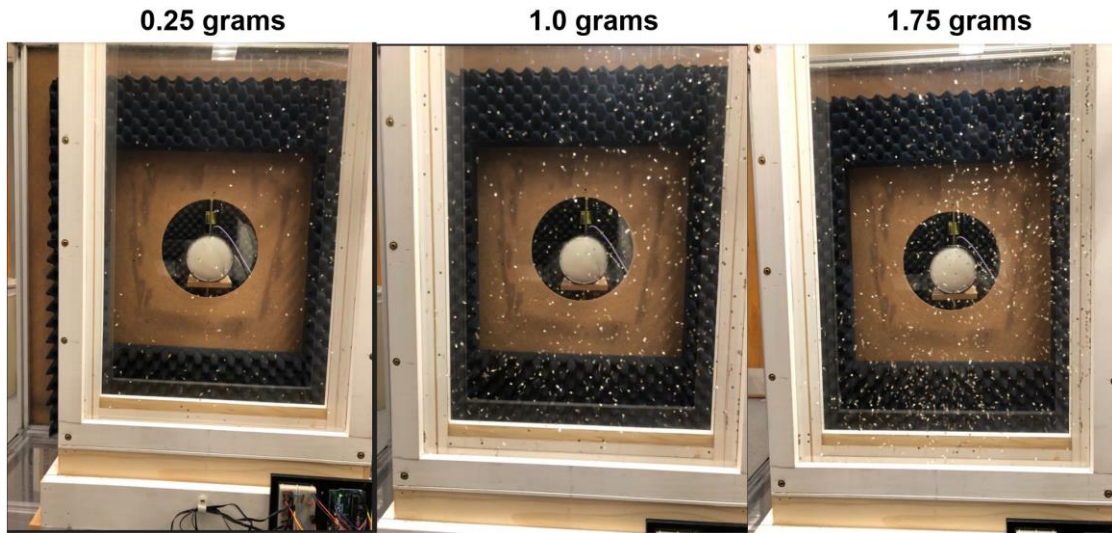


Figure 5.12: Images of chaff cloud chamber suspending particles during a test. The total weight of chaff particles placed in the system varied from 0.25 grams to 1.75 grams to demonstrate how various concentration of particles can be suspended.

In figure 5.13, the transmission magnitude in dB is displayed in a color plot as a function of frequency (x-axis) and time (y-axis). The figures show a high transmission approach 100% for the experiment's first 10 to 15 seconds. This is due to the time the system takes to suspend a uniform distribution of particles within the chamber fully. After this time, the transmission magnitude is roughly independent of measurement time from 10-45 seconds. There is, however, a significant and expected variation with both frequency and particle concentration. The higher frequencies tend to have a high degree of scattering and the extinction coefficient also increases as the concentration increases. Both effects are entirely expected and match our numerical predictions.

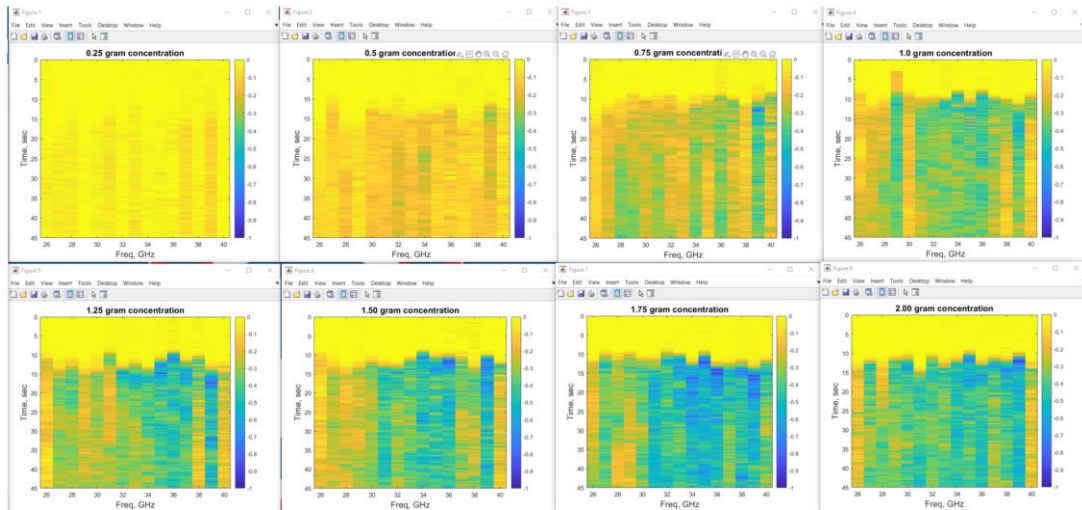


Figure 5.13: Results for fully flooded chaff particles (3 mm x 3mm in dimensions). Measurements were conducted from 26 GHz to 40 GHz over a 45 second time frame. Here the transmission magnitude in dB is displayed in a color plot as a function of frequency (x-axis) and time (y-axis). The yellow portion indicates a high level of transmission (i.e., small degree of scattering) while the blue regions indicate increased scattering. The different plots are experiments on the same particles but increasing concentrations.

Figure 5.14 shows a comparison of transmission for fully flooded and patterned particles. Here the particle weight was the same for both tests (i.e., 1.5 grams). The bottom two plots in the figure provide a time-averaged transmission in dB over the time frame in which the particles are fully suspended (i.e., 15 to 45 seconds) as a function of frequency. It is clear from these plots that the transmission from the patterned flake is measurably below that of the fully flooded. This would indicate a higher degree of scattering and, thus, a higher extinction coefficient for the optimized pattern. To better quantify this the experimental data is listed in a table below where

the magnitude of the transmission coefficient (S21) is given on a linear scale for both the fully flooded and patterned tests at different frequencies.

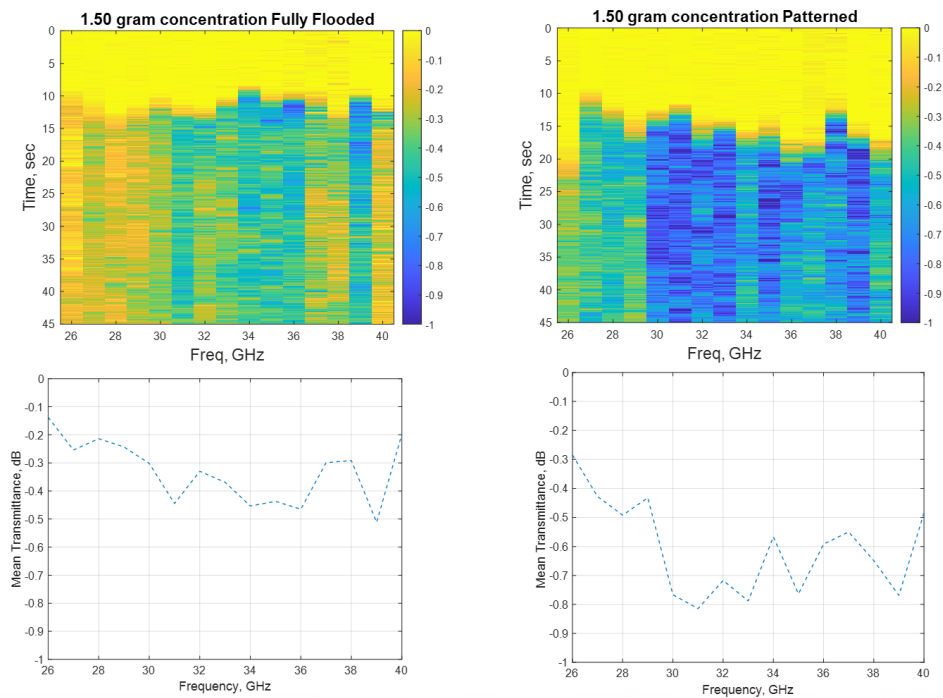


Figure 5.14. Transmission results for fully flooded chaff particles (3 mm x 3mm in dimensions) versus patterned particles of the same size. For these experiments the same concentration of both particles was used. Also shown are plots of the mean transmission averaged over the time frame of 15 to 45 seconds.

Table 5.1: Measured abs(S21) for both fully flooded and patterned particles

Frequency, GHz	Fully Flooded abs(S21)	Patterned abs(S21)
26	0.9661	0.933
28	0.9528	0.8933
30	0.933	0.8414
32	0.9279	0.8472
34	0.9016	0.8760

35	0.9057	0.8414
36	0.9016	0.8710

In the next section this data is compared to predictions from the cloud model.

5.5 Comparison of Experimental Results to Computational Predictions

As discussed in chapter 2, when looking at particles in a cloud, the average RCS of a single particle can be used, assuming the particles are non-interacting. If the number of particles relative to the cloud is small, then coupling effects can be ignored [29,30]. This can be extended into larger particle densities. When an incident field approaches a cloud of particles, the total scattering can be divided into coherent scattering and incoherent scattering of the particles.

As discussed in chapter 2 the coherent term of the RCS dominates in forward scattering [32]. The average RCS considering only the coherent component is thus given by

$$\sigma_{coh} = N^2 \frac{1}{4\pi} \int_0^{2\pi} d\Phi \int_0^\pi \sigma(\Theta, \Phi) \sin\Theta d\Theta \quad (5.2)$$

where $\sigma(\Theta, \Phi)$ is the RCS of a single particle oriented at an angle (Θ, Φ) and N is the number of particles. The enhancement factor EF, discussed in chapter 4, is used to compare improvement against a fully flooded, non-patterned particle to normalize the measured and simulated results. This is given mathematically as

$$EF = \frac{\sigma_{pattern}^{cloud}}{\sigma_{plate}^{cloud}} = \frac{\int_0^{2\pi} d\Phi \int_0^\pi \sigma_{pattern}^{particle}(\Theta, \Phi) \sin\Theta d\Theta}{\int_0^{2\pi} d\Phi \int_0^\pi \sigma_{plate}^{particle}(\Theta, \Phi) \sin\Theta d\Theta} \quad (5.3)$$

The experimental data reported transmission (S21) not RCS. However, RCS can be obtained from this data using the well-known radar range equation. Consider a

transmitting radar. P_s is supplied to an antenna with G gain. The transmitting antenna sends a signal out R distance. The wave encounters a scattering object with RCS σ and returns to a receiving antenna also a distance R away. The power received P_r can be written as

$$P_r = \frac{P_s G \lambda^2}{(4\pi)^3 R^4} \sigma \quad (5.4)$$

The received power can be written in terms of S21 as

$$P_r = 1 - |S_{21}|^2 \quad (5.5)$$

Comparing the patterned particles to the fully flooded ones, the EF can be written in terms of the power received as

$$EF = \frac{\sigma_{pattern}^{cloud}}{\sigma_{plate}^{cloud}} = \frac{P_r^{pattern}}{P_r^{plate}} \quad (5.6)$$

The EF, given in equation 5.9, was calculated for both the measured and simulated data using the above schemes. The mean and median are given over the entire frequency sweep. The results can be seen in the Table 2.

Table 5.2: EF of measured and computational prediction of patterned particles

Frequency, GHz	Measured EF	Predicted EF	Percent Diff (%)
26	1.93	1.85	4.23
28	2.19	2.06	6.12
30	2.26	2.20	2.69
32	2.03	2.15	5.74
34	1.24	1.89	41.53
35	1.63	1.67	2.42
36	1.29	1.54	17.67
mean	1.80	1.91	5.93
median	1.93	1.89	2.09

The results presented in Table 5.2 do validate that the patterned particles demonstrate enhanced scattering over a fully flooded particle. This is even true when the particles are electrically small. The degree of enhancement is also consistent with the predicted values (i.e., approximately a two-fold increase). However, there are some deviations between measured and expected results at various frequency values, with percent errors ranging from 1% to 40%. However, the mean error between the measured and predicted EF is 5.93%. This is an excellent agreement and validates the computational models and results in chapter 4.

5.6 Conclusion

In this chapter, I presented an experimental system and results that were used to validate my computational model and optimized particle results. To this end, a particle cloud chamber was developed that was used to suspend a cloud of particles within a free-space focus beam system. This system measured transmission or extinction through a cloud of particles as a function of frequency and particle density. The particles were designed to have approximately a two-fold improvement in scattering over a fully flooded particle. A comparison of the measured results to predictions showed reasonably good agreement with an average percent error of 11.4%.

Chapter 6

CONCLUSION AND FUTURE WORKS

This chapter seeks to summarize the work of this dissertation and provide concluding remarks about possible continuing work. This dissertation's focus was a study of scattering effects from small meta-surface particles (patterned particles). Current commercial software tools are not well suited for this problem. This dissertation developed custom software to fill this gap.

Chapter 2 provided the necessary background in computational electromagnetics needed for this work. Different computational EM approaches were discussed, with MoM being the best approach for PEC scattering problems. MoM discretizes the EFIE to solve for the surface currents. All other necessary values (RCS, C_{ext}) derive from the surface current, so the problem is fully solved. The impedance sheet approximation modifies the EFIE with a linear term to allow material effects to be studied.

The method of moments is then applied to a square PEC plate in chapter 3 and implemented in MATLAB. Matrix manipulation (removing rows or columns) of the impedance matrix creates different patterns from the original non-patterned plate. An average solution of a vast number of incident waves can then be solved with simple matrix multiplication. At no point is a new impedance matrix found, which significantly speeds the optimization process. Well-known optimizers (particle swarm, genetic algorithm, pattern search) take the average and find the best pattern. The

custom software generates solutions much faster than commercial (COMSOL, HFSS, FEKO.)

Chapter 4 presented the computational results. It began by focusing on maximizing the backscattering through the monostatic RCS. The cross-polarized $\sigma_{\theta\phi}, \sigma_{\phi\theta}$ terms are much smaller than the co-polarized $\sigma_{\theta\theta}, \sigma_{\phi\phi}$, so were discarded. The average monostatic RCS was therefore composed only of the co-polarized $\sigma_{\theta\theta}, \sigma_{\phi\phi}$. Plate lengths L chosen are with respect to wavelength λ wherever possible to allow for frequency-independent results. The findings are summarized as

- The optimized single frequency pattern discovered a high EF at $L = 0.2\lambda$. This x-pattern was seen multiple times throughout the thesis. I believe it achieves high radiation due to acting as an LC-resonator that other groups have found with similar patterns. This improvement is unfortunately lost after material properties are introduced and impedance increases.
- As expected, at $L = 0.5\lambda$ particles were the least successful at finding a better-optimized pattern relative to a full PEC plate than other plate lengths. This length is already the optimal plate length for the full PEC plate. Still, an EF of 1.2 was achieved.
- A manufacturing error with cutting registration was identified. This means the code had to be modified to consider this. With no control, optimized patterns were still successfully able to improve a full PEC plate. However, this error could lead to results as bad EF = 1.1. Being able to control the cutting registration by a small amount saw this minimum increase to EF = 1.56. I note the software appears to resolve this by placing a metalized border around the particle around the area a person is most likely to cut.

- A multi-frequency response is investigated. I had hoped that the high EF seen at $L = 0.2\lambda$ could be capitalized upon. The first plate length was chosen to be half wavelength at the center frequency, a more traditional design. The optimizer found a ring resonator-like pattern which matched the expected results. These are well-known designs used for multi-frequency operations. The next plate length was then set so that over the range, each frequency's corresponding plate length would vary between $L = [0.27\lambda, 0.5\lambda]$. Slightly decreased average EF was found (EF = 1.14 vs EF = 1.2). This scheme took significantly more time as well. However, this is a possible pattern if the size is a limiting factor.

Minimizing forward scattering was next investigated. The extinction cross-section C_{ext} was shown to capture both absorption and scattering effects that lead the minimization. Unintuitively, this means the extinction coefficient C_{ext} must be maximized. Again, the co-polarized terms are much larger than the cross-polarized ones, so they are disregarded in the average. Results found are

- The same general graph for EF was found for forward scattering improvement as backscattering at a lower order magnitude. A high peak is seen at $L = 0.2\lambda$. The optimized pattern is also the same x-pattern as seen before. Introducing material properties once again decreases the improvement.
- The optimized forward scattering patterns are not always the optimized backscattering patterns.
- The same multi-frequency scheme was attempted as backscattering over a frequency range 7-13 GHz. This aims to maximize scattering effects for the smallest possible particle.

- One particle had a length of $L = 0.5\lambda$ at the center frequency or 1.5 cm. A ring resonator like design once again emerged. The EF improved by 7%.
- Another particle had a length that varied between $L = [0.27\lambda, 0.5\lambda]$ over the frequency range or 1.15 cm. The EF improved by 13%, however, is not improved over the entire frequency range. A non-patterned flake has higher average scattering than the optimized pattern starting at 11GHz.

The cross-polarized term for backscattering was finally considered next. This introduced a problem. Using a simple average of all terms, $\sigma_{\theta\theta}$, $\sigma_{\theta\phi}$, $\sigma_{\phi\theta}$, $\sigma_{\phi\phi}$, will not work. The cross-polarized terms are orders of magnitude smaller. Instead, improvement is averaged. The co-polarized EF and cross-polarized EF are averaged together. Three different schemes were attempted with this process 1) plate symmetry seen in previous chapters is enforced, 2) the plate symmetry is enforced, but now the EFs are forced to remain within a ratio, and 3) the plate symmetry is removed, and the EF ratio is enforced. I found

- The third scheme worked the best. One EF could overpower the other by not forcing a ratio, leading to unequal scattering improvement. Requiring symmetry with the ratio control, the optimizer essential found no solution. Improvement is seen equally in both the cross- and co-polarized monostatic RCS with these requirements.
- An important note from the symmetry with no ratio control is that an x-pattern similar to the co-polarized optimization in chapter 4 emerges again.
- The impedance effects were not as drastic as on the maximized backscattering in chapter 4. The peak at $L = 0.2\lambda$ for cross- and co-polarized EF does decrease, but not as drastically.

Chapter 5 concludes with the experimental validation. The no-registration designs were fabricated and then measured as a particle cloud. This means that a particle model must be implemented for the computational model. Spherical particle clouds have been well studied, so this model was used. This gives the RCS of the entire cloud based on a single particle. The available data gives S_{21} not RCS. The EF of a fully flooded flake vs the optimized pattern must be taken where the computational model uses monostatic RCS, and the experimental data uses transmitted power. The model was validated over a frequency range with strange errors appearing at higher frequencies. Further investigation is required to determine if it is a computational error or experimental.

Optimization algorithms are applied to a new area of interest by implementing custom software, scattering from patterned particles. My work solely focused on single flat particles. Continued research should expand on other 3-D shapes (cubes, spheres, etc). Another consideration is real-world scenarios. Particles are stored in a cartridge and then released. Smaller particle lengths lead to a higher number in a single cartridge. The high improvement seen around a plate length of $L = 0.2\lambda$ could lead to improvement over other particle sizes. However, the material study showed impedance significantly diminished the EF. Manufacturing the optimized patterns $L < 0.5\lambda$ and measuring their properties, such as flake thickness and scattering effects, could allow improved computational modeling. A final consideration is if the number of particles in the cartridges increases, the particle cloud will be higher density. An assumption made in this research is that the particles were enough apart that no coupling effects occurred. As the number of particles increases, this is no longer the case. Further research is required.

REFERENCES

1. J. B. Pendry, A. J. Holden, D. J. Robbins, and W. J. Stewart, "Magnetism from conductors and enhanced nonlinear phenomena," *IEEE Transactions on Microwave Theory and Techniques*, vol. 47, no. 11, pp. 2075–2084, 1999, doi: [10.1109/22.798002](https://doi.org/10.1109/22.798002).
2. D. R. Smith, W. J. Padilla, D. C. Vier, S. C. Nemat-Nasser, and S. Schultz, "Composite Medium with Simultaneously Negative Permeability and Permittivity," *Physical Review Letters*, vol. 84, no. 18, pp. 4184–4187, May 2000, doi: [10.1103/physrevlett.84.4184](https://doi.org/10.1103/physrevlett.84.4184).
3. T. Vandervelde, "Beyond invisibility: engineering light with metamaterials," *The Conversation*. <https://theconversation.com/beyond-invisibility-engineering-light-with-metamaterials-54632> (accessed Aug. 15, 2022).
4. R. W. Ziolkowski, "Passive and active metamaterial constructs and their impact on electrically small radiating and scattering systems," *IEEE Xplore*, pp. 1–4, Aug. 2011, doi: [10.1109/URSIGASS.2011.6050490](https://doi.org/10.1109/URSIGASS.2011.6050490).
5. Z. Wang, S. Liu, and Y. Dong, "Electrically Small, Low-Q, Wide Beam-Width, Circularly Polarized, Hybrid Magnetic Dipole Antenna for RFID Application," *IEEE Transactions on Antennas and Propagation*, vol. 69, no. 10, pp. 6284–6293, Oct. 2021, doi: [10.1109/TAP.2021.3070236](https://doi.org/10.1109/TAP.2021.3070236).
6. F. Bilotti, S. Tricarico, and L. Vegni, "Electromagnetic cloaking devices for TE and TM polarizations," *New Journal of Physics*, vol. 10, no. 11, p. 115035, Nov. 2008, doi: [10.1088/1367-2630/10/11/115035](https://doi.org/10.1088/1367-2630/10/11/115035).
7. C. A. Balanis, *Antenna theory analysis and design*. Hoboken, New Jersey Wiley, 2016.
8. A. Hamza and H. Attia, "Fast Beam Steering and Null Placement in an Adaptive Circular Antenna Array," *IEEE Antennas and Wireless Propagation Letters*, vol. 19, no. 9, pp. 1561–1565, Sep. 2020, doi: [10.1109/LAWP.2020.3009905](https://doi.org/10.1109/LAWP.2020.3009905).
9. A. Recioui and A. Azrar, "Use of genetic algorithms in linear and planar antenna array synthesis based on Schelkunoff method," *Microwave and Optical Technology Letters*, vol. 49, no. 7, pp. 1619–1623, 2007, doi: [10.1002/mop.22510](https://doi.org/10.1002/mop.22510).

10. A. Hamza, K. K. Qureshi, S. I. Sheikh, and H. Attia, "Linear and Planar Antenna Array Nulling based on Schelkunoff Polynomial and Genetic Algorithm," *IEEE Xplore*, Jan. 01, 2020.
<https://ieeexplore.ieee.org/abstract/document/9050021> (accessed Oct. 28, 2022).
11. J. Fondevila-Gomez, J. A. Rodriguez, F. Ares, and E. Moreno, "A Simple Way of Obtaining Optimized Patterns using the Woodward-Lawson Method," *IEEE Xplore*, Jul. 01, 2006.
<https://ieeexplore.ieee.org/abstract/document/1711340> (accessed Oct. 28, 2022).
12. S. Reza and C. G. Chrostodulou, "Beam shaping with antenna arrays using neural networks," *IEEE Xplore*, Apr. 01, 1998.
<https://ieeexplore.ieee.org/abstract/document/673333> (accessed Oct. 28, 2022).
13. J. M. Cid, J. A. Rodriguez, and F. Ares, "Shaped Power Patterns Produced By Equispaced Linear Arrays: Optimized Synthesis Using Orthogonal $\sin(Nx)/\sin(x)$ Beams," *Journal of Electromagnetic Waves and Applications*, vol. 13, no. 7, pp. 985–992, Jan. 1999, doi: [10.1163/156939399x00466](https://doi.org/10.1163/156939399x00466).
14. M. Kim, A. M. H. Wong, and G. V. Eleftheriades, "Optical Huygens' Metasurfaces with Independent Control of the Magnitude and Phase of the Local Reflection Coefficients," *Physical Review X*, vol. 4, no. 4, Dec. 2014, doi: [10.1103/physrevx.4.041042](https://doi.org/10.1103/physrevx.4.041042).
15. T. Pochiraju and V. Fusco, "Amplitude and Phase Controlled Reflectarray Element Based on an Impedance Transformation Unit," *IEEE Transactions on Antennas and Propagation*, vol. 57, no. 12, pp. 3821–3826, Dec. 2009, doi: [10.1109/TAP.2009.2026596](https://doi.org/10.1109/TAP.2009.2026596).
16. M. Ohira, H. Deguchi, M. Tsuji, and H. Shigesawa, "Multiband single-layer frequency selective surface designed by combination of genetic algorithm and geometry-refinement technique," *IEEE Transactions on Antennas and Propagation*, vol. 52, no. 11, pp. 2925–2931, Nov. 2004, doi: [10.1109/TAP.2004.835289](https://doi.org/10.1109/TAP.2004.835289).
17. A. Alakhras and D. A. McNamara, "The shape synthesis of 3D electrically-small conducting surface antennas," *Electronics Letters*, vol. 57, no. 8, pp. 311–313, Mar. 2021, doi: [10.1049/ell2.12078](https://doi.org/10.1049/ell2.12078).

18. R. W. Ziolkowski, P. Jin, and C.-C. Lin, "Metamaterial-Inspired Engineering of Antennas," *Proceedings of the IEEE*, vol. 99, no. 10, pp. 1720–1731, Oct. 2011, doi: [10.1109/JPROC.2010.2091610](https://doi.org/10.1109/JPROC.2010.2091610).
19. A. Erentok and R. W. Ziolkowski, "Metamaterial-Inspired Efficient Electrically Small Antennas," *IEEE Transactions on Antennas and Propagation*, vol. 56, no. 3, pp. 691–707, Mar. 2008, doi: [10.1109/tap.2008.916949](https://doi.org/10.1109/tap.2008.916949).
20. J. L. T. Ethier and D. A. McNamara, "Antenna Shape Synthesis Without Prior Specification of the Feedpoint Locations," *IEEE Transactions on Antennas and Propagation*, vol. 62, no. 10, pp. 4919–4934, Oct. 2014, doi: [10.1109/TAP.2014.2344107](https://doi.org/10.1109/TAP.2014.2344107).
21. Y. Aoki, H. Deguchi, and M. Tsuji, "Reflectarray with arbitrarily-shaped conductive elements optimized by genetic algorithm," *IEEE Xplore*, Jul. 01, 2011.
https://ieeexplore.ieee.org/abstract/document/5996437?casa_token=CnvMrp_YNK4AAAAA:ajcztgm2X5ULMkndzsmQ51cz_8FEwQcLGWPm9Ybn c0RbP1JySd3qCwc65DmN7cri4QVJ_qqBYg (accessed Aug. 15, 2022).
22. R. Li and G. Wei, "Electrically Small Antenna Shape Synthesis That Approaches the Maximum Achievable Directivity," *IEEE Antennas and Wireless Propagation Letters*, vol. 21, no. 6, pp. 1198–1202, Jun. 2022, doi: [10.1109/LAWP.2022.3161559](https://doi.org/10.1109/LAWP.2022.3161559).
23. D. B. Davidson, *Computational electromagnetics for RF and microwave engineering*. Cambridge ; New York: Cambridge University Press, 2011.
24. T. Rylander and Pär Ingelström, *Computational electromagnetics*. New York, N.Y.: Springer, 2013.
25. A. F. Peterson, S. L. Ray, Raj Mittra, and A. And, *Computational methods for electromagnetics*. Hyderabad: Universities Press, 2001, pp. 416–423.
26. H. van de Hulst, *Light scattering by small particles*. New York, Ny Dover [Ca, 2009.
27. T. Senior, "Combined resistive and conductive sheets," *IEEE Transactions on Antennas and Propagation*, vol. 33, no. 5, pp. 577–579, May 1985, doi: [10.1109/TAP.1985.1143616](https://doi.org/10.1109/TAP.1985.1143616).

28. R. Harrington and J. Mautz, "An impedance sheet approximation for thin dielectric shells," *IEEE Transactions on Antennas and Propagation*, vol. 23, no. 4, pp. 531–534, Jul. 1975, doi: [10.1109/TAP.1975.1141099](https://doi.org/10.1109/TAP.1975.1141099).
29. K. Dedrick, A. Hessing, and G. Johnson, "Bistatic radar scattering by randomly oriented wires," *IEEE Transactions on Antennas and Propagation*, vol. 26, no. 3, pp. 420–426, May 1978, doi: [10.1109/TAP.1978.1141862](https://doi.org/10.1109/TAP.1978.1141862).
30. Y. Guo and H. Uberall, "Bistatic radar scattering by a chaff cloud," *IEEE Transactions on Antennas and Propagation*, vol. 40, no. 7, pp. 837–841, Jul. 1992, doi: [10.1109/8.155750](https://doi.org/10.1109/8.155750).
31. K. Sarabandi and P. R. Siqueira, "Numerical scattering analysis for two-dimensional dense random media: characterization of effective permittivity," *IEEE Transactions on Antennas and Propagation*, vol. 45, no. 5, pp. 858–867, May 1997, doi: [10.1109/8.575638](https://doi.org/10.1109/8.575638).
32. S. W. Marcus, "Bistatic RCS of Spherical Chaff Clouds," *IEEE Transactions on Antennas and Propagation*, vol. 63, no. 9, pp. 4091–4099, Sep. 2015, doi: [10.1109/TAP.2015.2452963](https://doi.org/10.1109/TAP.2015.2452963).
33. B. Özbakis, "Analysis of the Electromagnetic Scattering from Flat Plates by Using Different Sinc-type Basis Functions in Method of Moments," Thesis, Izmir Institute of Technology, 2021.
34. Y. Lu *et al.*, "Ultrawideband Monostatic and Bistatic RCS Reductions for Both Copolarization and Cross Polarization Based on Polarization Conversion and Destructive Interference," *IEEE Transactions on Antennas and Propagation*, vol. 67, no. 7, pp. 4936–4941, Jul. 2019, doi: [10.1109/TAP.2019.2911185](https://doi.org/10.1109/TAP.2019.2911185).
35. S. H. Esmaeli and S. H. Sedighy, "Wideband radar cross-section reduction by AMC," *Electronics Letters*, vol. 52, no. 1, pp. 70–71, Jan. 2016, doi: [10.1049/el.2015.3515](https://doi.org/10.1049/el.2015.3515)